PHASE BEHAVIOR AND REACTION MECHANISM STUDY OF HYDROGEN STORAGE IN SODIUM BOROHYDRIDE

by

Ping Li

Bachelor of Science, Shaanxi University of Science and Technology, 2005

Master of Science, Tianjin University, 2007

Submitted to the Graduate Faculty of

Swanson School of Engineering in partial fulfillment

of the requirements for the degree of

Doctor of Philosophy

University of Pittsburgh

2013

UNIVERSITY OF PITTSBURGH

SWANSON SCHOOL OF ENGINEERING

This dissertation was presented

by

Ping Li

It was defended on

June 03, 2013

and approved by

J. Karl Johnson, Ph.D., Professor, Department of Chemical & Petroleum Engineering

Michael A. Matthews, Ph.D., Professor, Department of Chemical Engineering

Götz Veser, Ph.D., Professor, Department of Chemical & Petroleum Engineering

Wei Shi, Ph.D., Adjunct Professor, Department of Chemical & Petroleum Engineering

Dissertation Director: J. Karl Johnson, Ph.D., Professor, Department of Chemical & Petroleum Engineering

PHASE BEHAVIOR AND REACTION MECHANISM STUDY OF HYDROGEN STORAGE IN SODIUM BOROHYDRIDE

Ping Li, Ph.D.

University of Pittsburgh, 2013

Complex hydrides are promising hydrogen storage materials and have received significant attention due to their high hydrogen storage capacity. $NaBH_4$ has high gravimetric (10.6 wt%) and volumetric (115 kg of H_2 per cubic meter) hydrogen content. The $NaBH_4$ crystal structure, bulk and surface properties were determined from first-principles density functional theory (DFT) calculations. The surface of the $NaBH_4$ crystal is hygroscopic and adsorption of water vapor results in deliquescence. Interactions between H_2O and $NaBH_4$(100), which is the lowest energy surface, were investigated using van der Waals-corrected DFT. The results indicate that the adsorption energy per water molecule is roughly independent of water coverage, which suggests that a thick film of water can form on the surface of $NaBH_4$ without enthalpy penalty, and explains the hygroscopic nature of $NaBH_4$ at a molecular level. The initial stage of deliquescence was simulated via *ab initio* molecular dynamics (AIMD) at finite temperature and the first four significant steps of deliquescence were identified. These are the firstly atomically detailed studies of the hygroscopicity and deliquescence of $NaBH_4$.

Hydrolysis of $NaBH_4$ is of importance for niche hydrogen storage applications, such as portable power generation. Hydrolysis of $NaBH_4$ produces hydrogen gas and hydrated sodium metaborate, $NaBO_2$•*n*HO, when *n* depends on the hydrolysis conditions. One of the major challenges in practical use of $NaBH_4$ hydrolysis is the minimization of the degree of hydration of $NaBO_2$•*n*HO. Accordingly, DFT calculations on sodium metaborate with variying degrees of

hydration were carried out and the vibrational frequencies of solids for n=1/3 and n=2 have been calculated. The calculated frequencies are used to identify the vibrational modes observed in experiments and characterize the possible hydrolysis products. The most likely elementary reaction steps for aqueous $NaBH_4$ hydrolysis have been identified from DFT calculations and the corresponding energy barriers computed via the climbing image nudged elastic band (cNEB) method. The literature contains conflicting reports on the existence of $BH_{4-x}(OH)_x^-$ (x=1,2,3) intermediates, with some reports claiming to have observed x=2 and x=3 species, and other researchers claiming the only observe x=4 and trace amounts of x=1. Calculations reported in this work confirm the existence of intermediates for x=1,2,3. A new reaction pathway has been identified that involve intramolecular rearrangement of BH_3-OH_2 and BH_2OH-OH_2 to produce H_2. Reactions pathways involving two hydroxyborates were identified. It was found that extensive proton shuttling and solution rearrangement are naturally involved in the individual reaction steps for $NaBH_4$ hydrolysis. The cNEB calculations reveal that reactions between $BH_{4-x}(OH)_x^-$ (x=0,1,2,3) and H_2O have similar energy barriers to the initial step; therefore, the concept of a rate-limiting step cannot be applied to $NaBH_4$ hydrolysis.

TABLE OF CONTENTS

LIST OF TABLES

LIST OF FIGURES

PREFACE

First and foremost, I would like to thank my husband, parents, sister and brother for their endless love, support and encouragement.

I would like to sincerely thank my advisor, Professor J. Karl Johnson, for his supervision and support throughout my Ph.D. study. I express my heartfelt gratefulness for his excellent guidance. I thank Dr. Wissam A. Al-Saidi for suggestive advice and generous help for my study. I am grateful for his discussion and guide. I would also like to thank Professor Matthews, Professor Veser and Professor Shi for serving as a member on my Ph.D. defense committee.

I want to thank my fellow group members, Bo Zhang, De-Li Chen, Hang-Yan Chen, Pabitra Choudhury and Hong-Bin Xie for their help and encouragement. I cannot list all the names here, but you are always in my mind. Thank you all for the assistance you have given me and your friendship.

I would also like to acknowledge the computational resource provided by Center for Simulation & Modeling of University of Pittsburgh and Extreme Science and Engineering Discovery Environment (XSEDE).

1.0 INTRODUCTION

Energy consumption constantly increases as consequence of global population growth and economic growth, which makes great challenges to energy resources and global environment. Secure and reliable energy supplies are fundamental to people's current living standard, which can only be realized by mixing of various energy resources, such as fossil fuels, biofuels and hydroelectricity. While energy related CO_2 emission is primary reason for global warming. According to a report by the Intergovernmental Panel on Climate Change (IPCC, 2007), about 69% CO_2 emission are energy related and about 60% of greenhouse emissions are due to energy production and consumption. Therefore clean and renewable energy is highly in demand for sustainable development of human being and environment.

1.1 HYDROGEN ENERGY

In many ways, hydrogen is a kind of perfect energy carrier. It is abundant, high in energy density, and produces almost no pollution when used in a fuel cell. Additionally, it is non-toxic, can be generated from renewable resources and is not a greenhouse gas. Since hydrogen is clean, potable and versatile, it has been noted in numerous studies as an effective solution to reduce the world's dependence on non-renewable fossil fuels, as long as numerous obstacles in its safe and efficient production, storage, and application in fuel vehicles can be overcome. Hydrogen is not

freely available in nature and can be produced from a variety of feedstock, including coal, oil, natural gas, biomass, and water (see Table 1).

Table 1. Pathways for hydrogen production

	Resources	**Availability[(a)]**	**Current Consumption[(b)] (2012)**	**Projected Consumption[(b)] (2040)**
Non-renewable Pathways	Natural Gas	2,543 trillion cubic feet (recoverable resources)	25 trillion cubic feet	27 trillion cubic feet
	Coal (with sequestration)	441 billion tonnes (reverse base)	870 million metric tonnes/year	992 million metric tonnes/year
	Nuclear	6,077 million pounds	102 GWe	120 GWe
Renewable Pathways	Biomass	Between 0.4-1.1 billion dry tonnes/year	160 million metric tonnes/year	389 million metric tonnes/year
	Wind	3,750 GWe (capacity, not power output)	130 billion kWh	300 billion kWh
	Solar (photovoltaic and thermochemical)	32,300 GWe (capacity, full U.S.)	2.15 billion kWh	80 billion kWh

Resources: [(a)] Annual Energy Review 2010 and US Renewable Energy Technical Potential Report by NREL

[(b)] AEO 2012 Early Release.

Most hydrogen production in the United States today is by steam reforming of natural gas. However, it trades one relatively clean fuel for another with energy loss and releases carbon monoxide in the process, so it is still far away from meeting national energy needs. Though hydrogen production from biomass seems promising, it is still in the early research and

development stage. One problem is that biomass includes all organic substances, such as plants, wood chips and organic wastes, which leads to uncertain hydrogen producing processes. Currently, there is no commercially available process for producing hydrogen from biomass, but usually the method is to use a high-temperature and chemical additive to convert biomass into hydrogen and carbon dioxide. Hydrogen can also be produced by electrolysis, in which a current is passed through water. Although any power source can be used to produce the electric current, hydroelectric and solar energy resources offer low price for hydrogen production.

1.2 HYDROGEN STORAGE METHODS

Generally speaking, onboard hydrogen storage methods include compressed hydrogen, liquid hydrogen, physisorption storage and chemisorption storage. Compressed hydrogen is the gaseous phase of the element hydrogen which is kept under pressure. Compressed hydrogen in tanks at 350 bar and 700 bar is used for hydrogen in vehicles. Liquid hydrogen storage is the current bulk hydrogen storage method and has a very good safety record. The hydrogen is typically liquefied at the production site and then transported cross-country in tanks. But the energy requirement of liquefaction is high which leads to relatively high energy cost as compared to compressed hydrogen. In general, hydrogen storage in pressured tank or in liquid form requires significant energy costs and safety processing.

Nanoporous materials are considered to be strong candidates for physisorption hydrogen storage due to their large surface to volume ratio and tunable physical properties as a function of pore size and shape, such as carbon nanotubes, activated carbons, zeolites, and metal organic frameworks[1-3]. They can be structurally well ordered with similar pore sizes, or structurally

disordered with a wide range of pore sizes, but nanoporous solids with ordered structures attract numerous interests[4]. The main challenge of hydrogen storage via physical storage is that the stored gas must be recoverable with fast kinetics in useable form and the loaded materials should have high reversibility over multiple cycles.

In chemisorption, the H_2 molecule dissociates and migrates into the host lattice, and binds chemically with a binding energy about 2-4 eV[5]. Chemisorption materials have tunable kinetic and thermodynamic parameters by addition of catalysts and mixing of hydride phases. The binding is strong and H_2 desorption occurs at high temperatures. Examples of chemisorption materials include complex hydrides, carbohydrates, amine borane complexes and imidazolium ionic liquids.

Complex hydrides consisting of light metal hydrides and chemical hydrides attract intensive research interests because of their stable properties under ambient condition and high hydrogen-capacity. Many elemental metals that can reversibly absorb large amounts of hydrogen form metal hydrides MH_x (such as MgH_2 and $PdH_{0.6}$), in which hydrogen charging can be done using molecular hydrogen from an electrolyte and two atomic H recombine to H_2 molecule during desorption[6]. Metal hydrides with alloys are called intermetallic hydrides MN_xH_y, where M is typically a rare earth metal or an alkaline metal, and N represents a transition metal[7]. MN, MN_2 and MN_5 are common formation of host alloys[6]. The hydrogen density in intermetallic hydrides is low due to heavy metal alloys. Chemical hydrides are a family of hydrides containing relatively higher hydrogen density than metal/intermetallic hydrides but not reversible on board of a vehicles, such as $NaBH_4$, NH_3BH_3 etc. In most cases, chemical hydrides are produced from chemical reaction, where hydrogen atoms form chemical bonds with others. This differs from metal/intermetallic hydrides with hydrogen encapsulated in metallic interstitial sites. Chemical

hydrides are a rich source of hydrogen which can be released through high temperature dehydrogenation or reaction with water. For example, $NaBH_4$ reacts with H_2O and liberates hydrogen at ambient temperature. The spent fuel containing byproduct $NaBO_2$ can be later recycled to $NaBH_4$. Other discoveries on Li_3N[8] and NH_3BH_3[9] also bring new hope that chemical hydrides may be used for on-board hydrogen storage.

1.3 SODIUM BOROHYDRIDE AS A HYDROGEN CARRIER

1.3.1 Properties of sodium borohydride crystal

After $NaBH_4$ was first synthesized by Schlesinger et al.[10], there are both experimental[11-16] and theoretical[17-24] reports discussing its crystal structure as a function of temperature and pressure. At least three phases of $NaBH_4$ are known to exist at different conditions of T and P: the low pressure α-$NaBH_4$ (cubic – $Fm\bar{3}m$) transforms to β-$NaBH_4$ (tetragonal –$P\bar{4}21c$) phase at 6.3 GPa and then to an orthorhombic phase (Pnma) γ-$NaBH_4$ at 8.9 GPa. And the pressure-induced transition is completely reversible[15]. Considering temperature, Babanova et al. reported that the cubic phase exists in the 190-500 K range, and a tetragonal phase (P42/nmc) dominates in temperature 80-190 K[25]. They revised the low temperature tetragonal structure from $P\bar{4}21c$ proposed by Filinchuk et al. to higher symmetry P42/nmc[26]. For practical application, cubic is the major phase under ambient temperature and pressure, so our work mainly focuses on α-$NaBH_4$ (cubic - $Fm\bar{3}m$). α-$NaBH_4$ displays some disorder in terms of the positions of H atoms, i.e., lattice sites for H atoms in the α-$NaBH_4$ structure are half occupied, which means there are eight possible locations for the four H atoms in each BH_4 group.

Surface of sodium borohydride is very hygroscopic, which causes the crystal to absorb water from the atmosphere and dissolve when exposed in open air. Dihydrated $NaBH_4$ is a crystal state which exists between unhydrated $NaBH_4$ and its solution in the deliquescence process. $NaBH_4 \cdot 2H_2O$ is stable only at room temperature. At 313-315K, the hydrate decomposes into $NaBH_4$ and H_2O. $NaBH_4 \cdot 2H_2O$ was firstly reported over 50 years ago[27]. Custelcean et al. demonstrated the existence of short dihydrogen bonds in $NaBH_4 \cdot 2H_2O$ through neutron diffraction about ten years ago[28]. Recently, a full account of the structural data was established by Filinchuk et al. by using single-crystal X-ray diffraction and vibrational spectroscopy. They confirm the strong dihydrogen bond in the range of 1.77-1.95 Å in $NaBH_4 \cdot 2H_2O$ crystal structure[29]. The unit cell volume of $NaBH_4 \cdot 2H_2O$ increase linearly with temperature between 200 and 313K.

Murtomaa et al. demonstrated that an increase in relative humidity results in an increase in both the total amount of moisture uptake and rate of hydrolysis of $NaBH_4$ at 25°C.[30] Murtomaa's results were also qualitatively observed via experiments at higher temperatures.[31-34] However, increasing temperature beyond 110°C was found to decrease the rate and yield of the reaction for reactions taking place at one atmosphere pressure.[31-34] It may be that higher temperatures suppress deliquescence, resulting in a lower rate and overall yield. Hence, understanding the deliquescence process is important for optimizing the overall reaction conditions for hydrolysis of $NaBH_4$.

1.3.2 Hydrolysis reaction of sodium borohydride

The pathways for releasing stored hydrogen in $NaBH_4$ include thermolysis[35] and hydrolysis[10] and combination of the two[36,37]. However, only the hydrolysis approach is applicable in practical

hydrogen generation systems[34,38]. Thermolysis of $NaBH_4$ suffers from high operating temperature and poor control of reaction rate. So we are mainly interested in hydrolysis reaction of $NaBH_4$. Ideal $NaBH_4$ hydrolysis reaction occurs according to[10]:

$$NaBH_4(s) + 2H_2O \rightarrow 4H_2(g) + NaBO_2(aq) + heat \qquad (1.1)$$

Equation (1.1) captures neither the remarkable subtlety of the fundamental molecular mechanisms nor the practical difficulties of carrying out this reaction. Generally, the hydrolysis of solid $NaBH_4$ or of highly concentrated solutions of $NaBH_4$ forms mixtures of hydrated sodium metaborates as by-products by the following reaction:

$$NaBH_4(s) + (2+x)H_2O \rightarrow 4H_2(g) + NaBO_2 \cdot xH_2O(aq) + heat \qquad (1.2)$$

In this way, the hydrogen density of the whole system is limited by excess water requirement x due to the low solubility in water of both $NaBH_4$ (55 g $NaBH_4$/100 g H_2O at 25 °C[39])and of the metaborate byproducts (28 g $NaBO_2$/100 g H_2O at 25 °C[40]). Moreover, the reaction mixture becomes basic due to the formation of hydrated metaborate byproducts, and these reaction intermediates are stabilized at elevated pH, which prevents the reaction to completion even though it is strongly favored thermodynamically (Gibbs free energy is estimated to be about -340 kJ/mol $NaBH_4$[34] and enthalpy of reaction is measured to be at least -210 kJ/mol $NaBH_4$[41,42]). Hence, the yield of hydrogen in aqueous hydrolysis reaction is low. The overall conversion of $NaBH_4$ by the self-hydrolysis reaction at room temperature is only 7-8%[43,44]. To improve rates and yields of the reaction, two kinds of catalyst are employed: acid catalyst and metal heterogeneous catalyst. Catalytically accelerated $NaBH_4$ hydrolysis for the generation of hydrogen has been studied since the 1950s[10], and it is now under intensive investigation[45-47]. But the solubility limits is still an insurmountable problem for practical application and fulfillment of

DOE target. In another word, the solubility of $NaBH_4$ in water is about 35% by weight at ambient temperature, but practical systems to date use feed compositions of only about 15% (corresponding x = 8~9) to prevent unwanted crystallization of the less soluble reaction product $NaBO_2$, which dramatically decrease the hydrogen capacity of the system.

In practice, $NaBH_4$ solutions are typically maintained as strongly basic solution by adding NaOH to increase the shelf life and to prevent H_2 gas being generated upon storage. Catalyzed hydrolysis is carried out on basic $NaBH_4$ solutions. Thus, hydrolysis kinetics is a complex process influenced by multiple factors such as $NaBH_4$ concentration, reaction temperature, stabilizer concentration, and catalyst performance. Apparent activation energy of spontaneous $NaBH_4$ hydrolysis reaction was reported about 98 ± 10 kJ/mol[48]. Metal catalyzed $NaBH_4$ hydrolysis reactions lead to lower apparent activation energy. Li et al. reported the apparent activation energy with CoB/open-CNTs catalysts is 37.63 kJ/mol[49]. The apparent activation energy of Co-P/Ni foam catalyst manufactured under optimal conditions is 46.8 kJ/mol[50]. PVP-stabilized Ru (0) nanorods[51], Ru-promoted sulphated zirconia[52] and Fe-Co-B/Ni foam[53] catalysts result in the apparent activation energy as 33.4 ± 1 kJ/mol, 76 kJ/mol and 27 kJ/mol, respectively.

To date, traditional $NaBH_4$ hydrolysis reaction taking place in solution is still far away from practical application due to the unsolved issues as mentioned above. Recently, Matthews' group at University of South Carolina discovered hydrolysis of solid chemical hydrides can be accomplished with steam, without the need for a catalyst[32]. Several hydrides, including $NaBH_4$, $NaAlH_4$, $LiAlH_4$, and $LiBH_4$ have been so reacted and are potential useful as compact sources of hydrogen for portable fuel cells. Water vapor hydrolysis has several advantages over the conventional aqueous hydrolysis. Firstly, $NaBH_4$ crystal directly contacts with water vapor and

releases hydrogen after absorbing enough water. This process minimizes the amount of excess water, and overcomes the solubility limits inherent in aqueous solution; Secondly, the water vapor hydrolysis of $NaBH_4$ can take place with fast kinetic and high conversion without catalyst, which is a significant improvement compared to traditional catalyst-aided aqueous hydrolysis; Last but not least, water vapor hydrolysis happens at elevated temperature (> 100°C), thermal and water integration is a great way to save energy, *i.e.* recycling the energy generated in the reaction process to heat up the water vapor.

Despite a long history of research and development, the fundamental mechanism of $NaBH_4$ hydrolysis reaction is still unknown at molecular level, neither of aqueous phase reaction nor vapor phase reaction. Besides, Matthews' group found the kinetic limitations associated with aqueous solution hydrolysis are not present in the water vapor hydrolysis reaction. These make an investigation for reaction mechanism of $NaBH_4$ hydrolysis important and urgent for practical hydrogen storage system. Upon the reaction mechanism, we can tune the reaction process and make $NaBH_4$ an applied and efficient hydrogen carrier. Unfortunately, until now, there is very little experimental structural information on intermediate phases or reaction pathways in the $NaBH_4$+H_2O system. The literature contains conflicting reports on the existence of $BH_{4-x}(OH)_x^-$ (x=1,2,3) intermediates, with some reports claiming x=1, 2 and 3 species[54-59], i.e. a mechanism based on the substitution of B-H bonds by B-OH bonds: $BH_4^- \rightarrow BH_3OH^- \rightarrow BH_2(OH)_2^- \rightarrow BH(OH)_3^- \rightarrow B(OH)_4^-$. While other researchers claiming the only observe x=4 and trace amounts of x=1[48]. For acid catalyzed $NaBH_4$ hydrolysis reaction, formation of BH_3 is the rate-limiting step. After formation, BH_3 quickly reacts with $3H_2O$ to generate $B(OH)_3$ and 3 H_2 molecules[60-63]. The ambiguity makes our theoretical exploration difficult but at the same time significantly meaningful to complement experiment. Our work about $NaBH_4$ is the first attempt at molecular

level understanding of this particular hydrolysis reaction, which is one of a larger class of possible hydrolysis reactions. The goal of our work is to develop a fundamental molecular level understanding of the hydrolysis reaction pathway between water vapor and a chemical hydride, sodium borohydride, which liberates pure hydrogen gas. We expect new scientific insights into the structure and reactivity of the highly hygroscopic hydride surface, and of the mechanisms of adsorption and reaction. Experimentally and theoretically this is a very challenging system because of the near simultaneous reaction that follows water adsorption. So we focus on water sorption and reactivity by modeling $NaBH_4$ surface and reaction mechanisms between deliquesced $NaBH_4$ and water.

2.0 THEORETIC APPROACH

In this chapter, the basic concepts of theoretical approaches for the study of $NaBH_4$ properties and hydrolysis reaction mechanisms are presented. The fundamentals of density functional theory and two related simulation programs are introduced. In addition, molecular dynamics and one related simulation package are presented.

2.1 DENSITY FUNCTIONAL THEORY

Density functional theory has been the dominant method for the quantum mechanical simulation of periodic systems and molecule cluster in physics and chemistry to investigate the electronic structure of many-body systems. With this theory, the properties of a many-electron system can be determined by using electron density instead of solving N-electron wavefunction $\psi(x_1, x_2, ..., x_N)$ and the associated Schrödinger.

Hohenberg and Kohn[64] provided the basis of DFT and proved that all electronic properties of the system can be determined by its ground state probability density in 1964. They introduced the concept of DFT but did not provide a practical method to calculate the ground state properties based on electron density. In 1965 Kohn and Sham[65] proposed an approach to solve energy functional by introducing a fictitious system of N non-interacting electrons to be

described by a single determinant wavefunction in N "orbitals". Their approach achieves an accurate solution of the density and ground state energy of a system.

DFT calculations allow us to develop a complete picture of how $NaBH_4$ works as hydrogen storage material by (i) calculating its crystal structure; (ii) simulating interaction between H_2O and its surface to explain hygroscopicity of surface; (iii) identifying elementary reaction steps of its hydrolysis reaction.

2.1.1 Hohenberg-Kohn Theorem

Hohenberg and Kohn proved the two theorems to consider DFT as an exact theory of many-body systems[64]. The first theorem can be stated as:

The electron density determines the external potential (to within an additive constant)

It indicates that the Hamiltonian operator

$$\hat{H} = -\frac{1}{2}\sum_{i}^{N}\nabla_i^2 + \hat{V}_{ext} + \sum_{i<j}^{N}\frac{1}{|\boldsymbol{r}_i - \boldsymbol{r}_j|} \qquad (2.1)$$

can be uniquely determined by integration of electron density over all space, because Hamiltonian is dependent on the external potential and the total number of electrons N. Hohenberg and Kohn[64] provided a straightforward proof of this theorem, which was extended to include system with degenerate states in proof given by Levy[66]. The second theorem establishes a variational principle:

For any positive definite trial density, ρ_t, such that $\int \rho_t(\boldsymbol{r})dr = N$ *then* $E[\rho_t] \geq E_0$

The proof of this theorem is straightforward based on the first theorem. Because the trial density determines a unique trial Hamiltonian (H_t) and thus wavefunction (Ψ_t), the second theorem

$$E[\rho_t] = \langle \Psi_t \mid H \mid \Psi_t \rangle \geq E_0 \qquad (2.2)$$

follows the variational theorem of the Schrödinger equation ($E[\Psi] \geq E_0$). This theorem confines density functional theory to ground state studies, but an extension to excited states which are orthogonal to the ground state can be done, provided that the exact ground state wavefunction is known.

2.1.2 Self-consistent Kohn-Sham Equation

Based on the form of Schrödinger equation, the energy functional contains three terms: the interaction with external potential, the electron-electron interaction and the kinetic energy

$$E[\rho] = V_{ext}[\rho] + V_{ee}[\rho] + T[\rho] \qquad (2.3)$$

where the interaction with external potential can be calculated from $V_{ext}[\rho] = \int \hat{V}_{ext}\rho(r)dr$, and the kinetic and electron-electron functionals are unknown. Kohn and Sham proposed a fictitious system where kinetics energy and electron density are known exactly from the orbital

$$T_s[\rho] = -\frac{1}{2}\sum_i^N \langle \phi_i \mid \nabla^2 \mid \phi_i \rangle \qquad (2.4)$$

This is not the true kinetic energy but is that of a system of non-interacting electrons. The true ground state density can be expressed from non-interacting orbitals

$$\rho(r) = \sum_i^N \mid \phi_i \mid^2 \qquad (2.5)$$

The electron-electron interaction is classical Coulomb interaction and calculated from

$$V_H[\rho] = \frac{1}{2}\int \frac{\rho(\mathbf{r}_1)\rho(\mathbf{r}_2)}{\mid \mathbf{r}_1 - \mathbf{r}_2 \mid} d\mathbf{r}_1\mathbf{r}_2 \qquad (2.6)$$

Based on the above terms, the energy functional can be rearranged as

$$E[\rho] = T_s[\rho] + \mathrm{V}_{ext}[\rho] + V_H[\rho] + E_{xc}[\rho] \qquad (2.7)$$

The $E_{xc}[\rho]$ is called exchange-correlation functional, equivalent to the sum of error made in using a non-interacting kinetic energy and error made in treating electron-electron interaction classically. Practically, the accuracy of DFT rests on the approximation used for E_{xc}.

2.1.3 Exchange and Correlation Functional Approach

The approximation of E_{xc} has introduced a large and still expanding field of research—functional development. The local density approximation (LDA)[67] is the basis of all approximate exchange-correlation functionals. This model is based on the idea of uniform electron gas, where electrons move on a positive background charge distribution so the total charge of system is neutral,

$$E_{xc}^{LDA}[\rho] = \int \rho(\boldsymbol{r})\varepsilon_{xc}(\rho(\boldsymbol{r}))d\boldsymbol{r} \qquad (2.8)$$

here, $\varepsilon_{xc}(\rho(\boldsymbol{r}))$ is the exchange-correlation energy per particle of an uniform electron gas of density $\rho(\boldsymbol{r})$. It can be further split into exchange and correlation contributions. The accuracy of LDA for the exchange energy is typically ±10%, and correlation energy is generally overestimated. This moderate accuracy makes LDA insufficient for many applications.

A logical step to go beyond LDA is to use gradient of the charge density, $\nabla\rho(\boldsymbol{r})$, instead of density $\rho(\boldsymbol{r})$ at a particular point $\boldsymbol{r}$, which is termed as generalized gradient approximation (GGA)

$$E_{xc}^{GGA}[\rho_\alpha, \rho_\beta] = \int f(\rho_\alpha, \rho_\beta, \nabla\rho_\alpha, \nabla\rho_\beta)d\boldsymbol{r} \qquad (2.9)$$

Recently functional which rely on the semi-local information in the Laplacian of the spin density or of the local kinetic energy density have been developed[68-70]. Such functional are generally referred to as meta-GGA. Another approach introduced by Becke is hybrid function with coefficients determined by a fit to the observed atomization energies, ionization potentials, proton affinities and total atomic energies for a number of small molecules[71]. Hybrid functionals are now widely used in chemical application with improved reliability than GGA functional in computing binding energies, geometries and frequencies.

2.2 VIENNA AB-INITIO SIMULATION PACKAGE

The Vienna *ab-initio* simulation package (VASP)[72-74] is used to perform quantum-mechanical calculations using pseudopotentials or the projector-augmented wave (PAW)[75,76] method and a plane wave basis set. Electronic and atomic structures of molecules and crystal can be simulated in VASP. The configuration of VASP is versatile and can be tuned for different systems and desired properties. Four most important input files of VASP are INCAR, KPOINTS, POSCAR and POTCAR. As the central input file, the INCAR file determines the purpose of calculation and method to realize the purpose including information about the optimization algorithm, energy cut-off for the plane waves, exchange-correlation functionals, and required precision. The KPOINTS file contains k-point coordinates and weights or the mesh size for creating the k-point grid. Information about lattice geometry and the ionic positions (optionally velocities for molecular dynamics calculation) of simulated system are contained in the POSCAR file. The POTCAR file specifies the pseudopotential or PAW potential for each atomic species and the chosen exchange-correlation approximation.

2.3 QUANTUM ESPRESSO

Quantum ESPRESSO is an Open-Source code distributed for free under the GNU General Public License for electronic-structure calculations and materials modeling[77]. Similar to VASP, it is also based on DFT, plane wave, and pseudopotentials. Quantum ESPRESSO can be used for ground-state calculations, structural optimization, transition states and minimum energy paths searching, AIMD, spectroscopic properties and so on. In our work, we optimized the structure of $NaBH_4$ hydrolysis byproducts ($NaBO_2 \cdot \frac{1}{3}H_2O$ and $NaBO_2 \cdot 2H_2O$) and calculated Raman bands of each structure to identify the motion of Raman modes at molecular level.

2.4 MOLECULAR DYNAMICS AND LAMMPS

Molecular dynamics calculate physical properties of systems via simulation of molecules and atoms movement at finite temperature. It deals with ensembles of atoms through statistical mechanism. A certain physical property can be calculated from probability distribution of these ensembles based on the assumption that every state is equally likely to be occupied, which is reasonable for a system at thermodynamic equilibrium but untrue for non-equilibrium systems. Therefore molecular dynamics requires rigorous sampling of a large number of possible phase-space distributions. In molecular dynamics, a molecule is described as a series of charged points (atoms) linked by springs (bond). Force field is an empirical potential energy function that models the main interactions found on a molecular system with time evolution, including bonds, angles, dihedrals, coulomb and van der Waals. Molecular dynamics has the advantage of dealing

with large number of atoms and longer simulation time than AIMD, but chemical properties cannot be accurately simulated.

LAMMPS, copyrighted-code distributed under GNU public License, is a classical molecular dynamics code which simulates an ensemble of particles in a liquid, solid or gaseous state[78,79]. It supports a large amount of model types and force fields. In most cases, LAMMPS integrates Newton's equations of motion for particles (atoms and molecules) which interact with a variety of initial and/or boundary conditions via short- or long-range forces. LAMMPS uses neighbor lists to keep track of nearby particles for computational efficiency[79]. The lists are optimized for systems with particles that are repulsive at short distances, so that the local density of particles never becomes too large. We developed a force field for B, H, Na and O species readable to LAMMPS that can be used to calculate the Gibbs free energy change of moving Na^+/BH_4^- from crystal lattice to the bulk liquid phase of H_2O at initial stage of deliquescence to understand the deliquescence process at molecular level.

3.0 RESULTS AND DISCUSSION

3.1 STRUCTURE DETERMINATION AND BULK PROPERTIES

3.1.1 Structure determination

Before any further calculation, we firstly used DFT[64,65] to fully characterize the α-$NaBH_4$ structure ($Fm\bar{3}m$, No. 225)[15], so that following calculations can be carried out with accurate structure. First-principles calculations were performed on $NaBH_4$ using plane wave DFT with PW91-GGA functional[80,81] PAW method, as implemented in the VASP. We used a conjugate gradient method for optimization of $NaBH_4$ structure. The cutoff energy was set to 520 eV, which was found to be sufficiently high to give well-converged structures and total energies. 7×7×7 Monkhorst-Pack (MP) meshes were used to sample the Brillouin zone in crystal structure optimization. This gave a k-point spacing less than 0.05 $Å^{-1}$. Convergence of the total energy with the number of k-points was examined for structure determination calculations. Ion positions, the supercell shape and volume were optimized until the forces on all atoms were less than 0.01 eV/Å.

We labeled the four different boron atoms in one unit cell as shown in the Figure 1. Since all BH_4 groups should be in tetrahedron configurations, we considered the hydrogen sites around every boron atom either in A or B orientations defined arbitrarily (Figure 1).

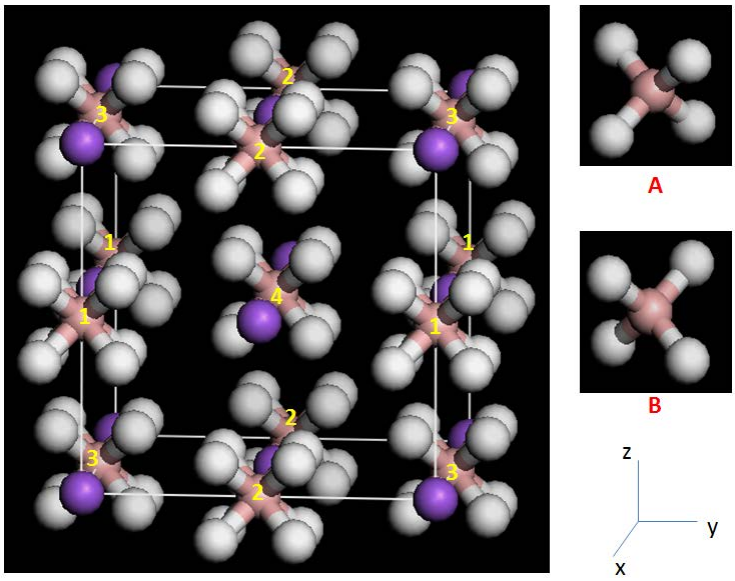

Figure 1. $NaBH_4$ unit cell with half hydrogen occupancy. Pink, purple, and white indicate B, Na, and H, respectively. Similar symbols are applied in the following figures except redefinition. The four boron atoms are labeled 1-4, and BH_4 group is in either A or B configuration

It is easily to find that rotating either one of A and B by 90 degree, it will become identical to the other. Each of the four BH_4 groups in a unit cell has two possible configurations, which gives a total of 16 possible combinations. Because configuration A and B are identical upon rotating by 90 degrees, it is certain that the 16 structures are degenerate, i.e., the number of different distinguishable structure should be much less than 16. After relaxing these 16 structures to ground state, we found they are simplified to 3 distinct structures: lattice parameter of structure I a = 6.1506 Å, with relaxation energy E = -94.55289 eV; lattice parameter of structure II a = 6.1506 Å, with relaxation energy E = -94.73466 eV; lattice parameters of structure III a = 4.3491 Å, c = 6.1506 Å, with relaxation energy E = -94.81914 eV, as shown in Table 2. Of the three structures, Structure I is the highest in energy because all the BH_4 groups are being oriented in the same direction, which maximizes the steric hindrance among H atoms on neighboring BH_4 groups, *i.e.* all neighboring BH_4 groups are in eclipsed configurations. Structure II relaxes one set of configurations from their eclipsed so lowers itself energy, and structure III relaxes all eclipsed

neighbors but become tetragonal. Therefore, Structure II which is in cubic phase and has lower energy is the actual existing structure of α-$NaBH_4$. All of our further calculations are based on optimized structure II.

Table 2. 16 possible structures of α-$NaBH_4$

	possible structures	Structure details	Space group	a, b, c (Å)	relaxation energy (eV)
Structure I	No. 1	1A,2A,3A,4A	$F\bar{4}3m$	6.1506, 6.1506, 6.1506	-94.55289
	No. 2	1B,2B,3B,4B	$F\bar{4}3m$	6.1506, 6.1506, 6.1506	-94.55289
Structure II	No. 3	1B,2A,3A,4A	$Fm\bar{3}m$	6.1506, 6.1506, 6.1506	-94.73466
	No. 4	1A,2B,3A,4A	$Fm\bar{3}m$	6.1506, 6.1506, 6.1506	-94.73466
	No. 5	1A,2A,3B,4A	$Fm\bar{3}m$	6.1506, 6.1506, 6.1506	-94.73466
	No. 6	1A,2A,3A,4B	$Fm\bar{3}m$	6.1506, 6.1506, 6.1506	-94.73466
	No. 7	1A,2B,3B,4B	$Fm\bar{3}m$	6.1506, 6.1506, 6.1506	-94.73466
	No. 8	1B,2A,3B,4B	$Fm\bar{3}m$	6.1506, 6.1506, 6.1506	-94.73466
	No. 9	1B,2B,3A,4B	$Fm\bar{3}m$	6.1506, 6.1506, 6.1506	-94.73466
	No. 10	1B,2B,3B,4A	$Fm\bar{3}m$	6.1506, 6.1506, 6.1506	-94.73466
Structure III	No. 11	1A,2A,3B,4B	P42/nmc	4.3491, 4.3491, 6.1506	-94.81914
	No. 12	1B,2B,3A,4A	P42/nmc	4.3491, 4.3491, 6.1506	-94.81914
	No. 13	1A,2B,3A,4B	P42/nmc	4.3491, 4.3491, 6.1506	-94.81914
	No. 14	1B,2A,3B, 4A	P42/nmc	4.3491, 4.3491, 6.1506	-94.81914
	No. 15	1A,2B,3B,4A	P42/nmc	4.3491, 4.3491, 6.1506	-94.81914
	No. 16	1B,2A,3A,4B	P42/nmc	4.3491, 4.3491, 6.1506	-94.81914

The experiment lattice parameter of α-$NaBH_4$ is a = 6.1506Å, and cell volume V = 232.68 $Å^3$. Our DFT optimized structure of α-$NaBH_4$ is a = 6.0509 Å, d_{B-H} = 1.22 Å, giving a cell volume 4.786% smaller than experimental value[15]. The lattice sites for H atoms in the optimized structures of α-$NaBH_4$ are shown in Figure 2, in which BH_4 groups are disordered. This structure is consistent with BH_4 group order-disorder analysis by Filinchuk[29] et al. The hydrogen positions in optimized structure of α-$NaBH_4$ determined by Kim et al[22] is No. 10 in Table 2. The lattice constant of their optimized structure is a = 6.02 Å. We believe the deviation of lattice constant is result from calculation parameters, such as cutoff energy and Monkhorst-Pack mesh of k-points.

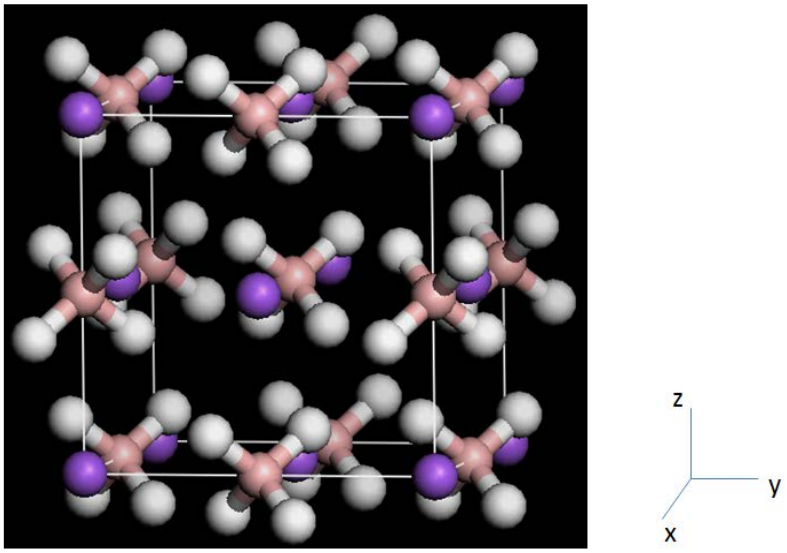

Figure 2. Optimized $NaBH_4$ structure

3.1.2 Bulk properties

We calculated the elastic constants, C_{11}, C_{12}, and C_{44}, and bulk modulus B of α-$NaBH_4$ by performing six finite distortions of the lattice and deriving the elastic constants from the strain-stress relationship in VASP (*i.e.* IBRION = 6, ISIF = 3). For cubic cell, bulk modulus B =

$(C_{11}+2*C_{12})/3$. Table 3 shows our calculated elastic constant and bulk modulus and other theoretical and experimental results. We believe that the divergence between our calculated elastic constants and experimental values result from the fact that our calculations ignored the contributions of disordered H positions to the elasticity in the real material.

Table 3. Bulk modulus and elastic constants of $NaBH_4$

	B (GPa)	C_{11} (GPa)	C_{12} (GPa)	C_{44} (GPa)
Calculated value (GPa)	19.78[a]	32.49[a]	13.42[a]	12.68[a]
	20.6[b]			
	13.5[c]	22.7[c]	8.9[c]	13.2[c]
Experimental value (GPa)	15.8±1.8[d]	26.5±1.1[d]	9.5±0.57[d]	9.4±2.7[d]
	19±1[d]			
	19.9[e]			

[a]Data from this work, [b]Data from reference[82], [c]Data from reference[22], [d]Data from reference[83], [e]Data from reference[15].

Bader charge analysis is based on only the charge density and assumes that charge density maxima are located at atomic centers (or at pseudoatoms). The definition of an atom is also on the basis of electronic charge density. Zero flux surfaces, a 2-D surface where charge density is a minimum perpendicular to the surface, are used to divide atoms. Bader charge analysis of bulk $NaBH_4$ crystal was performed in VASP[84-86], and the results are shown in Table 4.

Table 4. Bader charge of $NaBH_4$ crystal

Elements	Charges
Na	q(Na) = 0.94
B	q(B) = 1.66
H	q(H) = -0.65

In summary, the crystal structure of α-$NaBH_4$ was determined with lattice constant a = 6.1506Å, which was unknown when this project started. The optimized structure agrees well with result reported by other researchers. Elastic constant and bulk modulus were calculated from DFT. The divergence between our calculated elastic constants and experimental values probably result from the fact that DFT calculations ignored the contributions of disordered H positions to the elasticity in the real material. Bader charge analysis was performed for bulk $NaBH_4$ and demonstrated the negative charge on H atoms, which is fundamental to hydrolysis reaction between $NaBH_4$ and H_2O, i.e. dihydrogen bonds are formed between negative charge H in $NaBH_4$ and positive charged H in H_2O and then facilitate production of H_2 molecules.

3.2 SURFACE PROPERTIES AND INTERACTION BETWEEN SURFACE AND WATER

To the best of our knowledge, there have been no atomistic studies of the deliquescence process of $NaBH_4$ or any studies of water adsorption on $NaBH_4$ surfaces. As an initial step in understanding how deliquescence takes place, we here study the adsorption of water on the (100) surface of α-$NaBH_4$. The (100) surface has the lowest energy based on our surface energy calculations and is expected to be the dominant surface exposed on $NaBH_4$ crystallites. Our purpose in examining H_2O adsorption on $NaBH_4$(100) is to identify the atomic-level interactions that give rise to the highly hygroscopic nature of $NaBH_4$, and hence makes deliquescence thermodynamically favorable. The approach we take to study the adsorption of H_2O on $NaBH_4$(100) is to use van der Waals-corrected density functional theory (DFT), which can account for the chemical and physical interactions relevant to this system.

3.2.1 Surface properties

In surface energy calculation, we used 5 layers in our surface slab calculations, finding that using more layers did not give any significant difference in the surface energies. The slab was separated from its periodic image in the direction normal to the surface by a vacuum spacing of 15 to 20 Å. Unless stated otherwise, Brillouin-zone integrations employed a 7×7×1 Monkhorst-Pack k-point grid. Slab calculations allowed the top and bottom layers to relax, holding the middle three layers fixed in their optimized bulk positions. We checked that relaxation of additional layers had negligible effect on the energies. The positions of all unconstrained atoms were relaxed until the forces on each of the atoms were smaller than 0.03 ev/Å.

We examined surface terminations generated from families of low miller index surfaces, including (001), (101) and (111), to identify the surfaces with lowest surface energy. Since α-$NaBH_4$ is cubic (001) and (101) are equivalent to {001} and {101}, respectively. The average surface formation energy E_{surf} [87] was calculated by

$$E_{surf} = \frac{1}{2A}(E_{slab} - nE_{bulk}) \qquad (3.1)$$

Here, E_{surf} is the surface formation energy, A is the surface area, E_{slab} is the DFT computed slab energy, E_{bulk} is the DFT computed total energy per formula unit in the bulk, and n is the number of formula units in the slab supercell. The factor of 2 accounts for the two sides of the slab. The surface energy computed from Equation (3.1) is actually an average of two complementary surface terminations, which are not identical for these surfaces. Calculation values are presented in Table 5, and (001) is the lowest energy surface and is expected to be the dominant surface exposed on $NaBH_4$ crystallites. Water adsorption and hydrolysis reaction most

probably happens on this surface. (111) is unstable surface. After relaxation, some B-H bond length increase severely. In addition, distance between Na and B decrease, and Na layer tends to merge into its complementary BH_4 layer.

Table 5. Calculated surface energies (J/m^2) for low Miller index surfaces

Surface index	Surface energy E_{surf}
(001)	0.098
(101)	0.209
(111)	0.827

3.2.2 Interaction between surface and water

A four-layer slab, separated by a vacuum of at least 20 Å along the stacking direction to mitigate the interaction between periodic images, was employed to model the $NaBH_4$(100) surface. The top two layers in the slab were allowed to relax, while the bottom two layers were held fixed in their optimized bulk positions. Test calculations with six layers gave similar results to those computed with four layers. The positions of relaxed atoms were optimized until the forces on the atoms were less than 0.01 eV/Å. The optimized bulk $NaBH_4$ lattice constant was calculated to be 6.05 Å, which is in good agreement with the experimental value (6.15 Å) and other theoretical calculations (6.02 Å from Kim et al.[88] and 6.06 Å from Vajeeston et al.[20]) . Water molecules were placed on one side of the slab. We used a vacuum spacing of 25 Å to accommodate 48 and 64 water molecules on the surface. The vacuum height was 20 Å on all other systems. A plane wave basis set with cutoff energy of 520 eV was used in all calculations, which was found to be sufficiently high to give well-converged structures and total energies. The Fermi level was smeared by the Gaussian method with a width of 0.05 eV. All calculations used a 2×2 surface

unit cell, which is large enough to mitigate interactions between periodic images, as confirmed by test calculations using a 3×3 surface, which gave differences in the adsorption energies of several meV. A Monkhorst-Pack scheme having a grid mesh smaller than 0.05 $Å^{-1}$ was employed to sample the Brillouin zone.

Dispersion interactions are expected to be important for accurately characterizing the adsorption energies of H_2O on $NaBH_4$. However, standard local and semi-local functionals used in current DFT implementations do not account for van der Waals (vdW) interactions. There are several different approaches for including dispersion effects within DFT, such as the semiempirical vdW approach proposed by Grimme, known as DFT-D2[89], DFT-Tkatchenko-Scheffler (TS) approach[90], vdW-DF[91,92] and vdW-DF2[93] approaches of Langreth and coworkers. We have used the DFT-TS approach as implemented within VASP by Al-Saidi et al[94,95]. We have computed adsorption energies and geometries for several $H_2O/NaBH_4(100)$ configurations using each of these functionals. We have found that DFT-D2 and DFT-TS give similar adsorption energies and geometries for our test systems, whereas the vdW-DF and vdW-DF2 approaches appear to overbind the water in comparison. We used the bulk structure of $NaBH_4$ optimized with the GGA-PW91 functional for all our slab calculations, fixing the bottom two layers to the positions computed from this functional. We did this because the DFT-D2, DFT-TS, and vdW-DF functionals underestimate the bulk lattice constant, giving values of 5.71 Å, 5.63 Å, and 5.95 Å respectively. The DFT-D2 approach also underestimates the volume of $NaBH_4 \cdot 2H_2O$[96]. For many systems[97-99] the GGA is reported to overestimate the unit cell volume. Adding vdW interactions generally results in smaller lattice constants and hence acts to correct over prediction of the lattice constants from GGA. In our case the PW91 functional under-predicts the lattice constant relative to the experiments, therefore adding vdW corrections

exacerbates this problem. This is why we chose to freeze the bottom two layers at the PW91 optimized values in all our slab calculations. In the remainder of the section all energies reported are for the DFT-D2 formalism. We chose to carry out most of the calculations with this approach because of the efficiency of DFT-D2 and the good agreement it gave with the DFT-TS approach.

We have used a basin hopping-like approach[100] to explore configuration space for adsorption of multiple water molecules in order to identify low energy structures. For systems with four H_2O molecules and higher we performed ab initio molecular dynamics (MD) calculation at 80 K in the canonical ensemble with Nosé–Hoover thermostat to generate candidate water configurations. Simulations were carried out for 8 picoseconds with 1 femtosecond time step. We then optimized snapshots every 100 steps from the MD trajectory after 3 picoseconds equilibrium time to identify configurations with low energies. The parameters setting for optimization is described in the first paragraph of this section.

3.2.2.1 Water monomer adsorption.

We considered four different possible adsorption sites for a single H_2O molecule on $NaBH_4$(100). These sites are: hollow, bridge, sodium, and boron, and are shown in Figure 3. We considered four different possible orientations of H_2O above each adsorption site, as shown in Figure 4. The initial orientations were chosen to span a wide range of possible final relaxed orientations of H_2O on $NaBH_4$(100). Configuration (A) in Figure 4 has one O-H bond parallel to the surface and the water plane forming a 45° angle to the substrate surface. Configuration (B) has both H atoms pointing toward the surface with the water plane perpendicular to the (100) surface. The dipole vector of H_2O is also perpendicular to the substrate surface. Configuration (C) has both H pointing away from the surface and the water plane perpendicular to the surface.

The dipole vector of H_2O is also perpendicular to the substrate surface. Configuration (D) has one O-H bond perpendicular to the surface with the water plane is perpendicular to the surface.

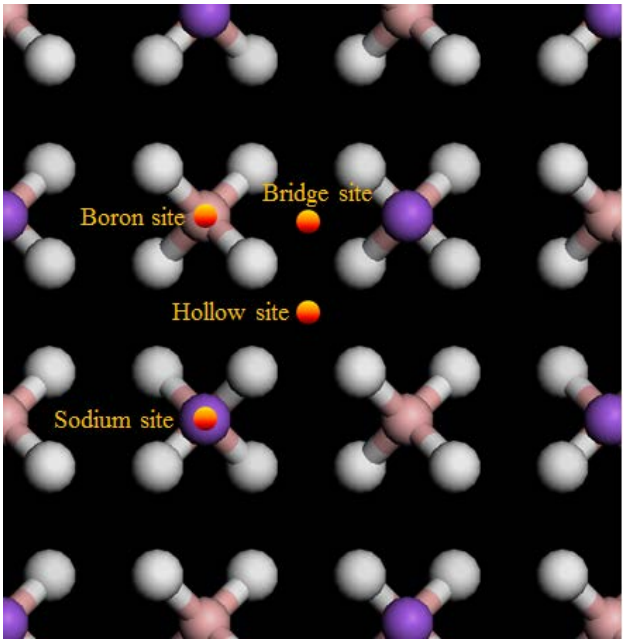

Figure 3. Top view of H_2O adsorption sites on the $NaBH_4(100)$ surface identified by multicolored dots. The atom types are identified by the following colors: white is hydrogen, red is oxygen, pink is boron, and purple is sodium.

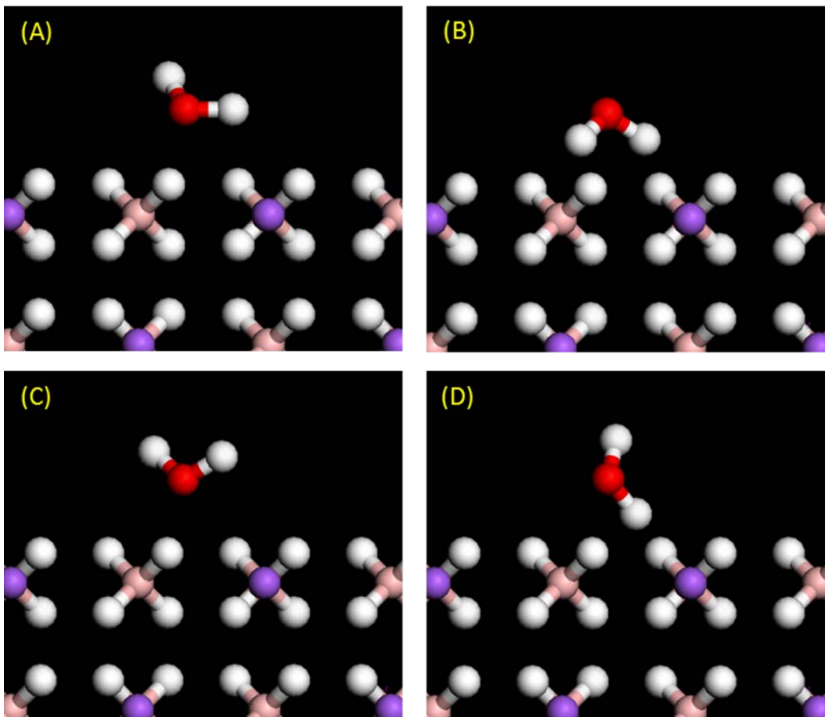

Figure 4. Initial water configurations considered for adsorption as viewed from the (010) plane.

The four adsorption sites coupled with the four H_2O orientations gives 16 different initial structures, as listed in Table 6 and Table 7. After optimization the water molecule ends up either at the sodium or boron atop sites, indicating that the bridge and hollow sites are unstable. The first 12 initial geometries, which include all but the boron atop geometries, all optimize to the sodium atop site and have similar adsorption energies and geometries (Table 6). In Figure 5(a) we identify three parameters that characterize the geometry of H_2O bound to the sodium site: The angle α defines the tilt angle between the plane of H_2O and the plane of $NaBH_4(100)$. The azimuthal angle between the [010] direction and the projection of the H_2O dipole vector onto the (100) surface is Φ. We note that the O of H_2O adsorbed on the sodium site does not actually sit directly atop the sodium atom. This agrees with previous studies of water adsorption on the NaCl(001) surface[101-103]. We define ΔS_{xy} as the displacement of O away from the top of the sodium site in the (100) plane. The four initial configurations where H_2O is on the boron site all

remain on the boron site after optimization (Table 7). The optimized geometry is shown in Figure 5(b). The optimized adsorption energies and geometry parameters for the 16 initial configurations are summarized in Table 6 and Table 7.

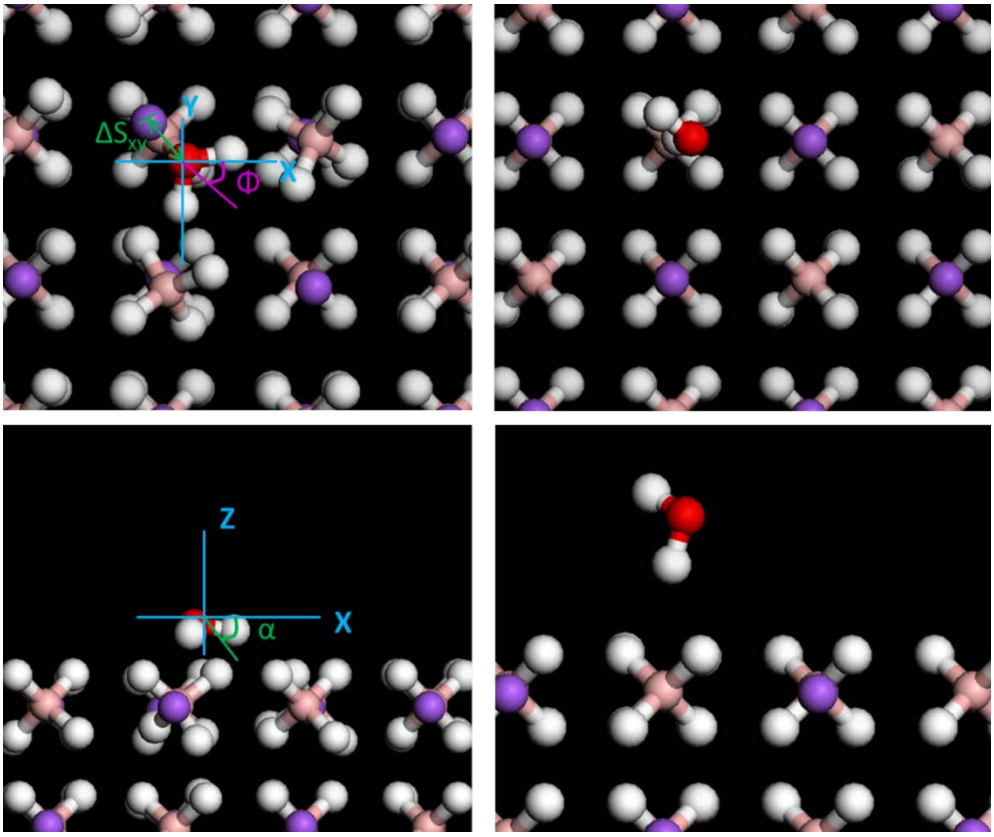

(a) (b)

Figure 5. Top (upper panels) and side (lower panels) views of optimized adsorption geometries for H_2O on (a) sodium and (b) boron sites. The top and side views for (a) define three parameters that characterize the geometry of H_2O adsorbed on the Na site: α is the tilt angle between the H_2O plane and $NaBH_4(100)$; Φ is the azimuthal angle between the [010] direction and the projection of the H_2O dipole vector onto the (100) surface; ΔS_{xy} is the displacement of O away from the top of the sodium site. In (b) the water adsorbed above boron site has one H pointing to the boron site with the H_2O plane perpendicular to $NaBH_4(100)$. The X, Y and Z axis notation corresponds to the [010], [001] and [100] vectors of the cubic crystal, respectively. The X-Y, X-Z, and Y-Z planes correspond to the (100), (001) and (010) crystal lattice planes.

Table 6. Adsorption energies (E_{ads}) and geometries for H_2O monomer starting from different initial adsorption sites (hollow, bridge and sodium) and H_2O orientations. The initial orientations, A-D, are defined in Figure 4. The $O\text{-}Na^+$ is the distance between oxygen in H_2O and nearest Na^+ on the surface. ΔS_{xy}, α, and Φ are defined in Figure 5(a). θ is the H-O-H angle of the adsorbed H_2O molecule. $H_1\text{-}H_2$ and $H_1'\text{-}H_2'$ are the distances between the H atoms in H_2O (H_1 and H_1') and the two nearest H atoms in the nearest BH_4^- groups (H_2 and H_2').

Initial Adsorption Site	Initial H_2O Configuration	E_{ads} [eV]	$O\text{-}Na^+$	ΔS_{xy}	α	Φ	θ	$H_1\text{-}H_2$	$H_1'\text{-}H_2'$
Hollow Site	A	-0.71	2.343	1.113	15	48	102	1.817	1.893
	B	-0.71	2.338	1.133	19	50	102	1.779	1.913
	C	-0.71	2.340	1.070	17	45	102	1.870	1.879
	D	-0.71	2.335	1.100	17	50	102	1.785	1.935
Bridge Site	A	-0.72	2.337	1.150	16	46	102	1.836	1.851
	B	-0.74	2.337	1.184	19	131	105	1.930	2.141
	C	-0.72	2.341	1.132	17	47	102	1.841	1.885
	D	-0.74	2.358	1.167	20	131	105	1.946	2.165
Sodium Site	A	-0.71	2.330	1.136	18	51	102	1.762	1.934
	B	-0.73	2.346	1.173	20	46	106	2.012	2.039
	C	-0.71	2.341	1.074	16	47	102	1.847	1.919
	D	-0.71	2.327	1.128	18	50	102	1.770	1.927

Table 7. Adsorption energies (E_{ads}) and geometries for H_2O monomer starting from the boron adsorption site with various H_2O orientations. H_1-B is the distance between hydrogen in adsorbed H_2O and the nearest boron. ΔS_{xy} is the displacement of O away from the top of the boron site. H_1-H_2, H_1-H_2' are the distances between hydrogen (H_1) in adsorbed H_2O and the two hydrogens (H_2 and H_2') in the nearest BH_4^- group. Definitions of α and θ are given in Table 6.

.Initial H_2O Configuration	E_{ads} (eV)	H_1-H_2	H_1-H_2'	H_1-B	ΔS_{xy} (Å)	α (°)	θ (°)
A	-0.25	2.045	2.019	2.461	0.452	98	105
B	-0.27	1.946	1.99	2.373	0.73	76	105
C	-0.25	1.971	2.019	2.412	0.434	81	105
D	-0.25	2.015	2.043	2.46	0.374	94	105

The adsorption energy is defined as:

$$E_{ads} = E[(\mathrm{NaBH_4}(100) + \mathrm{H_2O})_{relaxed}] - E[(\mathrm{NaBH_4}(100)_{relaxed}] - E[(\mathrm{H_2O})_{gas}] \qquad (3.2)$$

where $E[\mathrm{NaBH_4}(100) + \mathrm{H_2O}]_{\mathrm{relaxed}}$, $E[\mathrm{NaBH_4}(100)_{\mathrm{relaxed}}]$, and $E[(\mathrm{H_2O})_{\mathrm{gas}}]$ are the total energies of the adsorption system after optimization, the optimized $NaBH_4(100)$ pristine slab, and a gas phase water molecule, respectively. The pristine α-$NaBH_4(100)$ slab has two complementary termination surfaces, due to the different orientations of the BH_4^- group in ground state bulk α phase structure[88]. All BH_4^- groups have the same orientation on termination surface I, but alternating orientation on termination surface II, as shown in Figure 6. It is necessary to test the H_2O adsorption on the two different termination surfaces I and II. H_2O with configuration A initially on the hollow site of surface I gives an adsorption energy of -0.71 eV (Table 6), and the same water configuration on surface II gives E_{ads} = -0.68 eV, which is similar to the energy for surface I. In the remainder of the paper all calculations are based on surface I.

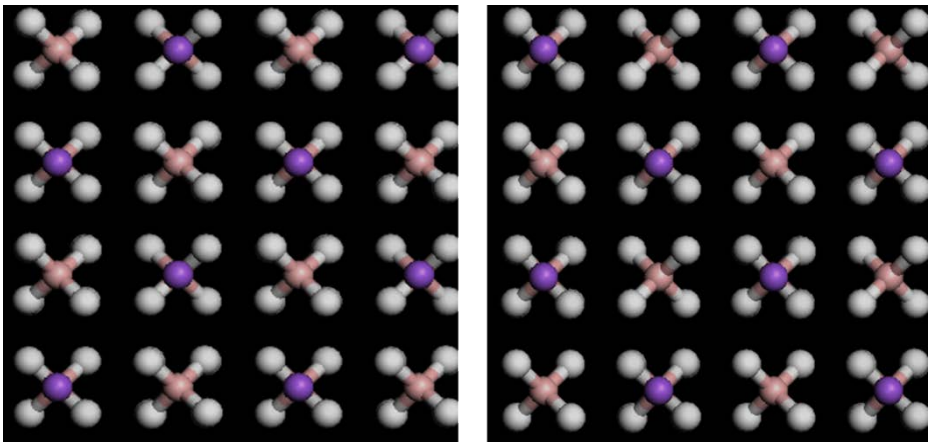

(I) (II)

Figure 6. Top view of two complementary termination surfaces (I) and (II) of $NaBH_4$ (100) surface

The adsorption energies for the 12 sodium sites given in Table 2 vary from -0.71 eV to -0.74 eV. Seven of the structures have energies of -0.71 eV, two have -0.72 eV, one has an energy of -0.73 eV, and two have -0.74 eV. For comparison, we also calculated water monomer adsorption without dispersion interactions. The results from the PW91 functional show similar adsorption geometries to those computed from DFT-D2, but the adsorption energy for the most favorable site is -0.52 eV, which is significantly less attractive compared with the DFT-D2 results. Roughly speaking, the vdW interactions add about -0.2 eV to the adsorption energy.

We have computed the vibrational frequencies for four of the 12 systems having different adsorption energies: (hollow site + water configuration A), (bridge site + water configuration B), (bridge site + water configuration C) and (sodium site + water configuration B). The vibrational frequencies for H_2O and all the atoms in the top layer of $NaBH_4$(100) for each of these configurations are real (no imaginary modes), indicating that the geometries correspond to different local minima. This implies that the energy landscape of the $H_2O/NaBH_4$(100) system is complex, having several different but similar local minima.

Our DFT optimized gas phase geometry of H_2O has a O-H bond distance of 0.972 Å and an H-O-H bond angle, θ, of 104.58°. The value of θ for adsorbed H_2O molecules on the sodium site are within ±2° of the gas phase value. This implies that the electronic structure of H_2O is not greatly perturbed from that of the gas phase upon adsorption. We note that for the systems with E_{ads} = -0.71 eV and -0.72 eV that θ=102°. In contrast, the two systems with E_{ads} = -0.74 eV have θ=105°, and for E_{ads} = -0.73 eV θ=106°. Thus, the most strongly bound molecules have bend angles that are closest to the gas phase value. This implies that one reason the binding energy is smaller in magnitude is the increased strain energy of H_2O. We observe that to two significant figures all the systems with E_{ads} = -0.71 eV and -0.72 eV have ΔS_{xy}=1.1 Å, while the systems that are slightly more strongly bound have ΔS_{xy}=1.2 Å. There are smaller differences in the O-Na^+ distances reported in Table 6 compared with changes in ΔS_{xy}. The largest change in the O-Na^+ distance is 0.03 Å, while for ΔS_{xy} it is 0.11 Å, so the larger value of ΔS_{xy} does not necessarily translate into smaller electrostatic interaction due to larger distances to the sodium charge center. The tilt angle α lies in the range 15° to 20° and does not seem to follow any trends with respect to the adsorption energy. In all cases, H atoms in water plane are pointing toward the surface. The water plane tilt combined with ΔS_{xy} facilitates simultaneous O···Na^+ and O-H···H-B interactions. Note that the attractive dihydrogen interaction is due to the partially positively charged H in H_2O being attracted to the partially negatively charged H in BH_4^-. Our calculated H···H distances lie in the range 1.77 ~ 2.17 Å, as reported in Table 6. These values are consistent with the dihydrogen bond length reported for the $NaBH_4 \cdot 2H_2O$ crystal structure as determined by experiments of 1.77 ~ 1.95 Å[29] and from theoretical calculations of 1.8 Å[96]. Duffin et al. studied aqueous $NaBH_4$ solution by X-ray spectroscopy and found an uncharacteristically narrow adsorption attributed to the formation of dihydrogen bonds between

BH_4^- and solvent water, where the dihydrogen bond length was found to be less than 2.1 Å[104]. Similarly, Custelcean et al. reported $NaBH_4 \cdot 2H_2O$ and $NaBD_4 \cdot 2D_2O$ crystal structure with close dihydrogen contacts of 1.79, 1.86, and 1.94 Å. These bond lengths are shorter than twice the vdW radius of a hydrogen atom (1.2 Å), and hence demonstrated the existence of O-H···H-B dihydrogen bonds[28]. To the best of our knowledge, our calculations are the first to show O-H···H-B dihydrogen bonding for H_2O adsorbed process on the $NaBH_4$ surface.

Adsorption of H_2O on the boron atop site gives much weaker binding energies, with E_{ads} in the range of -0.25 to -0.27 eV, as shown in Table 7. As with the sodium site adsorption, the O atom of H_2O does not lie exactly above the B atop site. However, the ΔS_{xy} values are much smaller than for the Na site adsorption (cf. Table 6 and Table 7). The tilt angle is close to 90° for these configurations and all have one H atom pointing toward the B atom, as indicated by the H_1-B distance listed in Table 7. The interaction energy for boron site adsorption appears to be dominated by formation H_2O-BH_4^- dihydrogen bonds. Comparing the adsorption energies for sodium and boron sites, we deduce that the electrostatic interaction between O and Na^+ contributes more to the binding energy than the dihydrogen bond, since only the latter interaction is present in boron site adsorption and the E_{ads} values are less than half as attractive as for the sodium site.

3.2.2.2 Water cluster adsorption.

We have computed the adsorption energies for co-adsorption of two H_2O molecules on $NaBH_4$(100). We started from seven different initial configurations and found that the optimized geometries always result in both H_2O molecules adsorbed on sodium sites. The configurations with the least and most favorable adsorption energies are shown in Figure 7(A) and (B), respectively. The adsorption energies only differ by 0.05 eV per H_2O molecule.

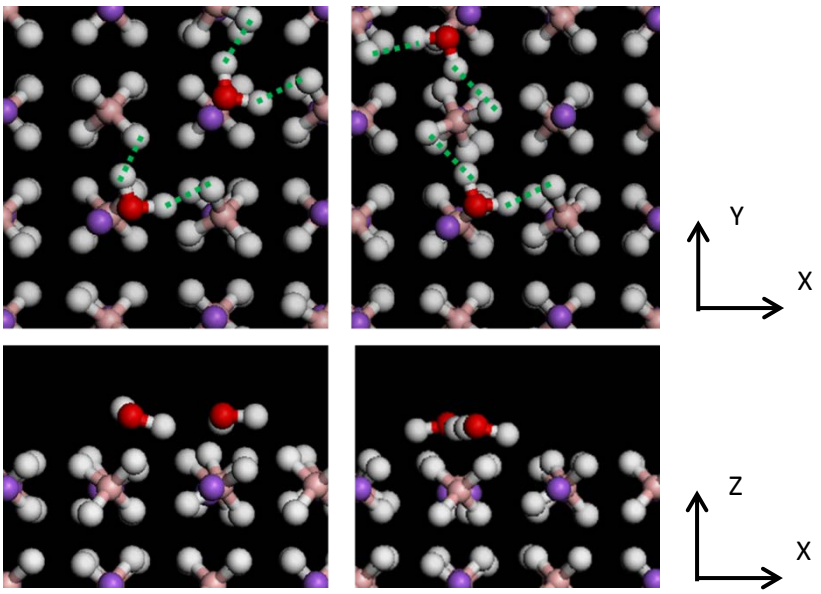

(A) (B)

Figure 7. Top (upper panels) and side (lower panels) views of water dimer adsorption geometries having the least (A) and most (B) favorable adsorption energies out of seven different geometries. The binding energies differ only by 0.05 eV per H_2O. The green dashed lines illustrate dihydrogen bonds.

Discussion of the adsorption energy necessitates a digression on the reference state for the isolated slab in the definition of E_{ads}. In equation (3.2) we used the relaxed pristine slab as the reference. However, optimization of a surface with multiple adsorbed water molecules leads to significant rotation of one or more BH_4^- groups, which distorts the surface relative to the pristine slab. One then has the choice of using the relaxed pristine surface or the relaxed distorted surface without adsorbed H_2O as the reference energy for the slab. For adsorption of a single H_2O these two definitions are identical, since the BH_4^- groups are only slightly perturbed so that the distorted surface relaxes back to the pristine configuration. However, when two or more water molecules are adsorbed on the surface BH_4^- groups tend to rotate such that relaxation of the

distorted surface without H_2O leads to new local minima. As an example, the configuration shown in Figure 7(B) exhibits rotation of the BH_4^- that lies between the two adsorbed water molecules by 62° caused by the formation of two dihydrogen bonds (one from each neighboring H_2O). Relaxation of this distorted surface goes to a local minimum with that BH_4^- group rotated by 90° from its initial position in the pristine slab. The reason that this is important is that the $NaBH_4$(100) surface shown in Figure 6(I) with all the BH_4^- groups having the same orientation is not the lowest energy configuration, although it is the lowest energy configuration for the bulk cubic structure[88]. $NaBH_4$(100) has a very complex energy landscape with many near-degenerate minima due to rotations of the surface BH_4^- groups. To illustrate and quantify this energy landscape we manually rotated various numbers of BH_4^- groups by 90° on the top layer and calculated the energy of the relaxed slab in each case. There are eight BH_4^- groups on the surface and these can be identified by row and column indices as shown in Figure 8. The energies of relaxed slabs having from zero to four rotated BH_4^- groups are given in Table 8. The energies listed in Table 8 are relative to the pristine (0 rotated) surface. We found that rotation of any number of BH_4^- groups (up to four) results in a lowering of the energy upon relaxation. Note that these energies are relatively large, ranging from -0.24 to -0.38 eV, which is roughly half the adsorption energy of a single H_2O (see Table 6). This is a critical point because we have found that adsorption of four or more water molecules can lead to approximately 90° rotation of one or more BH_4^- groups, hence the distorted slab in these cases can have an energy that is lower than the pristine slab. If one were to use the pristine slab as reference this would lead to an artificial lowering of the adsorption energy. Therefore, we define the adsorption energy per water for a cluster of *n* water molecules adsorbed on $NaBH_4$(100) as

$$E_{ads} = \frac{1}{n}\{E[(\mathrm{NaBH_4}(100) + n \times \mathrm{H_2O})_{relaxed}] - E[(\mathrm{NaBH_4}(100)_{relaxed}] - n \times E[(\mathrm{H_2O})_{gas}]\} \quad (3.3)$$

where $E[(NaBH_4(100)+nH_2O)_{relaxed}]$, $E[NaBH_4(100)_{relaxed\text{-}dist}]$ and $E[(H_2O)_{gas}]$ are the total energies of the adsorption system after optimization, the optimized $NaBH_4(100)$ distorted slab, and a gas phase water molecule, respectively.

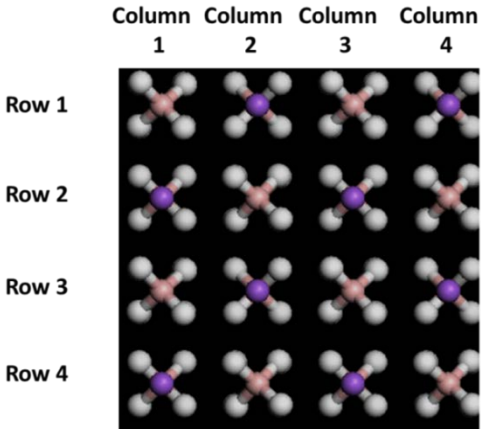

Figure 8. The notation of surface BH_4^- groups on surface I in Figure 6. For example, the BH_4^- group in row 3 and column 1 is denoted as (3,1).

Table 8. Energies of reconstructed $NaBH_4$(100) surfaces relative to the pristine surface. The notation of BH_4^- groups on surface is shown in Figure 8.

Number of rotated BH_4^- groups	Description of Top Surface	Relative slab energy (eV)
0 (Pristine)	All BH_4^- have the same orientation	0
1	Any single BH_4^- rotated by 90°	-0.24
2	Pair with Na^+ in-between them, e.g., (1,1) and (1,3)	-0.33
	Neighboring BH_4^-, e.g., (1,1) and (2,2)	-0.29
	Pair with another BH_4^- in-between them, e.g., (1,1) and (3,3)	-0.32
3	Rotated BH_4^- forming a straight line, e.g., (1,1), (2,2) and (3,3)	-0.33
	Rotated BH_4^- forming a triangle, e.g., (3,3), (4,2) and (4,4)	-0.34
4	Rotated BH_4^- forms a straight line, e.g., (1,1), (2,2), (3,3) and (4,4)	-0.34
	Rotated BH_4^- forms a square, e.g., (1,3), (2,2), (2,4) and (3,3)	-0.35
	Rotated BH_4^- forms an augmented triangle, e.g., (2,2), (3,3), (4,2) and (4,4)	-0.38

Using the definition of E_{ads} given in Equation (3.3), we find E_{ads} = -0.62 eV for the geometry shown in Figure 7(A) and -0.67 eV for that shown in Figure 7(B). Both structures include two $O\cdots Na^+$ contacts and four dihydrogen bonds (as shown by green dashed lines in Figure 7). The average distances of $O\cdots Na^+$ and dihydrogen bonds are 0.02 Å shorter in the structure with the more favorable adsorption energy. We have computed the charge density difference for the structure in Figure 7(B) and plotted the results in Figure 9. The charge density

difference is defined as the difference between the electron density of the system (with H_2O) and the sum of the electron densities of the isolated surface and isolated H_2O molecule computed with their atomic positions held fixed in the adsorbed system geometry. The cyan colored regions in Figure 9 indicate charge density depletion and the yellow color indicates charge density accumulation. We see from Figure 9 that the interaction between adsorbed H_2O and the surface is mainly due to charge transfer. Specifically, the H atoms in BH_4^- donate charge to the H atoms in H_2O through the dihydrogen bonds. We note that the extent of charge transfer is greater for the (1,1) and (3,3) BH_4^- groups than for the (2,2) group (using the notation of Figure 8). This is likely due to the (2,2) group participating in two dihydrogen bonds, and hence having to divide the electron transfer between two different water molecules. The formation of dihydrogen bonds explains why the H_2O molecules are adsorbed with the tilt angle of the H_2O plane such that H atoms are lower than the O atom.

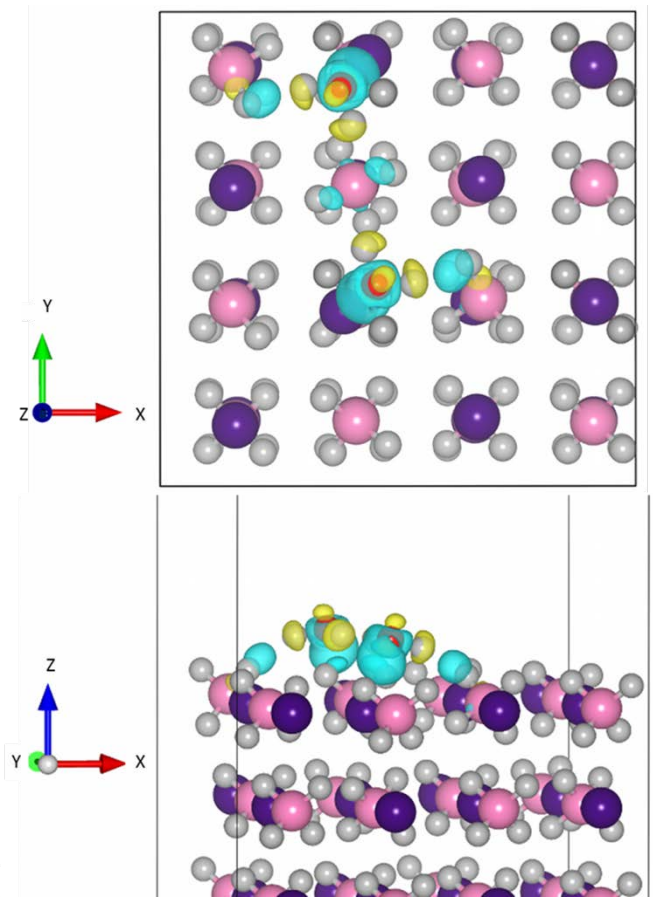

Figure 9. Charge density difference plots for two H_2O adsorbed on $NaBH_4(100)$, corresponding to the optimized geometry shown in Figure 7(B). Cyan colored regions indicate charge density depletion, and yellow colored regions indicate charge density accumulation. An isovalue of $\pm 2.0 \times 10^{-3}$ e/Bohr^3 has been applied to represent the isofurface. Purple, pink, red, and grey balls are Na, B, O and H, respectively.

The number of possible configurations for water adsorption increases dramatically as the number of water molecules on the surface increases. Therefore, we adopted a statistical sampling approach to identify energetically favorable configurations. As discussed in the Computational Methods section, we have used ab initio MD to generate candidate structures for adsorption of four or more H_2O molecules. The adsorption energies for adsorption of two through 64 water molecules on $NaBH_4(100)$ are listed in Table 9. The top and side view of 4 H_2O and 8 H_2O cluster adsorption geometry is shown in Figure 10. Water-water interactions, including hydrogen

bonding, become more important as the coverage of water on the surface increases. We can decompose the adsorption energy into water-surface interactions and water-water interactions. The water-water interaction per water, E_{ww}, is defined as

$$E_{ww} = \frac{1}{n}\{E[(H_2O)_{network}] - n \times E[(H_2O)_{gas}]\} \qquad (3.4)$$

where $E[(H_2O)_{network}]$ is the total energy of water with the geometry fixed in the adsorbed configuration, but without the surface, $E[(H_2O)_{gas}]$ is the optimized energy of an isolated water molecule at gas phase, and n is the number of water molecules. The water-surface interaction, E_{ws}, is defined as the difference between E_{ads} and E_{ww}. We see from Table 9 that E_{ads} is essentially independent of water coverage. E_{ww} is slightly positive for the water dimer, indicating a slight net repulsive interaction between the two water molecules. This repulsive interaction is likely due to the two adsorbed H_2O molecules being oriented such that the OH groups are roughly pointed toward each other, as can be seen in Figure 7(B). This gives an unfavorable dipole-dipole interaction, with the two partially positively charged H atoms 3.2 Å away from one another. The E_{ww} values for four and eight adsorbed H_2O are both much less favorable than optimized gas-phase water interactions for the same size clusters, as can be judged by the fewer hydrogen bonds in the adsorbed clusters relative to gas phase clusters[105-107]. This clearly indicates that the surface interactions dominate over the water-water interactions at low coverages.

Table 9. Adsorption energies (per H_2O), E_{ads}, and water-water interaction energies (per H_2O), E_{ww}, for submonolayer through multilayer water coverage on $NaBH_4(100)$. The water-surface interaction energy is $E_{ws} = E_{ads} - E_{ww}$. All energies are in eV.

Number of H_2O	E_{ads}	E_{ww}	E_{ws}
2	-0.67	0.02	-0.69
4	-0.67	-0.17	-0.5
8	-0.71	-0.32	-0.39
16	-0.72	-0.44	-0.28
32	-0.69	-0.54	-0.15
48	-0.70	-0.63	-0.07
64	-0.71	-0.64	-0.07

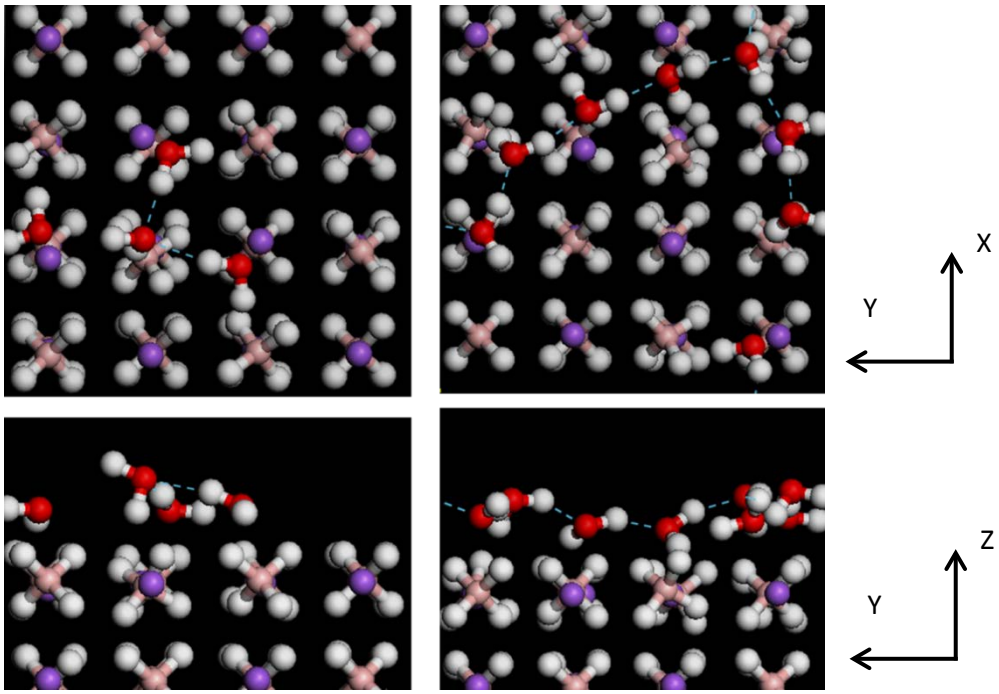

Figure 10. Top and side view of 4 and 8 H_2O adsorption geometry. The blue dashed lines illustrate hydrogen bonds.

3.2.2.3 Multi-layer water adsorption

The 2×2 supercell surface studied in this work has 16 adsorption sites (8 sodium and 8 boron sites) and so we consider 16 H_2O as a monolayer (ML). We have analyzed the hydrogen bonding structure for the lowest energy configuration for the ML and found that water molecules adopt ring-like structures on the surface. We have identified rings of 3, 5, 6 and 7 H_2O molecules, as shown in Figure 11. The structure of the $(H_2O)_3$ ring agrees with the lowest energy gas phase water trimer structure[108]. In contrast, the structures of other clusters are different from lowest energy gas phase isomers[106-109]. These non-optimal water clusters arise because of the importance of water-surface interactions, which can be quantified by noting from Table 9 that E_{ww} and E_{ws} are the same order of magnitude for systems with eight and 16 H_2O. When more than 16 H_2O are adsorbed, a complex H_2O network is formed as shown in Figure 12. The adsorption energies of multi-layer water (32, 48, and 64 H_2O) are summarized in Table 9. While the adsorption energy per H_2O is roughly independent of water coverage, we note that the water-water interactions dominate and water-surface interactions contribute only a small amount. The water-water interaction appears to converge to about -0.63 eV per water, being essentially constant for both 48 and 64 water molecules on the surface (Table 9). To verify that this value is converged to the bulk water-water energy we have computed the average E_{ww} for bulk water at 0 K by carrying out AIMD for liquid water at 300 K at a density of about 1 g/cm^3 for 8 ps and then minimizing 13 snapshots from the final 6 ps of the simulation to their local minima. This approach gives E_{ww} = -0.60 eV, which confirms that E_{ww} for the thickest slabs of water in Table 9 have reached the bulk value. As a check of the accuracy of our calculations we have estimated the enthalpy of vaporization at 300 K as computed from DFT-D2 by taking the average of the single point energies from the 300 K AIMD simulations as liquid phase internal energy and

assuming ideal gas behavior for gas-phase H_2O. This gives an enthalpy of vaporization (including the PV term) of 0.49 eV, which is in very good agreement with the value computed from the NIST Webbook of 0.46 eV.[110] This gives us confidence in the values computed for the water-water and water-surface interactions. Hence, we deduce that the water-surface and water-water interactions are very similar, making the adsorption of a thick, bulk-like film of water energetically feasible, resulting ultimately in deliquescence. In contrast, calculations of H_2O adsorption on NaCl by Yang et al.[101] show that the interaction of H_2O with the NaCl surface is actually weaker than the water-water interactions in the monolayer or multilayer. This indicates that NaCl has a weaker surface potential and hence would require a larger RH to form a multilayer of H_2O on the surface.[111] We also note that adsorption of multiple H_2O molecules leads to reconstruction of the $NaBH_4(100)$ surface through rotation of BH_4^- groups by about 90°. This roughening of the surface is a precursor to dissolution of $NaBH_4$ into the film of water adsorbed on the surface and hence can be regarded as the earliest stage of deliquescence.

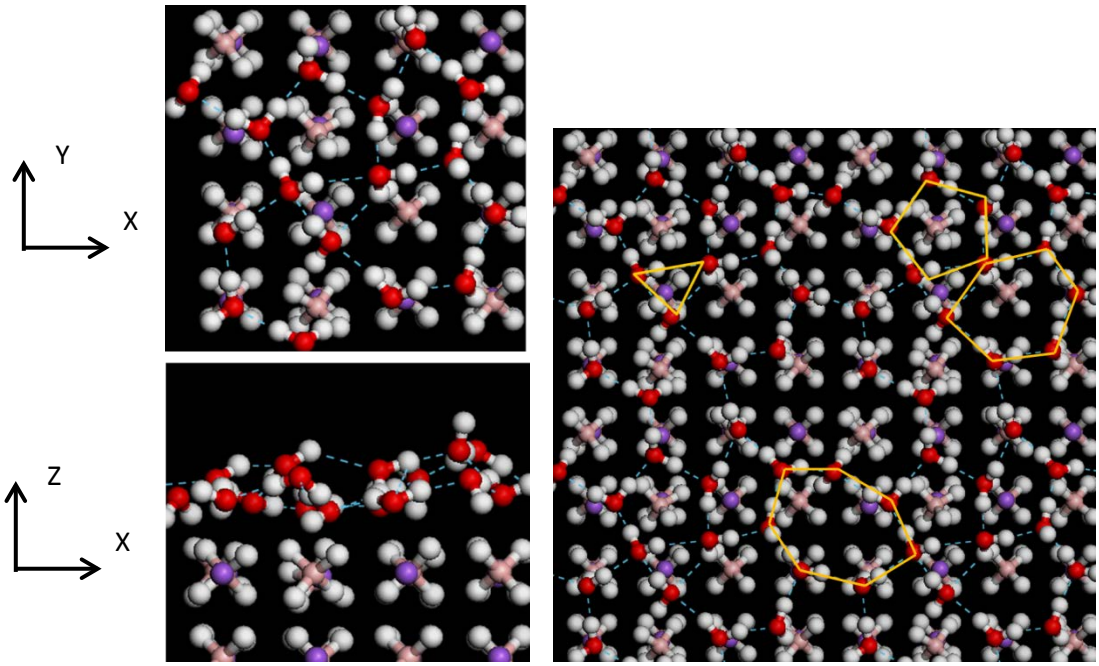

(A) (B)

Figure 11. (A): Top and side views of 16 H_2O adsorption on $NaBH_4$(100). (B): 2×2 supercell of the top view in (A) with 3, 5, 6 and 7 H_2O ring structures shown by yellow lines. The blue dashed lines illustrate hydrogen bonds.

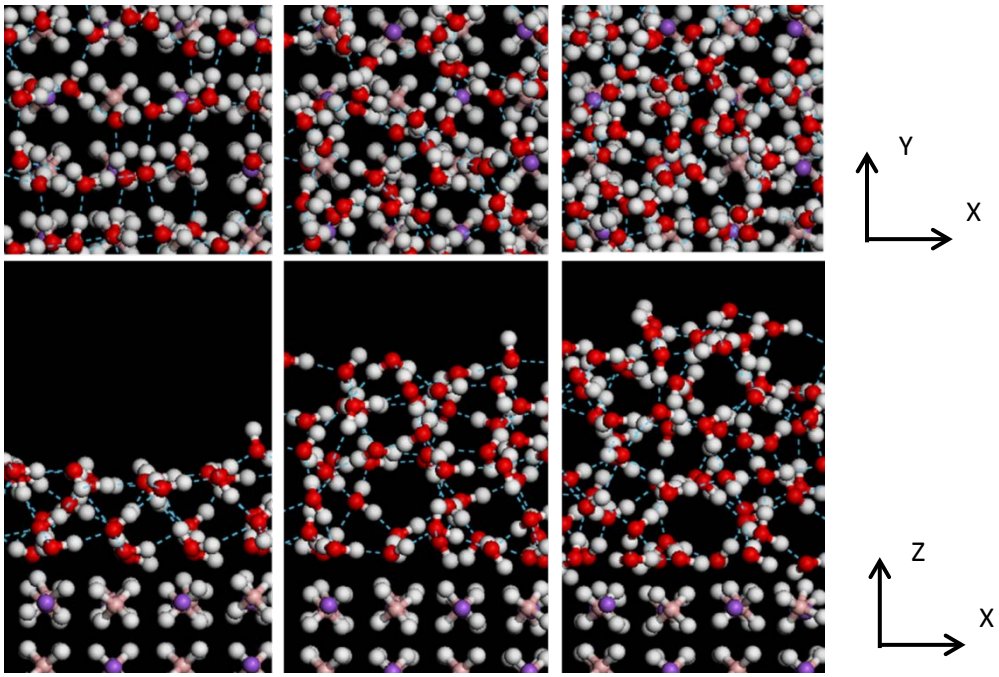

Figure 12. Top and side view of 32 (left), 48 (center), and 64 (right) H_2O molecules adsorb on $NaBH_4(100)$. The blue dashed lines illustrate hydrogen bonds.

To summarize, water adsorption on $NaBH_4(100)$ was studied from first principles DFT calculations with inclusion of dispersion corrections. The H_2O monomer is favorably adsorbed above the sodium site through O···Na and O-H···H-B attractions with hydrogen atoms, resulting in water adsorbing such that the plane of water is tilted with H atoms down. The O-H···H-B attraction is consistent with the dihydrogen bond found in the $NaBH_4 \cdot 2H_2O$ crystal and in aqueous $NaBH_4$. The adsorption energy per water molecule is roughly independent of water coverage, suggesting that formation of a thick water film on the surface is energetically favorable. Adsorbed H_2O molecules facilitate $NaBH_4(100)$ surface reconstruction through 90° rotation of BH_4^- groups in the surface. This process increases the roughness of the surface and promotes dissolution of $NaBH_4$ into the adsorbed water. Hence, H_2O-promoted surface reconstruction may be considered a preliminary step in the deliquescence process.

3.3 DELIQUESCENCE PROCESS

3.3.1 Initial stage of deliquescence process

The initial stage of deliquescence is fundamental for onset of deliquescence process and following hydrolysis reaction. Therefore characterization of key steps leading to deliquescence is significant for understanding of $NaBH_4$ crystal properties and hydrolysis reaction condition.

AIMD calculations were performed using a microcanonical ensemble with a time step of Δt = 0.3 fs at 330 K, 400 K, 450 K, 500 K and 700 K. The total simulation time was about 4.5 ps. Calculations at 700 K clearly shows the four initial steps of the process. The first step is roughening of the $NaBH_4$ surface. The $NaBH_4$ surface is no longer flat after several layers of water molecules adsorbed on top, due to the interaction between water and $NaBH_4$. The second step is for one or more BH_4^- ions to leave the surface and diffuse into the water phase. This leaves vacancies for H_2O molecules to penetrate into the $NaBH_4$ solid. Hence, the third step is for H_2O molecules to diffuse into BH_4^- vacancies and then penetrate down to deeper layers of $NaBH_4$. Then fourth step is for Na^+ ions to diffuse into water phase to form a charge neutral $NaBH_4$ solution. Finally, a new section forms at the interface of water and the solid $NaBH_4$ surface.

Then we calculated the radial distribution function (RDF) of the mixture section in the deliquescence process, and compared our results to the RDF of a $NaBH_4$ solution that we simulated separately. The $NaBH_4$ solution was simulated by placing 3 $NaBH_4$ and 29 H_2O molecules into a $10\times10\times10$ $Å^3$ box [$NaBH_4$ (wt%) = 17.86%]. The RDF comparison is given in Figure 13, where the RDF for the B-O pair shows how water density varies as a function of

distance from the BH_4^- group, and the RDF of the Na-O pair tells how water density changes as a function of distance from the Na^+ group. The RDF curves for B-O and Na-O both show similar trends in deliquescence process and in solution, *i.e.* the position of the first peak and the shape of the curve, which means the environment of BH_4^- and Na^+ ions in deliquescence are bulk solution like. This is surprising because there are only a few layers of water molecules on top of the $NaBH_4$ surface. Therefore, we predict that only a small amount of water is required to create a bulk-like environment for ions that go into the liquid phase. Additionally, the $NaBH_4$ interface does not dramatically impact the structure of the solution in contact with that interface.

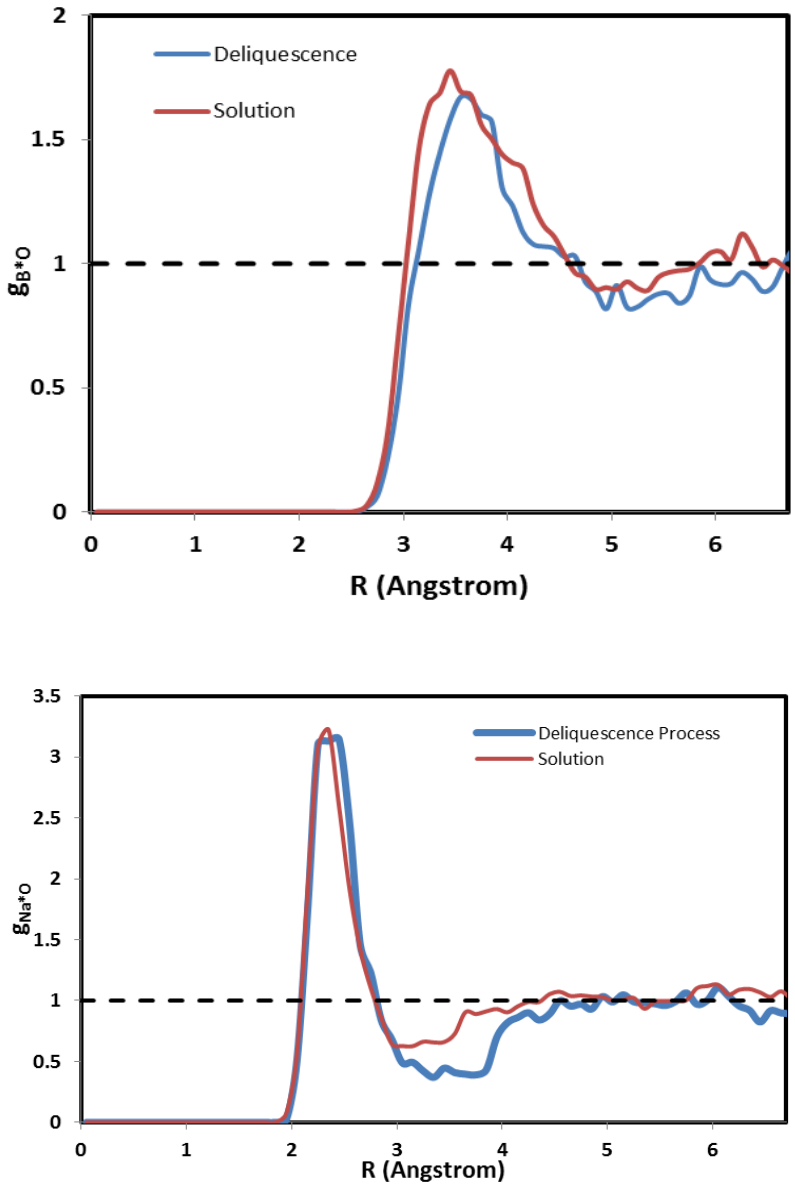

Figure 13. Radial distribution function of deliquescence process and solution

The deliquescence process does not occur in similar AIMD calculations at lower temperatures (330 K, 400 K, 450 K, 500 K) within the same simulation time. This indirectly indicates that the deliquescence rate increases with temperature at constant H_2O density, as it must.

3.3.2 Force field development for initial stage of deliquescence process

Quantitative characterization of initial deliquescence stage from simulation is useful to predict experiment deliquescence condition. To calculate Gibbs free energy change of moving Na^+/BH_4^- from crystal lattice to the bulk liquid phase of H_2O, molecular dynamics calculation at ambient temperature is required. Molecular dynamics is more powerful than AIMD on the basis of computation efficiency and sampling of the system. Force field (FF) is essential part for any kind of molecular dynamics simulation. Unfortunately, no established FF is available for $NaBH_4$ up to now. So we developed MSXX force field[112-115] (MSXX FF) for $NaBH_4$ and H_2O, and testing work is going on. The functional form of this new FF is based on Dreiding FF[79] and given in Table 10. The bond-bond cross term E_{HBH}^{RR} was added to describe the correct splitting between the ν_1 and ν_3 modes of BH_4^-, where the angle-angle cross term $E_{BHHH}^{\theta\theta}$ was added to described the splitting between ν_2 and ν_4 modes of BH_4^-, similar to those for $B(OH)_4^-$ (see Figure 40).

Table 10. MSXX Force field for $NaBH_4$ and H_2O

$$E = E^{nonbonded} + E^{valence}$$

$$E^{nonbonded} = E^{Coulomb} + E^{vdW}$$

$$E^{valence} = E_{BH}^{bond} + E_{HBH}^{angle} + E_{HBH}^{RR} + E_{BHHH}^{\theta\theta\theta}$$

$$E^{Coulomb} = C_0 \frac{q_i q_j}{\varepsilon R_{ij}}$$

$$E_{ij}^{vdW} = A\exp(-r_{ij} / \rho) - C_6 / r_{ij}^6$$

$$E_{BH}^{bond}(\theta) = \frac{1}{2} K_R (R - R_0)^2$$

$$E_{HBH}^{angle}(\theta) = \frac{1}{2} K_{angle} (\cos\theta - \cos\theta_0)^2$$

$$E_{HBH}^{RR}(R_1, R_2) = \frac{1}{2} K_{RR} (R_1 - R_0)(R_2 - R_0)$$

$$E_{BHHH}^{\theta\theta}(\theta_1, \theta_2) = \frac{1}{2} K_{\theta\theta} (\theta_1 - \theta_0)(\theta_2 - \theta_0)$$

Ab initio quantum molecular calculations used to fit FF parameters (B-H bond length, H-B-H angle and charge distribution in $NaBH_4$) were performed in Gaussian 09[116], which is an electronic structure program used to predict energies, molecular structure, vibrational frequencies and reactions in a wide variety of chemical environments. The calculated results of $NaBH_4$ (equilibrium bond length, bond coefficient, equilibrium angle, angle coefficient and charge distribution) were given in Table 11, and the basis set is aug-cc-pVTZ. Charge was fitted with CHelpG scheme[117].

Table 11. Ab initio calculation for $NaBH_4$ bond and angle properties and charge distribution in the gas phase

Level		B3LYP	MP2	CCSD(T)
B-H bond length (Å)		1.23775	1.23408	1.23999
B-H bond coefficient (kcal/(mol·Å^2))		181.0245	187.6196	192.7031
H-B-H bond angle (degree)		109.4712	109.4712	109.4712
H-B-H bond coefficient (kcal/(mol·rad^2))		36.43052	37.88225	39.46034
Charge on atom	B	-0.22913	0.61304	0.59966
	H	-0.19272	-0.40326	-0.3992

For the valence FF as given in Table 12, the six valence parameters, R_0, θ_0, K_R, K_{angle}, K_{RR} and $K_{\theta\theta}$, were adjusted to reproduce the experimental and ab initio calculation results of $NaBH_4$ crystal geometry, density, and compressibility. The atomic charges of Na^+ were fixed at its formal charge +1.0|e|, and those of B and H in BH_4^- were determined by fitting to the electrostatic potential generated from ab initio calculations from Gaussian 09. Those charges are based on a cluster calculation of BH_4^- and are not expected to be consistent with Bader charges.

Table 12. Force field valence and Coulomb parameters for $NaBH_4$ and H_2O

Bonded Interaction
R_0(Å) = 1.24
θ_0(degree) = 109.47
K_R(eV/Å^2) = 18.04903
K_{angle}(eV/rad^2) = 3.188596
K_{RR}(eV/ Å^2) = 0.572931
$K_{\theta\theta}$(eV/rad^2) = -0.001424
Coulomb
q(Na) = 1.0|e|
q(B) = 0.50666
q(H) = -0.376666
q(H_w) = 0.41
q(O_w) = -0.82

H, H_w and O_w represent hydrogen in BH_4^-, hydrogen in water, and oxygen in water, respectively.

For vdW nonbonding interaction between atoms as shown in Table 13, we were adjusted to reproduce the $NaBH_4 \cdot 2H_2O$ crystal geometry and density, BH_4^-/Na^+ and H_2O interaction in gaseous phase, and $NaBH_4$ crystal geometry, density and compressibility.

Table 13. Force field vdW parameters for element species in $NaBH_4$ and H_2O

Non-Bonded Interaction	*A (eV)*	*ρ (Å)*	*C_6 (eV/Å^6)*
H-H	147.776180	0.25804	1.361633
B-B	670.482705	0.33500	34.773672
Na-Na	3528.857711	0.26200	41.881048
H-Na	722.133684	0.26000	6.894892
B-Na	1538.194010	0.29404	38.160408
O_w-Na	5054.238310	0.246221	65.068129
H_w-Na	3234.717636	0.256878	49.012266
O_w-H	670.127119	0.26546	6.383196
H_w-H	132.932649	0.25804	1.222868
O_w-B	3716.763029	0.27784	30.007957
H_w-B	737.2911198531	0.269715118	5.7524648443

H, H_w and Ow represent hydrogen in BH_4^-, hydrogen in water, and oxygen in water, respectively.

Within above FF parameters, we calculated a density of $NaBH_4$ as 1.11621 g/cm^3 from MD calculation in LAMMPS at 298 K, which agrees with experimental density of 1.074 g/cm^3. The calculated lattice parameters at 298 K is 6.0837 Å that differs by 0.5% from our VASP calculated lattice parameter 6.0509 Å. Calculated density of $NaBH_4 \cdot 2H_2O$ using above FF is 1.10084 g/cm^3, which is consistent with experiment value[29] 1.15 g/cm^3.

The compressibility of $NaBH_4$ crystal was calculated from NPT MD simulation at 298 K in LAMMPS. The basic idea is to use the relationship between compressibility and volume fluctuation over the MD trajectory. The compressibility is defined as[118,119]

$$\chi = \frac{1}{V_0}(\frac{dV}{dP})_{V=V_0} \qquad (3.5)$$

We performed MD at eleven different pressures ranging from -0.5 GPa to 0.5 GPa at 298 K. At each pressure point, the average volume was obtained after 1 ns following a 10 ps equilibration. Compressibility at 298 K was calculated from the slope of the <P> -- <V> over V at P=0.0001 GPa (1 bar) based on Equation (3.5). The <P> -- <V> curve (see Figure 14) can be perfectly fitted to two order polynomial curve, and gives the compressibility at 0.0001 GPa to be -0.0562 GPa^{-1}. It is well known bulk modulus is defines as $B = -V(\frac{dP}{dV})_{V=V_0}$, equivalent to minus reciprocal of compressibility. Our calculated compressibility leads to bulk modulus 17.79811 GPa, which agrees with established experimental and theoretical values (see Table 3).

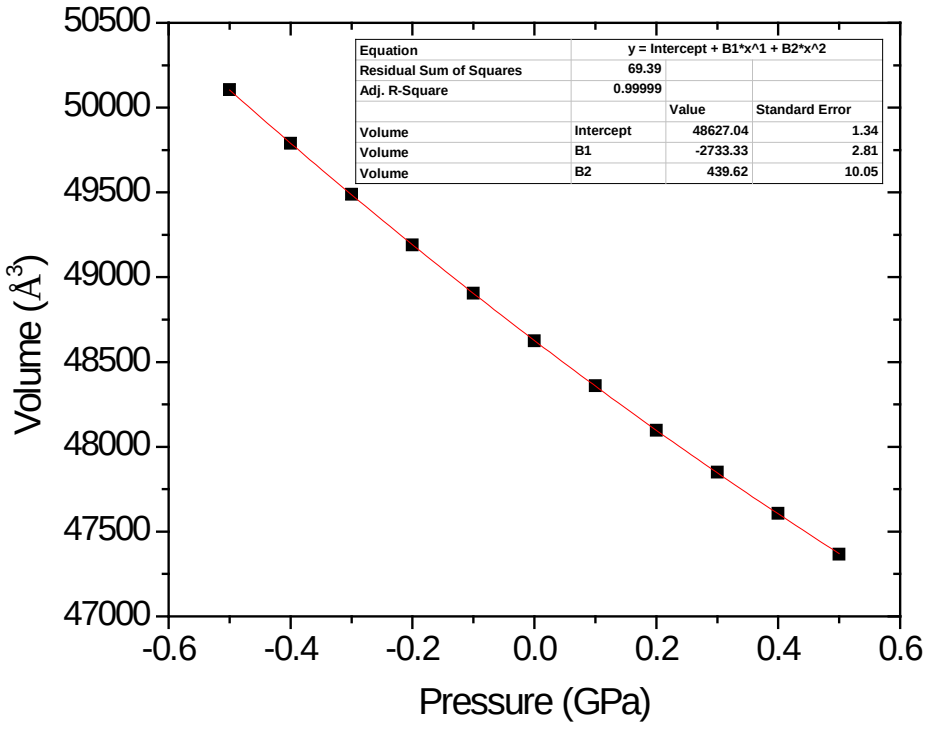

Equation	y = Intercept + B1*x^1 + B2*x^2		
Residual Sum of Squares	69.39		
Adj. R-Square	0.99999		
		Value	Standard Error
Volume	Intercept	48627.04	1.34
Volume	B1	-2733.33	2.81
Volume	B2	439.62	10.05

Figure 14. Volume change of $NaBH_4$ between pressure range (-0.5 GPa to 0.5 GPa)

Before calculating the Gibbs free energy change of moving Na^+/BH_4^- from crystal lattice to the bulk liquid phase of H_2O, we will perform more testing calculations to ensure the FF is reliable for our system. If proved to valid, this FF could be used to calculate other properties of $NaBH_4 + H_2O$ system by other researcher.

3.4 HYDROLYSIS MECHANISMS

Despite a long history of research and development, the basic mechanism of $NaBH_4$ hydrolysis reaction is not understood on a molecular level. We have performed first-principles density functional theory calculations to investigate the elementary reaction steps in aqueous $NaBH_4$ hydrolysis. Detailed understanding of these steps would be useful for reaction condition optimization, catalyst design, and ultimately for precise control of the reaction in practical applications.

cNEB[120,121] method , designed to efficiently locate the highest saddle point on the potential energy surface, was used to determine the minimum energy paths and corresponding transition states for all the elementary steps. Generalized solid-state nudged elastic band (G-SSNEB)[122] method was employed to roughly identify minimum energy pathway involving both atomic and unit-cell degrees of freedom. Based on G-SSNEB results, we carried out cNEB calculation to identify the minimum energy pathway in a cubic unit cell with only atomic position change but without cell shape and volume change. It was well-known that G-SSNEB is used for determining reaction pathway of solid-solid transformation. However, in present study, we explored its application in liquid phase reaction. The lattice constant of unit cell is from 9.5-10.5 Å, which corresponds to the minimum volume in G-SSNEB calculation. We used

combination of G-SSNEB and cNEB because there are too many degrees of freedom in our liquid phase reaction result from solvent motion and it really pushes the limit of cNEB method itself for identifying minimum energy pathway. For clarification purpose, the final presented results in this paper are based on cNEB calculation. In our calculations, Quick-Min optimizer[123] was used and the pathway is converged until the forces on all atoms were less than 0.03 eV/Å. It is noticeable that combination of explicit and implicit solvent was used for aqueous phase reaction calculation[124,125]. We did not take this approach because solvent effects are more complex in $NaBH_4$ hydrolysis system, e.g. OH- must migrate away from the product to prevent reverse reaction. This process requires long-range proton exchange across water wire that one cannot create in an implicit solvent.

The initial and final structures used to build each G-SSNEB pathway were obtained from AIMD simulation in VASP. AIMD calculations were performed in a cubic unit cell (lattice constant=10 Å) containing $1NaBH_4+33H_2O$, $2NaBH_4+31H_2O$, or $3NaBH_4+29H_2O$ at high temperature for more than 10 ps to generate a family of reaction pathways which were used as prototype to build G-SSNEB pathways.

Overall $NaBH_4$ hydrolysis reaction involves many elementary steps as summarized in Figure 15. Energy barrier profile and molecular evolvement along each step were described in following sections. Our hypothesis is that all elementary steps in $NaBH_4$ hydrolysis reaction involve very complex solvent rearrangement, including proton shuttling over relatively long distances (more than 8 Å). It also involves solution rearrangement around OH^- groups. For this reason, one cannot use the naïve approach of including a small number of water molecules and using an implicit solvent model to account for the continuum dielectric constant. Because of the complexity, one cannot expect to find actual minimum energy pathways for reactions. There are

ensembles of pathways. Our goal is to show representative mechanisms from the family or ensemble of mechanisms that exist in the real system. We argue that these ensemble members share the same salient features. However, the energies and reaction barriers are not necessarily representative of the actual energetics in the real system because energies in our calculations may be dominated by solvent rearrangement events.

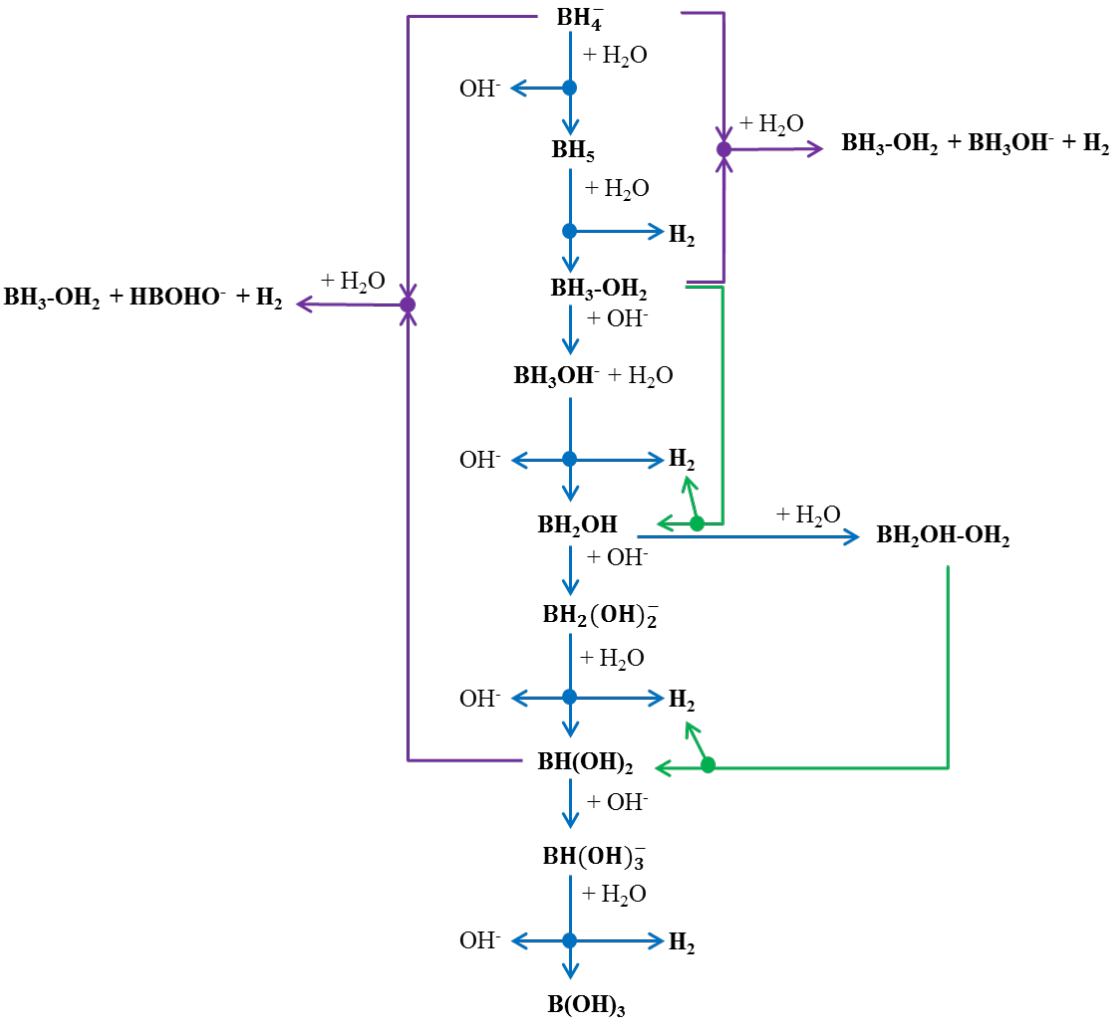

Figure 15. Reaction scheme of $NaBH_4$ hydrolysis reaction. Blue lines show reactions between hydroxyborates and H_2O; green lines for intramolecular reactions and purple lines for reactions between two hydroxyborates.

3.4.1 Reaction between hydroxyborates $BH_{4-x}(OH)_x^-$ (x= 0,1,2,3) and H_2O

$$BH_4^- + H_2O \rightarrow BH_5 + OH^- \qquad (3.6)$$

Equation (3.6) is the first step of entire BH_4^- hydrolysis process, and its energy evolution along pathway was shown in Figure 16. The calculated energy barrier of 1.03 eV is consistent with the fact that $NaBH_4$ hydrolysis in solution is very slow without catalyst. The structure change from initial to transition and final state along this reaction is illustrated in Figure 17. Here only reactant molecules are highlighted, and solvent molecules, which are not directly participating in the reaction, were shown in shadow. Certain H atoms in H_2O were colored to indicate the proton transfer process. This style applies to illustration of all reaction pathways in this paper. From initial state to transition state, BH_4^- transforms from ideal tetrahedral geometry to a structure similar to BH_5 but lacking one H atom. At transition state, 5 H_2O molecules form a chain to facilitate proton transferring from the O with H in cyan to its neighbor O with H atoms in mauve, and then to O with H atoms in lime. Therefore, the O atom closest to BH_4^- has a hydronium-like structure and the length of the O-H bond pointing to BH_4^- is increased to 1.39 Å since the H is shared by B and O atoms. The distance between that H and B is 1.56 Å. After transition state, BH_4^- obtains that H and generates BH_5 and water chain breaks to prohibit the reverse reaction, *i.e.* OH^- retrieving that H through water chain. In final state, BH_5 has a stable C_s symmetry (analogue to CH_5^+), and was previously notated as H_2BH_3 by Kreevoy *et al.*[126], because it has two relatively long and three normal B-H bond lengths, recognizable as a complex between BH_3 and H_2. The subunit of two long B-H bonds potentially evolves molecular hydrogen in further reaction steps. Our NEB calculation reveals that BH_5 with C_s symmetry as the product of BH_4^- reacting with 1 H_2O, which agrees with previous studies[126-128]. Furthermore, we improved the knowledge of this elementary step by estimating the energy barrier. BH_5 is in at least the second

solvation layer of byproduct OH^- (shown as $H_5O_3^-$ cluster in Figure 17, which is far enough to prevent the reverse reaction). The byproduct of reaction (2), OH^- group, is hydrated by 4 solvent H_2O molecules, and forms $OH(H_2O)_4^-$ with fourfold planar coordination around the O in OH^-, which is the most stable structure of OH^- group in aqueous solution[129,130] (see Figure 18).

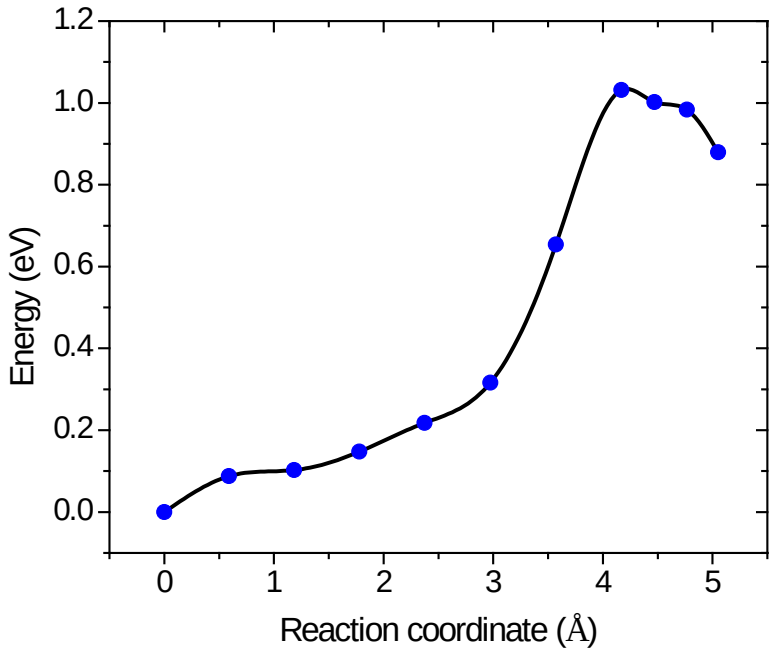

Figure 16. Density functional theory calculation of the minimum energy path for BH_4^- hydrolysis to BH_5.

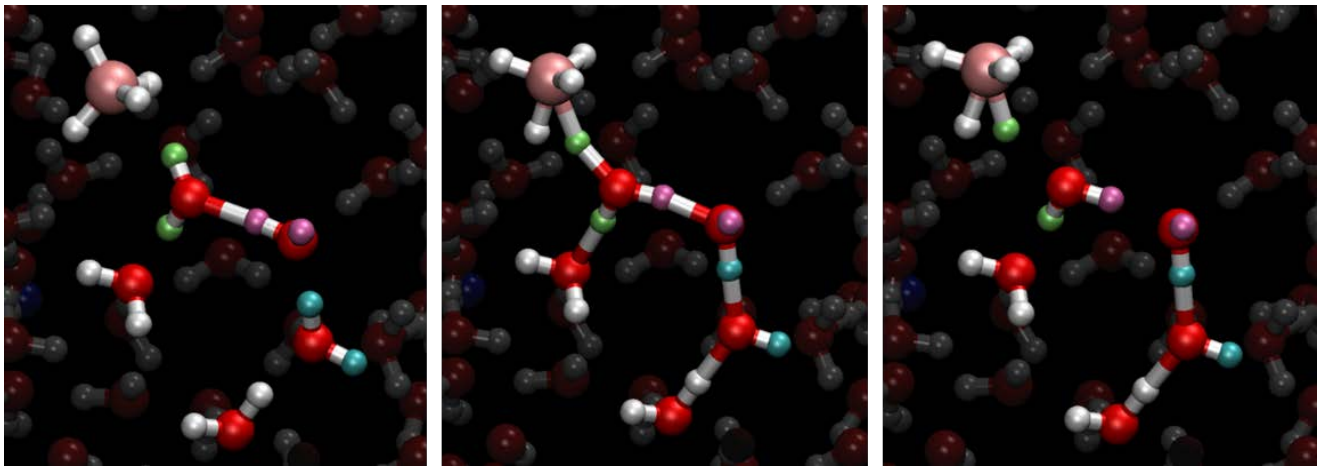

Figure 17. Structure of reactants, transition state and products in hydrolysis reaction of BH_4^- to BH_5. H atoms were colored in lime, mauve and cyan to show the proton transfer process involved in the reaction, where the two H atoms belonging to one H_2O are in the same color.

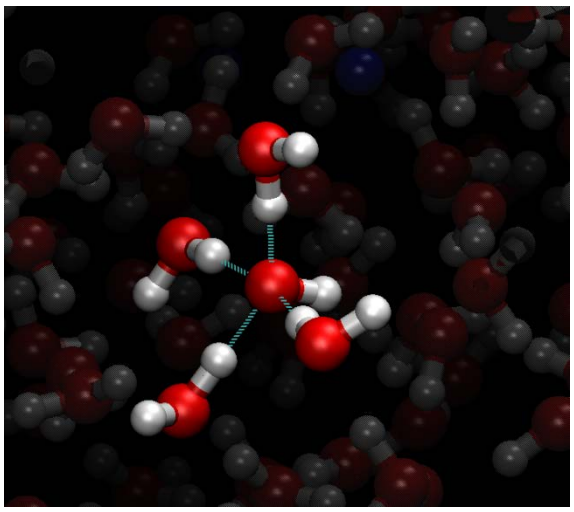

Figure 18. Structure of 4 H_2O hydrated OH^-: $OH(H_2O)_4^-$. The blue dashed lines illustrate hydrogen bond.

$$BH_5 + H_2O \rightarrow BH_3\text{-}OH_2 + H_2 \qquad (3.7)$$

The binding energy and dissociation pathway of BH_5 have been extensively studied since more 1960s[126-128,131,132]. However, only simple dissociation of BH_5 to BH_3 and H_2 was considered in most studies. As an exception, Pepperberg et al. considered solvation effects and H_2O:BH_3 complex as product of BH_5 dissociation[127], and found the solvation energy of BH_3 at the 6-31G* level to be about 6-8 kcal/mol and stabilization of BH_3:H_2O is sensitive to the choice

of basis set. In comparison, our AIMD calculation at 300 K indicates BH_3 is highly active in aqueous solution and always combine with one H_2O to form BH_3-OH_2 complex. The minimum energy pathway we found for Equation (3.7) is shown in Figure 19; and the corresponding energy barrier is 0.42 eV. The calculation also illustrate the step is exothermic, since the energy of products is 0.56 eV lower than that of reactants. The structure evolutions of reactants to products are shown in Figure 20. At transition state, BH_5 completely dissociates to H_2 and planar structure BH_3, which is known to be stable only in gas phase. After transition state, BH_3 combines with a H_2O molecule to form BH_3-OH_2 complex, which has BH_3 moiety in tetrahedral. At final state, the generated H_2 molecule is more than 2.82 Å away from B in BH_3-OH_2 complex.

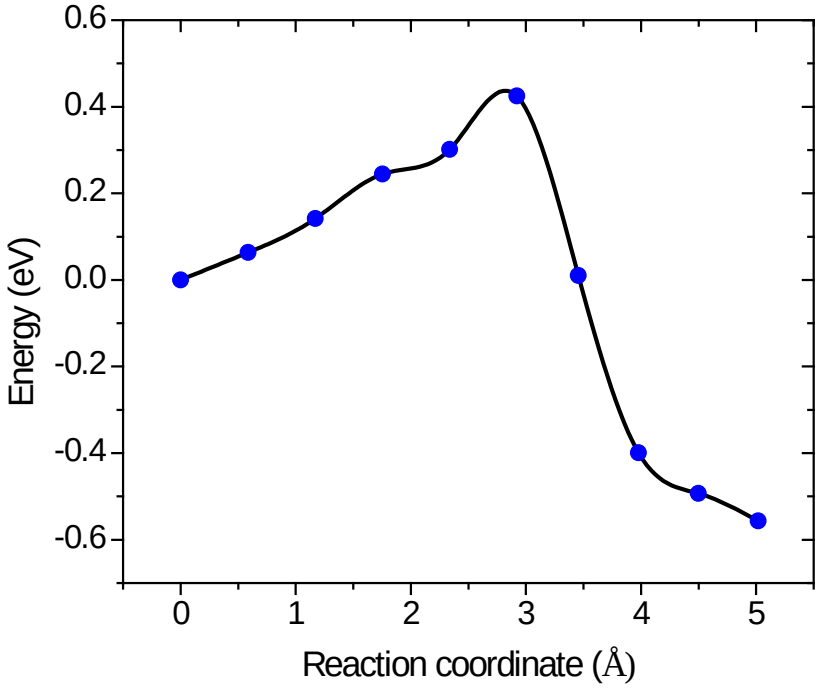

Figure 19. Density functional theory calculation of the minimum energy path for dissociation of BH_5 to BH_3-OH_2 complex and H_2.

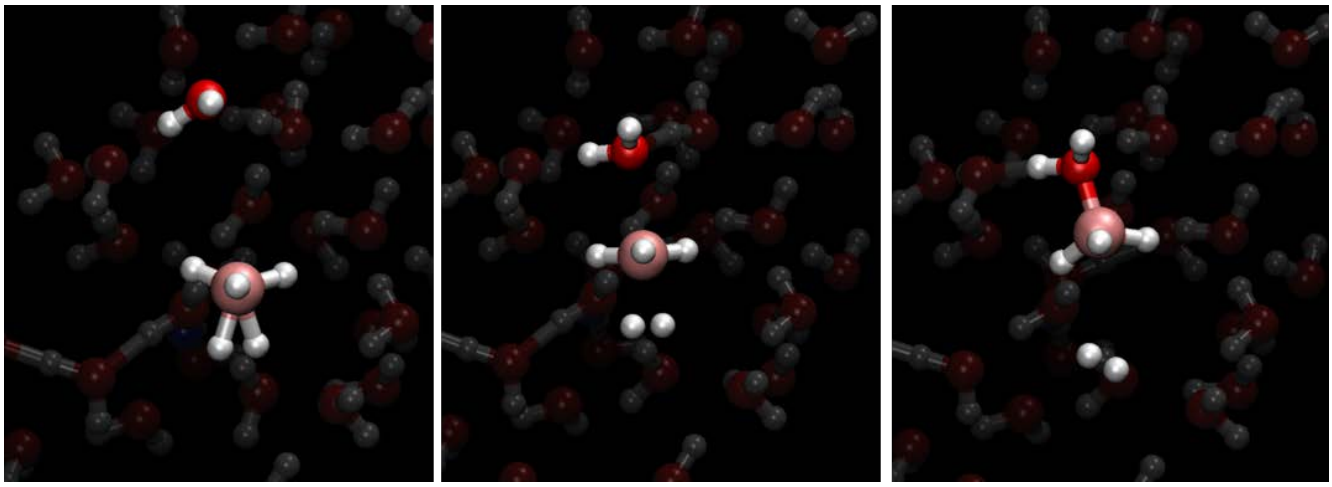

Reactants Transition State Products

Figure 20. Structure of reactants, transition state and products in BH_5 dissociation

$$BH_3\text{-}OH_2 + OH^- \rightarrow BH_3OH^- + H_2O \quad (3.8)$$

Studies about acid catalyzed $NaBH_4$ hydrolysis reaction consider the process after formation of BH_3 as $BH_3 + 3H_2O \rightarrow 3H_2 + B(OH)_3$[126,127,133,134]. In fact this is not a single step reaction but includes several elementary reaction steps and intermediates, depending on the pH of solution[60,135-137]. For spontaneous hydrolysis of $NaBH_4$ without catalyst, Andrieux et al. reported reaction $BH_4^- \rightarrow BH_3$, $BH_3 \rightarrow BH_3OH^-$ are rating determining steps and only traces of $BH_3(OH)^-$ were detected in their experiment[48]. Our cNEB calculation results indicate from the energy from BH_3-OH_2 to BH_3OH^- is 0.03 eV, almost barrierless. The product is 0.57 eV lower in energy than reactants. In a system with BH_3-OH_2 and OH^- coexisting, OH^- is a strong base with negative charge so it tends to obtain a proton from BH_3-OH_2 complex through proton shuffling. Moreover, the left BH_3OH^- is more stable than BH_3-OH_2 complex which agrees with Gardiner and Collat's results[135,138].

Proton shuttling process from BH_3-OH_2 to OH^- is shown in Figure 21. At initial state, OH^- with H colored in yellow is hydrated by two H_2O. Then one H atom in H_2O moiety of BH_3-OH_2 is transfer to neighbor O atoms, which pass on one of its original H atom (colored in

mauve) to next O atom at the same time. Finally the proton transfer terminates at OH^-. The total proton shuffling distance is larger than 8 Å.

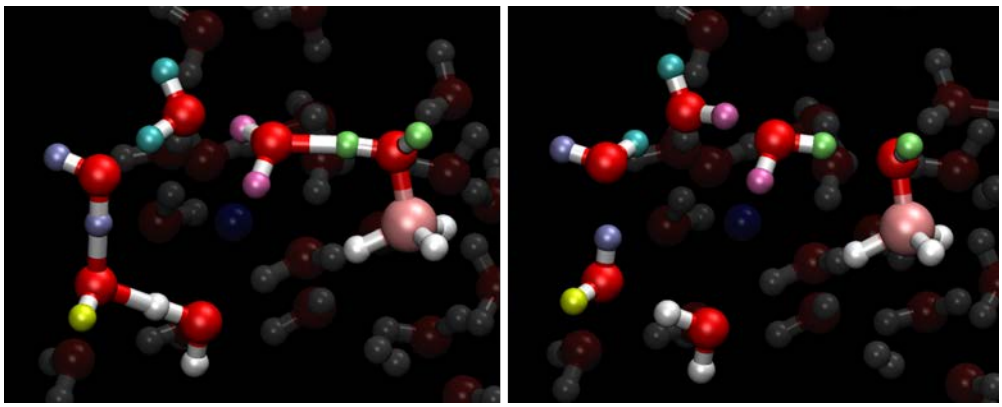

Reactants Products

Figure 21. Structure of reactants and products for BH_3-OH_2 to BH_3OH^-. H atoms in H_2O are colored to show the proton transfer process.

$$BH_3OH^- + H_2O \rightarrow BH_2OH + H_2 + OH^- \quad (3.9)$$

Two possible reaction mechanisms were found for above reaction: (i) BH_3OH^- reacts with H_2O in its first solvation shell; and the corresponding minimum energy pathway and structure evolution are shown in Figure 22 and Figure 23; (ii) water autoionization occurs firstly and then generated H_3O^+ transfers to BH_3OH^- vicinity via proton transfer along water wire, and the corresponding minimum energy pathway and structure evolution are shown in Figure 24, Figure 25 and Figure 26.

For mechanism (i), the distance between BH_3OH^- and its neighbor H_2O molecules gradually become smaller from initial state to transition state. At the transition state, the H_2O molecule dissociates to generate H^+ and at the same time BH_3OH^- also dissociates to generate H^-, which potentially combines with the H^+ to form H_2 molecule. The BH_2OH adopts three-coordinated planar structure and the OH^- generated from H_2O dissociation hydrated by a nearby H_2O to form $H_3O_2^-$. After transition state, the $H_3O_2^-$ and 3 more H_2O with H colored in cyan,

yellow and iceblue construct water wire to promote proton transfer from O with H in cyan to the OH^-. So in the final state OH^- already obtained a proton and changed to H_2O and the newly formed OH^- is hydrated by 1 H_2O on one side and 2 H_2O cluster on the other side. The energy barrier along this pathway is 0.95 eV.

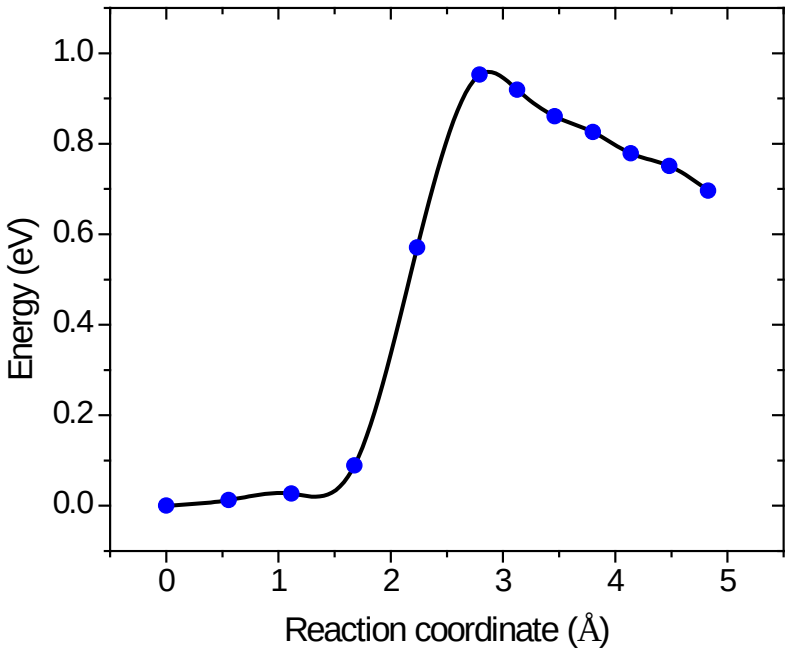

Figure 22. Density functional theory calculation of the minimum energy path for hydrolysis (i) of BH_3OH^- to BH_2OH.

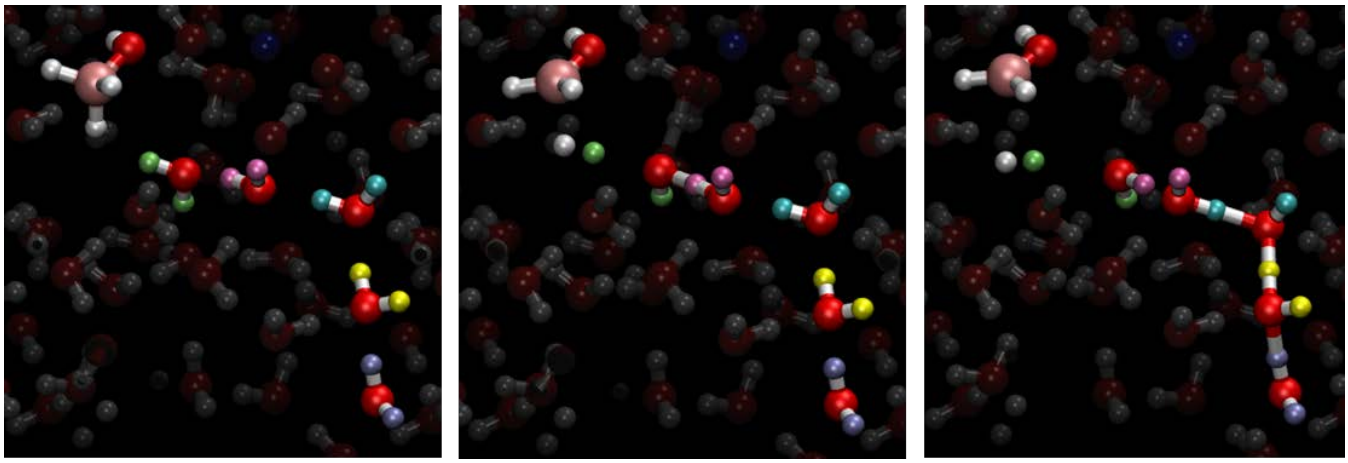

Reactants Transition State Products

Figure 23. Structure of reactants, transition state and products in hydrolysis (i) of BH_3OH^- to BH_2OH. H atoms in H_2O are colored to show the proton transfer process.

Different than (i), the mechanism (ii) is the water autoionization happens firstly, and then the generated H_3O^+ reacts with BH_3OH^-. The reaction barrier of this mechanism is 1.23 eV (Figure 24), which is believed the sum of water autoionization energy[139-142], proton diffusion energy and energy barrier between H_3O^+ and BH_3OH^-. In image 05, prior to the transition state, we observed $H_5O_2^+$, where the extra H^+ is shared by 2 H_2O as shown in Figure 25, indicating H_3O^+ is formed before transition state and the energy increase from image 05 to transition state (about 0.15 eV) is the true energy barrier for the reaction between H_3O^+ and BH_3OH^-. As shown Figure 26, at transition state H_3O^+ with one O-H bond stretched is close to BH_3OH^- with one B-H bond longer than the other two. The two stretched bonds break up after transition state and form a H_2 molecule.

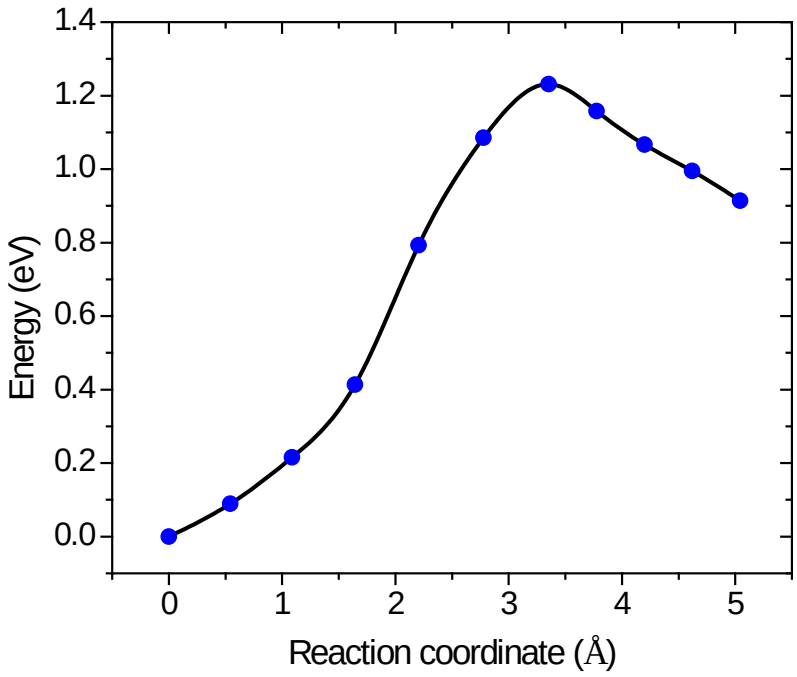

Figure 24. Density functional theory calculation of the minimum energy path for hydrolysis (ii) of BH_3OH^- to BH_2OH.

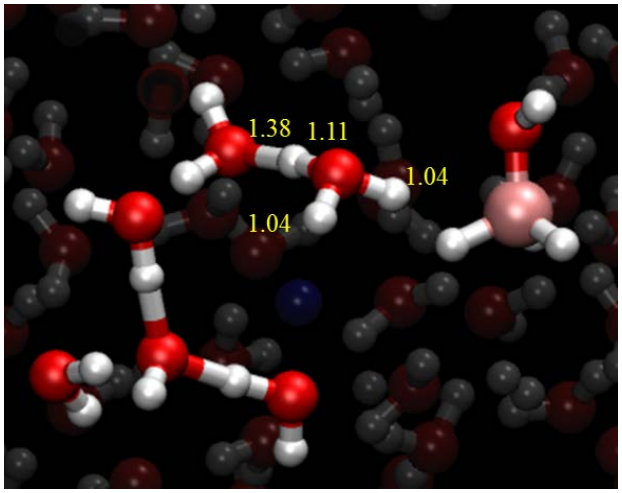

Figure 25. Structure of image 05 (all cNEB calculations start counting from image 00), bond length is in unit of Å

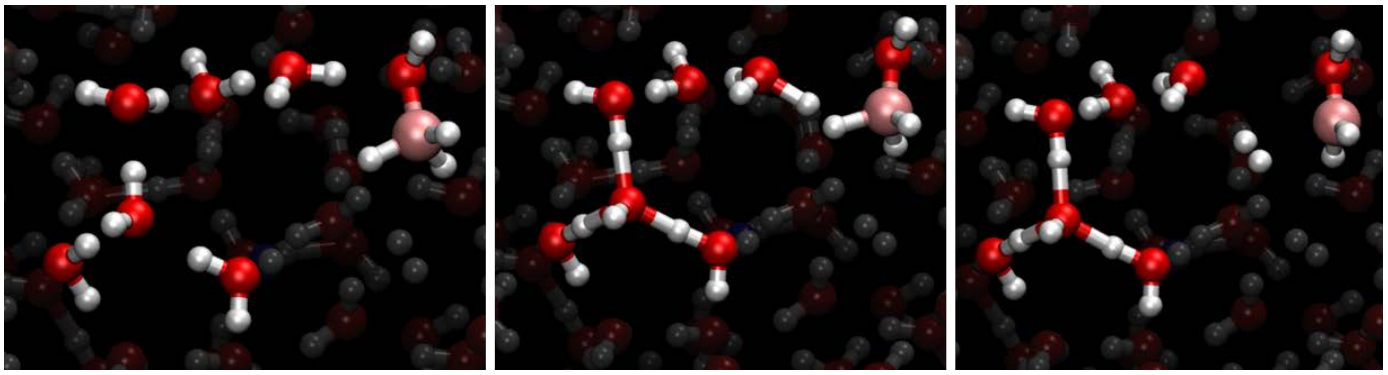

Reactants Transition State Products

Figure 26. Structure of reactants, transition state and products in hydrolysis (ii) of BH_3OH^- to BH_2OH

The two different reaction mechanisms shown above were generated completely independently, and they demonstrate significantly different pathways. One involves water autoionization and proton transfer for H_3O^+ migration; and the other only has proton transfer for OH^- migration. However their reactants and products are the same, indicating that our cNEB calculated barrier is somewhat independent of the choice of reactants and products.

$$BH_2OH + OH^- \rightarrow BH_2(OH)_2^- \qquad (3.10)$$

As product of Equation (3.9), BH_2OH and OH^- coexist in the system but with H_2O molecules in between. OH^- migrates toward BH_2OH via proton transfer and then the two parts combine together to form $BH_2(OH)_2^-$, a stable intermediate after BH_4^- hydrolyzed by 2 H_2O. The energy barrier of this step is 0.46 eV as shown in Figure 27. Figure 28 illustrates the structure evolvement along this reaction. At initial state, OH^- is hydrated by 2 H_2O molecules, while another H_2O is close to BH_2OH. OH^- moves towards the third H_2O at transition state, and is ready to obtain a proton from it. After losing a proton, this H_2O molecule becomes a OH^-, and consequently combines with nearby BH_2OH to form $BH_2(OH)_2^-$.

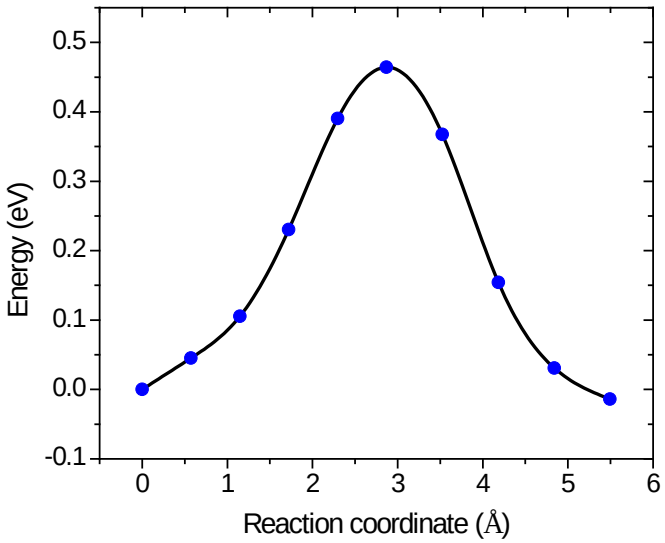

Figure 27. Density functional theory calculation of the minimum energy path for BH_2OH to $BH_2(OH)_2^-$.

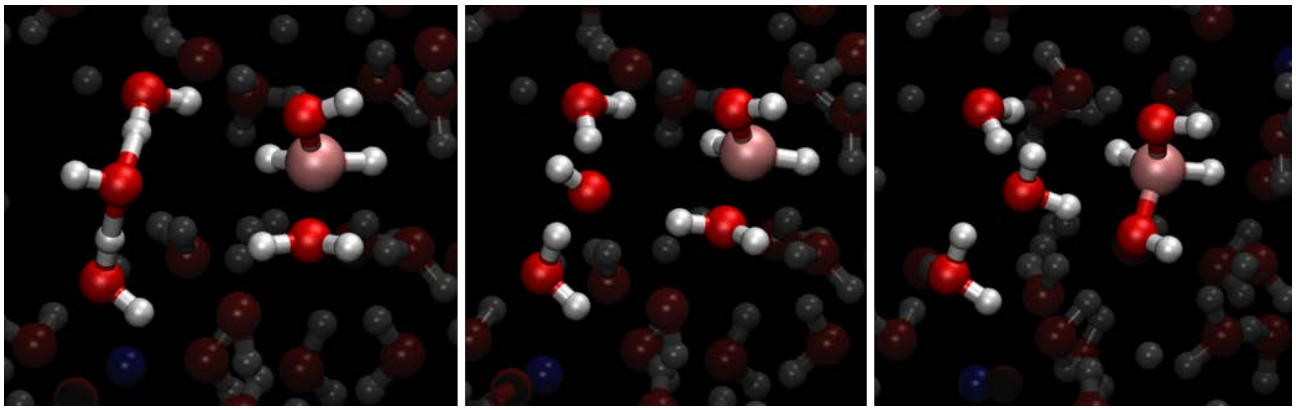

Figure 28. Structure of reactants, transition state and products for BH_2OH to $BH_2(OH)_2^-$

$$BH_2(OH)_2^- + H_2O \rightarrow BH(OH)_2 + H_2 + OH^- \qquad (3.11)$$

Reaction mechanism between $BH_2(OH)_2^-$ and H_2O is similar to mechanism (i) of BH_3OH^- reacting with H_2O, i.e. hydroxyborates $BH_{4-x}(OH)_x^-$ (x=1,2) dissociate to produce H^- when water wire generates H^+, and the left three-coordinate $BH_{3-y}(OH)_y$ (y=1,2) is in planar structure. Both BH_2OH and $BH(OH)_2$ are transient molecules and combine with solvent H_2O to form BH_2OH-OH_2 and $BH(OH)_2$-OH_2 complex quickly after formation. BH_2OH and $BH(OH)_2$ were also

observed in the hydrolysis of diborane by Kawashima et al.[143,144], who measured the lifetime of BH_2OH and $BH(OH)_2$ in a copper waveguide cell at room temperature, and found the former is a few seconds and the latter is half minute. After transition state, OH^- migrates away from three-coordinate $BH_{3-y}(OH)_y$ via proton transfer along the water wire. The energy barrier for $BH_2(OH)_2^-$ hydrolysis to $BH(OH)_2$ is 1.02 eV as shown in Figure 29; and the step is exothermic since the product is 0.45 eV lower than reactants in energy. The structure evolvement for this elementary step is shown in Figure 30.

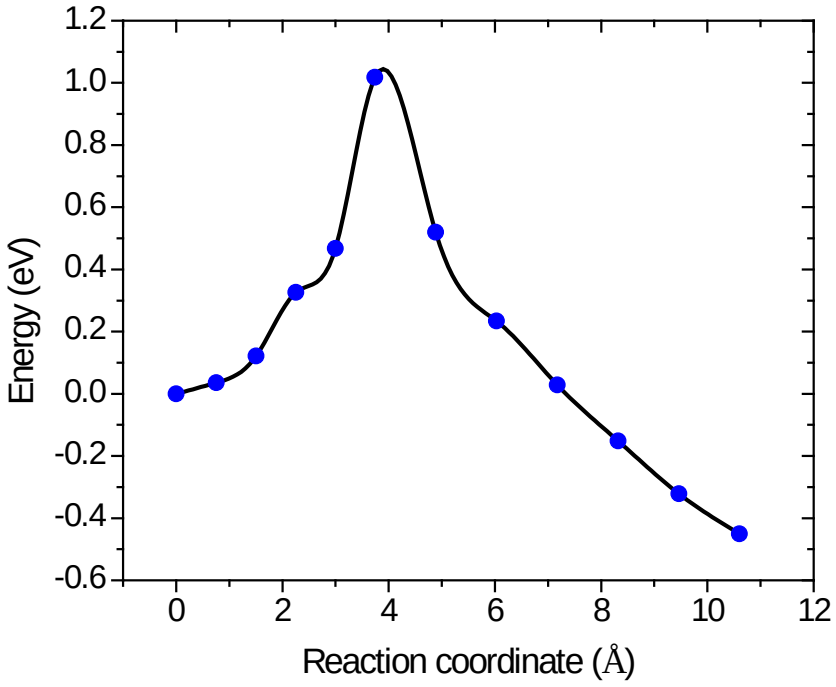

Figure 29. Density functional theory calculation of the minimum energy path for hydrolysis of $BH_2(OH)_2^-$ to $BH(OH)_2$.

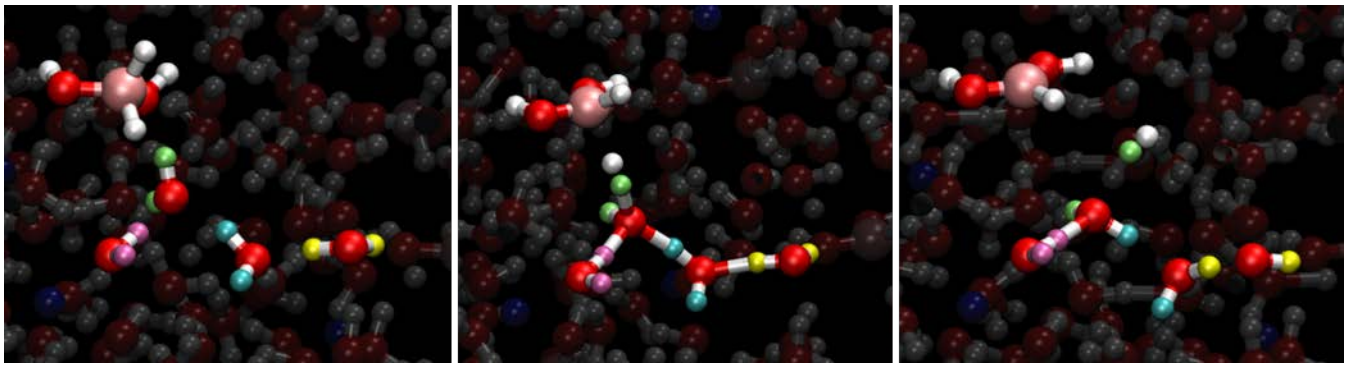

Reactants Transition State Products

Figure 30. Structure of reactants, transition state and products in hydrolysis of $BH_2(OH)_2^-$ to $BH(OH)_2$

$$BH(OH)_3^- + H_2O \rightarrow B(OH)_2O^- + H_2 + H_2O \quad (3.12)$$

Reaction between $BH(OH)_3^-$ and H_2O is similar to BH_3OH^- and $BH_2(OH)_2^-$ hydrolysis mechanism, i.e. at transition state hydroxyborates $BH_{4-x}(OH)_x^-$ (x=1,2,3) dissociate to produce H^- which potentially combine with H^+ generated by H_2O to produce H_2 molecule after transition state. Different from BH_4^- obtaining a proton to form BH_5, $BH_{4-x}(OH)_x^-$ (x=1,2,3) can generate H^- and is transiently stable in three-coordinate planar structure $BH_{3-y}(OH)_y$ (y=1,2,3).

The energy barrier along this pathway is 0.59 eV as shown in Figure 31. At transition state (image 03), $BH(OH)_3^-$ dissociates to H^- and $B(OH)_3$. At image 04, the H^- move close to the H_2O molecule with H colored in lime. And at image 05, the H^- attacks the H_2O and generates H_2 and OH^-. When $B(OH)_3$ and OH^- coexist in a system, $B(OH)_3$ acts as an acid to react with OH^-. The OH^- migrates to $B(OH)_3$ vicinity through proton transfer at image 06. At image 07, $B(OH)_3$ lose a H^+ to OH^- to generate $B(OH)_2O^-$ and H_2O. Therefore, at final state (image 11), the rightmost panel in Figure 32 illustrate the product structure and proton transfer process. Another cNEB calculation for $B(OH)_3 + OH^- \rightarrow B(OH)_2O^- + H_2O$ shows its energy barrier is 0.1 eV and the product is 0.3 eV lower in energy than reactants. This explains that exothermic reaction (8) terminates at $B(OH)_2O^-$ and H_2O because $B(OH)_3 + OH^- \rightarrow B(OH)_2O^- + H_2O$ is almost barrierless.

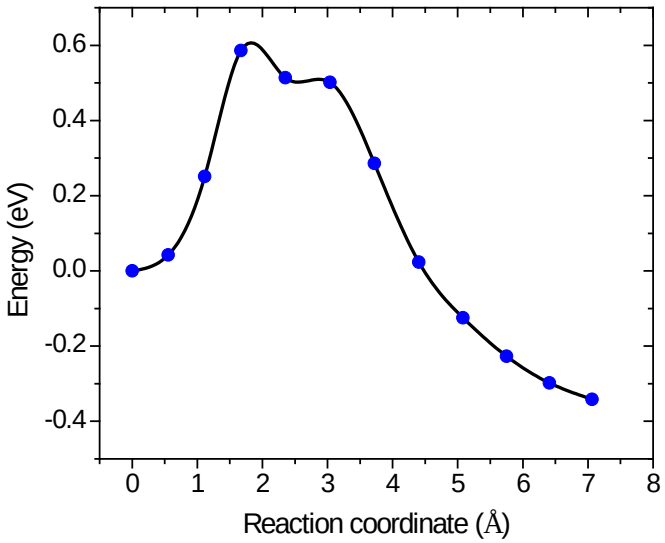

Figure 31. Density functional theory calculation of the minimum energy path for hydrolysis of $BH(OH)_3^-$ to $B(OH)_2O^-$.

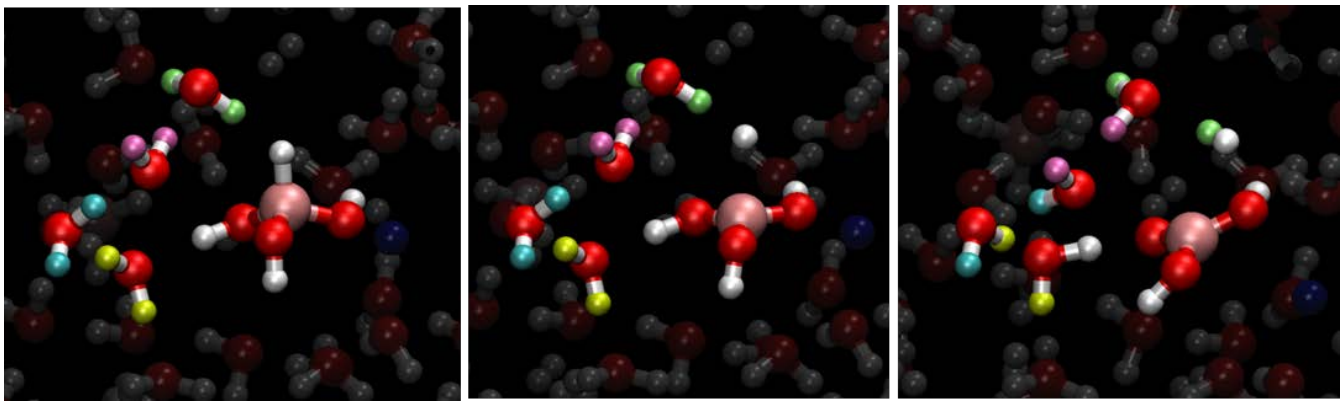

Figure 32. Structure of reactants, transition state (image 03) and products for hydrolysis of $BH(OH)_3^-$ to $B(OH)_2O^-$

3.4.2 Intramolecular reaction

$$BH_3\text{-}OH_2 \rightarrow BH_2OH + H_2 \quad (3.13)$$

Instead of losing a H^+ to generate BH_3OH^-, BH_3-OH_2 can go through intramolecular reconstruction to produce H_2 molecule and three-coordinate BH_2OH in one step instead of two. No matter via one or two steps, BH_3-OH_2 always goes through BH_2OH to other hydroxyborates. Even though the energy barrier of this step is as high as 1.44 eV (see Figure 33), it is comparable to the sum of energy barrier of Equation (3.8) and (3.9). However, the possibility of this reaction in our AIMD calculations is much lower than reaction shown in Equation (3.8) and (3.9). Figure 34 illustrates the structure evolvement in intramolecular reconstruction process. At transition state, one O-H bond rotates to facilitate the H atom shared by O and B atom, and the B, O and H atoms form a triangle structure. After transition state, that H atom and another H atom bonded to B dissociate from B and generate H_2 molecule. BH_2OH is three-coordinate planar structure the same as product in Equation (3.9).

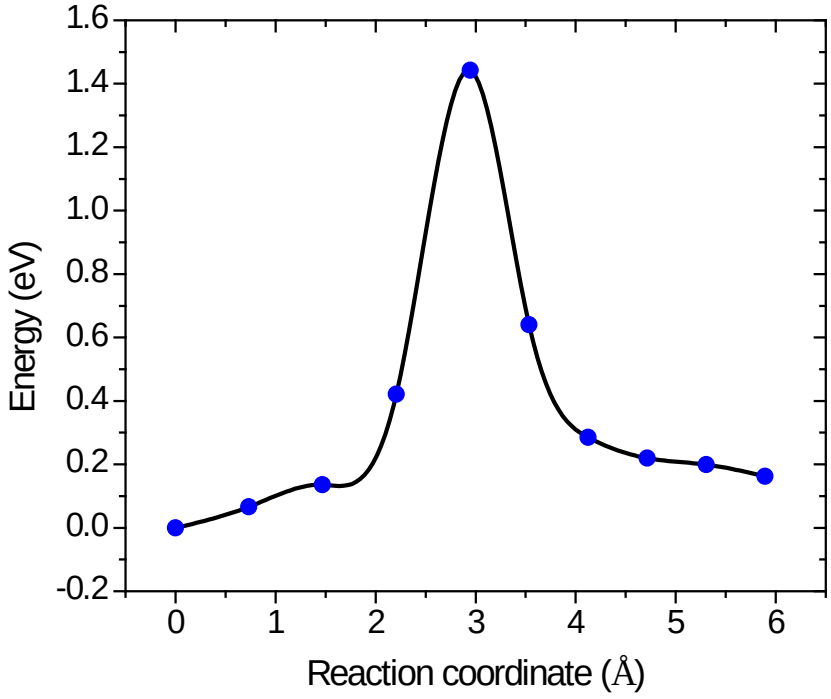

Figure 33. Density functional theory calculation of the minimum energy path for BH_3-OH_2 to BH_2OH.

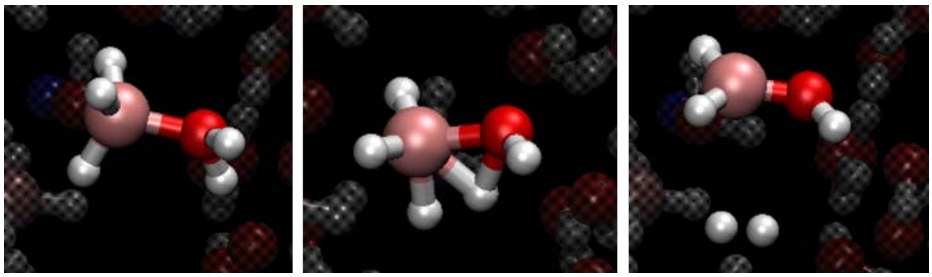

Reactant Transition State Products

Figure 34. Structure of reactants, transition state and products of intramolecular rearrangement of BH_3-OH_2

$$BH_2OH\text{-}OH_2 \rightarrow BH(OH)_2 + H_2 \quad (3.14)$$

Similar intramolecular reconstruction also happens to BH_2OH-OH_2, producing H_2 molecule and three-coordinate $BH(OH)_2$ in one step instead of two. The energy barrier for this step is 1.43 eV (see Figure 35), which is comparable to the sum of energy barrier of Equation (3.10) and (3.11). Figure 36 illustrates the intramolecular reconstruction process, where the O-H

of H_2O moiety forms a triangle structure with B at transition state. After transition state, that H atom and another H bonded to B dissociate from the B atom and generate H_2 molecule.

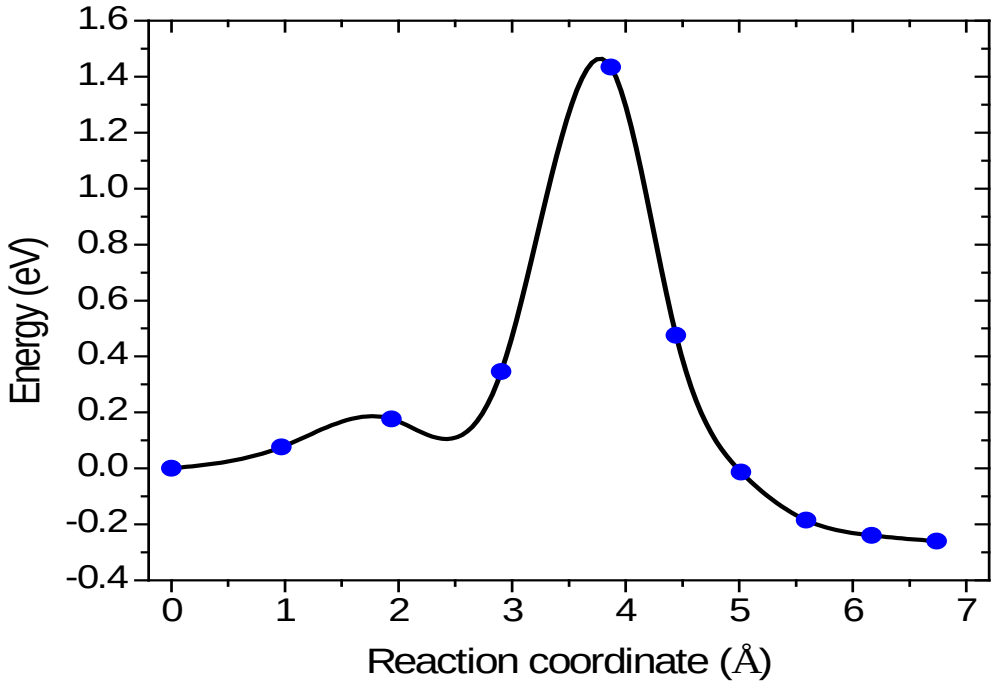

Figure 35. Density functional theory calculation of the minimum energy path for BH_2OH-OH_2 to $BH(OH)_2$

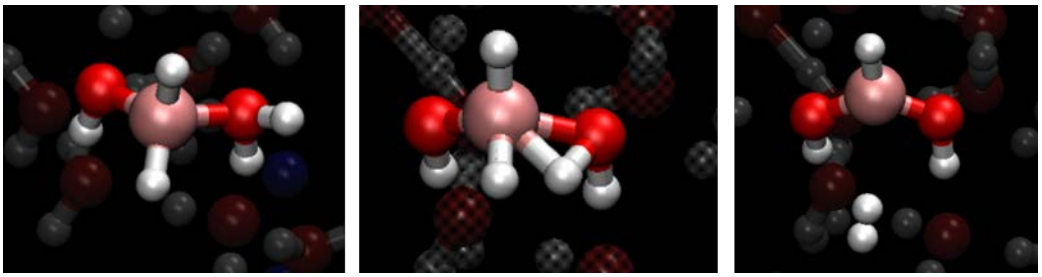

Reactants Transition State Products

Figure 36. Structure of reactants, transition state and products of intramolecular rearrangement of BH_2OH-OH_2.

3.4.3 Reaction between two hydroxyborates

$$BH_3OH_2 + BH_4^- + H_2O \rightarrow BH_3OH^- + BH_3OH_2 + H_2 \quad (3.15)$$

Reaction between hydroxyborates and H_2O are dominant pathways in the overall $NaBH_4$ hydrolysis reaction, only two mechanisms about reaction between two hydroxyborates were observed in our AIMD calculations. In most cases, once a BH_4^- reacts with H_2O, it can hydrolyze to large extent and liberate more than one H_2 while another BH_4^- keeps intact. When BH_3OH_2 and BH_4^- coexist in the system, proton can transfer from H_2O moiety of BH_3OH_2 to BH_4^- via H_2O wire to produce H_2. The energy barrier is 1.30 eV (see Figure 37). As shown in Figure 38, H atoms in 5 H_2O are highlighted with cyan, mauve, yellow, iceblue and lime to show the proton transfer process. At transition state, the H^+ colored in lime attacks BH_4^- and facilitates its dissociation to BH_3 and H^-. After transition state, H+ and H- forms H_2 molecule and BH_3 combines with a nearby H_2O to generate a new BH_3-OH_2 complex.

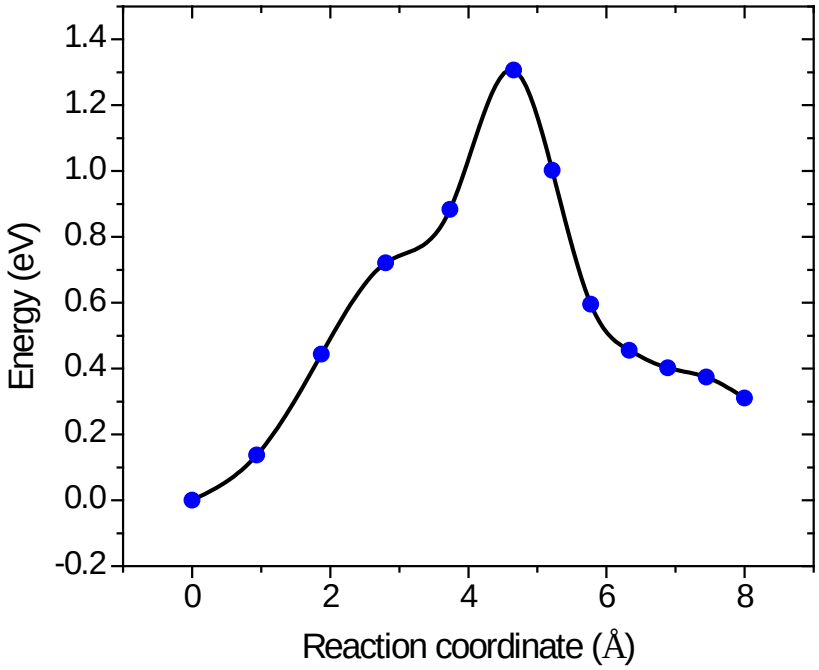

Figure 37. Density functional theory calculation of the minimum energy path for reaction between BH_3OH_2 and BH_4^-.

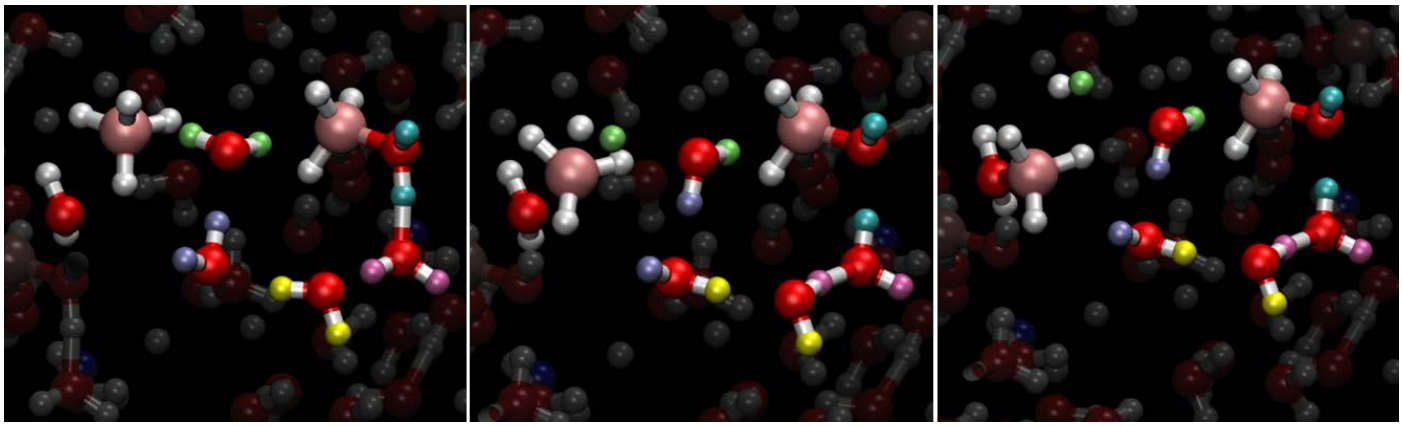

Reactants **Transition State** **Products**

Figure 38. Structure of reactants, transition state and products for reaction between BH_3OH_2 and BH_4^-.

The current work studied the elementary reaction steps of $NaBH_4$ hydrolysis by using cNEB, and revealed the complete picture of the hydrolysis reaction mechanism. Specifically, the reaction of hydroxyborates $BH_{4-x}(OH)_x^-$ (x=1,2,3) and H_2O were identified. Different from BH_4^-

obtaining a proton to form stable BH_5 in C_s symmetry, $BH_{4-x}(OH)_x^-$ (x=1,2,3) can generate H^- and is transiently stable in three-coordinate planar structure $BH_{3-y}(OH)_y$ (y=1,2,3). Furthermore, intramolecular reconstruction of BH_3-OH_2 and BH_2OH-OH_2 to generate H_2 were proposed. The reactions between two hydroxyborates are possible but not favorable in terms of high energy barrier. Proton shuttling and solution rearrangement are essentially involved in the overall $NaBH_4$ hydrolysis reaction. A better understanding of the elementary reaction steps of the hydrolysis reaction may open the pathway for rational catalyst design, reaction optimization, and finally a systematic development of $NaBH_4$ hydrolysis in large-scale H_2 storage.

3.5 RAMAN SPECTRA OF HYDROLYSIS REACTANTS AND PRODUCTS

The materials in this section mainly came from our published paper[145], whereby thermal analyses, X-ray diffraction, and Raman spectroscopy for sodium metaborate hydrates were performed by Dr. Matthews' group to characterize the dehydration mechanism, and I used first-principles density functional theory to compute Raman spectra for $NaBO_2$•$2H_2O$ and $NaBO_2$•$1/3H_2O$ and gave assignment of vibrational modes at molecular level.

Raman spectra of $NaBH_4$ and its hydrolysis products $NaBO_2$•$2H_2O$ and $NaBO_2$•$1/3H_2O$ were calculated using PWSCF code within the Quantum ESPRESSO (QE) software package[77]. The vibrational frequencies and intensities of Raman modes may be determined by the zone-center phonon frequencies and the Raman tensor[146]. Only norm-conserving pseudopotentials with electron exchange and correlation effects described by the LDA[67] can currently be used to calculate Raman spectra within QE, because third-order derivatives of the energy are currently

not implemented in QE with GGA functionals. The cutoff energy was set to 80 Ry, which was found to be sufficiently high to give well-converged structures and total energies. We used 4×5×3 and 4×2×4 Monkhorst-Pack meshes to sample the Brillouin zone of $NaBO_2 \cdot 1/3H_2O$ and $NaBO_2 \cdot 2H_2O$, respectively. This gave a k-point spacing less than 0.05 Å-1. Convergence of the total energy with the number of k-points was examined for the above structures.

We carried out optimization of the unit cells of $NaBO_2 \cdot 1/3H_2O$ and $NaBO_2 \cdot 2H_2O$, with initial structures taken from the Inorganic Crystal Structure Database (ICSD)[147]. Geometry optimizations of the bulk crystal structures were performed by allowing all cell parameters to relax, including atomic positions, cell volume, and shape, until the forces on all atoms were less than 10^{-4} Ry/bohr. We generated norm-conserving LDA pseudopotentials for H, B, O, and Na using the OPIUM pseudopotential code[148], because existing pseudopotentials for these elements in QE were found to be inadequate for our purposes. The transferability of the pseudopotentials was verified by carrying out calculations for the dimers H_2, B_2, O_2, and Na_2, and comparing with results obtained using VASP. We have found excellent agreement between the two sets of results where the deviations for bond lengths, binding energies, and eigen frequencies of the dimers are less than 1%.

Normal mode vibrational frequencies for $NaBO_2 \cdot xH_2O$ (x=1/3, 2) were also calculated within VASP using the LDA and PW91-GGA functionals in order to compare with the vibrational modes computed from PWSCF. The frequencies in VASP were calculated within the harmonic approximation by a finite difference technique. The frequencies computed from PWSCF and VASP with LDA agree to within about 20 wavenumbers, with the results from the VASP calculations giving on average higher frequencies than the PWSCF calculations. The frequencies computed from GGA within VASP are typically within a few tens of wavenumbers

of those computed from LDA, except at high frequencies. For example, the frequencies for $NaBO_2 \cdot 2H_2O$ above about 2800 cm^{-1} differ by a few hundred wavenumbers with the LDA frequencies being red shifted with respect to the GGA frequencies. These highly shifted modes correspond to O-H stretching modes. The frequency of these modes is very sensitive to the hydrogen bonding environment, where hydrogen bonding produces frequencies that are red shifted with respect to free O-H stretching. The reason that the LDA frequencies are red shifted with respect to the GGA frequencies is that the LDA lattice constants, and hence the hydrogen bond lengths, are significantly smaller in the LDA relaxed structures than the corresponding GGA structures (not shown). The hydrogen bonds between the neighboring $B(OH)_4$ groups are as much as 0.2 Å shorter for the LDA relaxed structures, compared with the GGA structures. Given that the GGA structures are in better agreement with the experimental data, we conclude that the GGA frequencies are more accurate for the O-H stretching modes. We do not report experimental results at these high frequencies, so the difference between LDA and GGA in this region is not important to our study.

The experimental (from ICSD) and relaxed (from LDA-DFT) crystal structures of $NaBO_2 \cdot xH_2O$ for x=1/3 and 2 are given in Table 14. The changes in structure during dehydration of $NaBO_2 \cdot 2H_2O$ is illustrated in Figure 39. $NaBO_2 \cdot 1/3H_2O$ is orthorhombic with space group *Pnma* and having four formula units per unit cell. The LDA-DFT calculated cell dimensions are about 3% smaller than the experimental structure, and volume contracts by 8.6%. This is consistent with the general trend that the LDA functional underestimates lattice constants. $NaBO_2 \cdot 2H_2O$ is monoclinic having space group P121/a1 and four formula units per unit cell. LDA-DFT underestimates the lattice parameters by 4% on average compared to experiment, and the volume is smaller by 13.6%.

Table 14. Experimental (from ICSD) and relaxed structure parameters of $NaBO_2 \cdot 1/3H_2O$ and $NaBO_2 \cdot 2H_2O$

		A (Å)	b(Å)	c(Å)	α(degree)	β(degree)	γ(degree)
$NaBO_2 \cdot 1/3H_2O$	Experiment	8.923	7.152	9.548	90	90	90
	Theory (QE)	8.644	6.886	9.353	90	90	90
$NaBO_2 \cdot 2H_2O$	Experiment	5.886	10.566	6.146	90	111.6	90
	Theory (QE)	5.7936	9.7261	5.9467	90	113.69	90

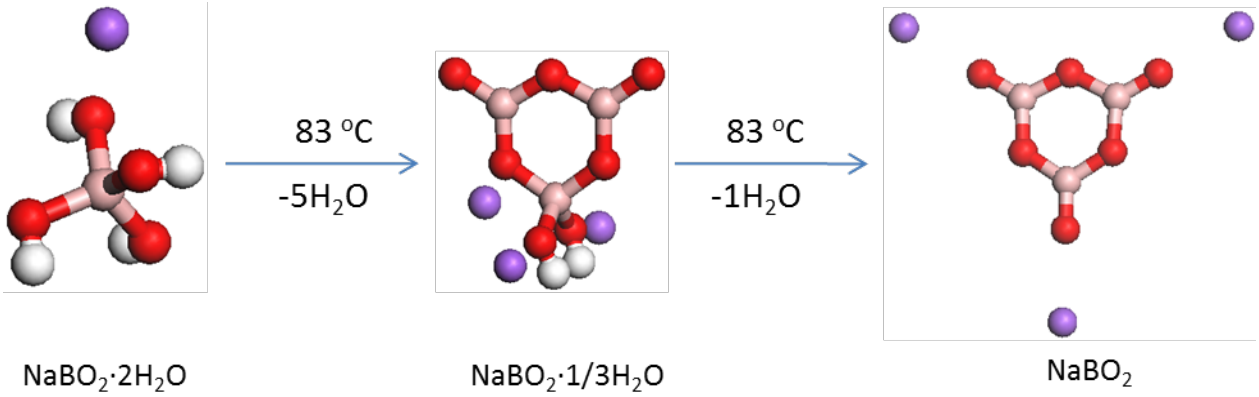

Figure 39. Crystal structure morphology during dehydration of $NaBO_2 \cdot 2H_2O$.

Experimentally observed Raman spectra of $NaBO_2 \cdot xH_2O$ (x=0, 1/3, 2, 4) are listed in Table 15. We also list Raman spectra from the literature for x=0 and 4, and results from our DFT calculations for x=1/3, and 2 for comparison. We have identified the symmetry of the vibrational modes in our computations by inspection of the normal modes. The assignment of the modes is also given in Table 15. The simulated Raman spectra show qualitative consistency with experimental data. There are four Raman active modes associated with deformation of the tetrahedral $B(OH)_4$ group for the $NaBO_2 \cdot 2H_2O$ and $NaBO_2 \cdot 4H_2O$ structures. These modes are illustrated in Figure 40. Nakamoto identified these modes in tetrahedral structures as $\nu_1(A_1)$, $\nu_2(E)$, $\nu_3(F_2)$, and $\nu_4(F_2)$[149]. The specific motions for each of these modes were identified by visualization of the modes as: B-O stretching, H-O-B bending, B-O stretching, and H-B-O

bending, respectively. As shown in Figure 40, the two B-O stretching modes are different: $\nu_1(A_1)$ is symmetric B-O stretching, $\nu_3(F_2)$ is asymmetric B-O stretching. The two H-O-B bending are also distinct. The difference between the $B(OH)_4$ groups in the $NaBO_2 \cdot 2H_2O$ and $NaBO_2 \cdot 4H_2O$ structures is that in the latter case the $B(OH)_4$ groups are surrounded by H_2O molecules. Jun et al.[150] assigned the 1069 cm^{-1} and 952 cm^{-1} modes of $NaBO_2 \cdot 4H_2O$ as asymmetric stretching of B-O. One would assume that nearly the same frequencies in $NaBO_2 \cdot 2H_2O$ would be the same modes; we have therefore tentatively assigned our experimentally observed modes at 1072 and 952 cm^{-1} in the x=2 material as B-O asymmetric stretching modes. Our calculations for $NaBO_2 \cdot 2H_2O$ have Raman modes at 1024 and 924 cm^{-1} that we believe correspond to the experimental 1072 and 952 cm^{-1} modes. However, the simulated modes are clearly H-O-B and H-B-O bending, respectively, and not B-O asymmetric stretching modes. Hence, there are two possibilities: the symmetry of the modes in the x=4 structure are not the same as the x=2 structure or, more likely, the modes identified by Jun et al.[150] as asymmetric stretching were misassigned and are in fact H-O-B and H-B-O bending modes. The other modes from our calculations agree with the experimentally assigned modes from Jun et al[150].

Table 15. Comparison of observed Raman bands (cm^{-1}) with literature assignments and computations [145]

Mode Description	$NaBO_2•4H_2O$		$NaBO_2•2H_2O$		$NaBO_2•⅓H_2O$		$NaBO_2$	
	Expt.	Ref.[150]	Expt.	Theory (QE)	Expt.	Theory (QE)	Expt.	Ref.[151]
in-plane $B_{(3)}$-O^- stretching						1486	1571 1547	1575 1554
asymmetric stretching of $B_{(3)}$-O							1078	
asymmetric stretching of $B_{(4)}$-O	1072 998 948	1069 952	1072 952	1024 [ν_2(E)] 924 [$\nu_4(F_2)$]	1079	970		
symmetric stretching of $B_{(3)}$-O					908	897		
symmetric stretching of $B_{(4)}$-O	 769	 857 768			847	877		
ring breathing					757	742	755	770
symmetric stretching of $B_{(4)}$-O[152]	739		740	733 [$\nu_1(A_1)$]				
out-of-plane bending of $B_{(3)}$-O							683	682
ring breathing					636	660	628	627
bending and deformation of $B_{(4)}$-O	579	579	579 527 510	633 [ν_2(E)] 543 [$\nu_3(F_2)$] 501 [ν_2(E)]	543	554		
bending of $B_{(3)}$-O					476	478	476	475
bending of $B_{(4)}$-O	466 408	467 391	466 410		420	441		
bending of $B_{(3)}$-O							402	399
bending of $B_{(4)}$-O	348		343		359	365		

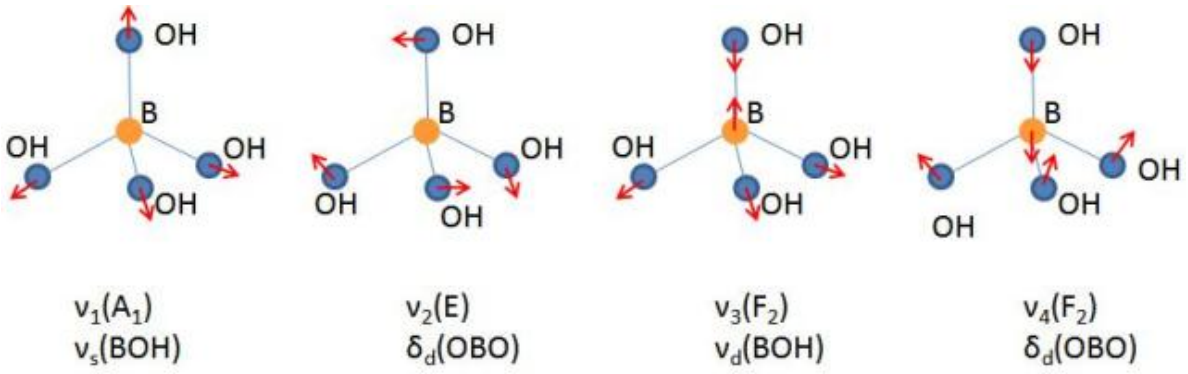

Figure 40. Raman active modes associated with the tetrahedral $B(OH)_4^-$ group [149].

Upon heating, $NaBO_2 \cdot 2H_2O$ is dehydrated to $NaBO_2 \cdot 1/3H_2O$, which has a planar ring structure with six intra-annular B-O bands, where two OH groups attached with one boron atom and one oxygen with the each of the other two boron atoms. The Raman spectra of $NaBO_2 \cdot 1/3H_2O$, $B(OH)_2$ exhibits out-of-ring asymmetric HO-B-OH stretching, which does not exist in $NaBO_2 \cdot 2H_2O$. Ring vibrational modes are manifest in both $NaBO_2 \cdot 1/3H_2O$ and $NaBO_2$[151,153]. We have assigned identities for the $NaBO_2 \cdot 1/3H_2O$ phase by comparison with both our DFT calculated spectra and the experimentally reported x=0 spectra. Our calculated Raman modes for x=1/3 are in generally good agreement with the experimental frequencies. We note, however, that the calculated spectra indicate the presence of modes at 1486 and 1457 cm^{-1} that are not distinguished in the experimentally measured spectra. These correspond to in-plane $B_{(3)}$-O stretching modes that are observed experimentally in the $NaBO_2$ compound. The reason these modes are not resolved in the experiments is that they overlap with the sample holder region. As shown in Figure 41 measure by our collaborator Dr. Matthews' group, where peaks around 1450 cm^{-1} can be seen, but cannot be unambiguously resolved from the sample holder. The mode assignments we deduce from our DFT calculations agree with the mode assignments inferred by comparison with the previously published data for $NaBO_2$[151].

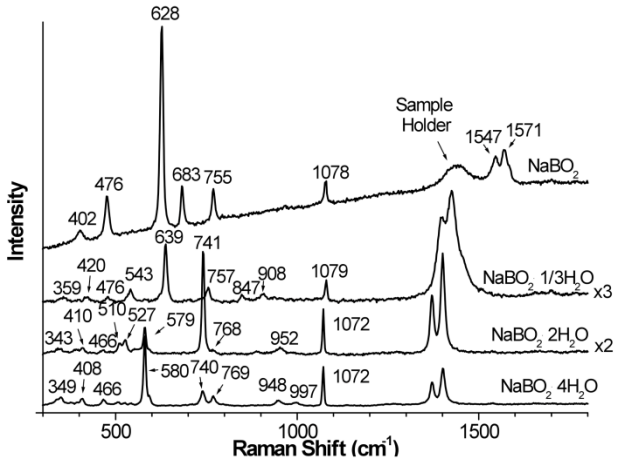

Figure 41. Raman spectra of hydrated sodium metaborates (x=4, 2, ⅓, 0)

In summary, we have computed Raman spectra for $NaBO_2 \cdot 2H_2O$ and $NaBO_2 \cdot 1/3H_2O$ from DFT and have found good agreement with experimental spectra. The symmetry of the modes identified from simulations for $NaBO_2 \cdot 2H_2O$ is in agreement with previous experiments for $NaBO_2 \cdot 4H_2O$ except for the modes at 1072 and 952 cm^{-1}. We predict that these modes are H-O-B and H-B-O bending, respectively, rather than B-O stretching.

4.0 SUMMARY AND FUTURE WORK

Our DFT optimized α-$NaBH_4$ is in $Fm\bar{3}m$ space group with lattice constant a = 6.0509 Å, $d_{B\text{-}H}$ = 1.22 Å. It is found that (100) surface is the lowest energy surface, which could dominate the experimentally observed surfaces, and are candidates for water adsorption and hydrolysis reaction.

Water adsorption on $NaBH_4$ (100) surface was studied by first principles DFT calculations with inclusion of dispersion correction as DFT-D2 implemented in VASP to investigate the interaction between water and $NaBH_4$ (100) surface as an initial step in understanding how deliquescence takes place. It is a first step toward understanding how the whole deliquescence process of $NaBH_4$ occurs, which is difficult to characterize in experiment due to the hygroscopic nature of $NaBH_4$. The H_2O monomer is favorably adsorbed above the sodium site through O···Na and O-H···H-B attractions with hydrogen atoms, resulting in water adsorbing such that the plane of water is tilted with H atoms down. The O-H···H-B attraction is consistent with the dihydrogen bond found in the $NaBH_4 \cdot 2H_2O$ crystal and in aqueous $NaBH_4$. The adsorption energy per water molecule is independent of water coverage, suggesting that an infinitely thick water film could form on the surface. Adsorbed H_2O molecules facilitate $NaBH_4$(100) surface reconstruction through 90° rotation of BH_4^- groups in the surface. This process increases the roughness of the surface and promotes dissolution of $NaBH_4$ into the

adsorbed water. Hence, H_2O-promoted surface reconstruction may be considered a preliminary step in the deliquescence process.

In the initial stage of deliquescence, the first step is roughening of the $NaBH_4$ surface. The $NaBH_4$ surface is no longer flat after several layers of water molecules are adsorbed on top, due to the interaction between water and $NaBH_4$. The second step is for one or more BH_4^- ions to leave the surface and diffuse into the water phase. This leaves vacancies for H_2O molecules to penetrate into the $NaBH_4$ solid. Hence, the third step is for H_2O molecules to diffuse into BH_4^- vacancies and then penetrate down to deeper layers of $NaBH_4$. Then fourth step is for Na^+ ions to diffuse into water phase to form a charge neutral $NaBH_4$ solution. Finally, a new section forms at the interface of water and solid $NaBH_4$ phase.

We studied the elementary reaction steps of $NaBH_4$ hydrolysis by using cNEB, and revealed the complete picture of the hydrolysis reaction mechanism. Specifically, the reaction of hydroxyborates $BH_{4-x}(OH)_x^-$ (x=1,2,3) and H_2O were identified. Different from BH_4^- obtaining a proton to form stable BH_5 in C_s symmetry, $BH_{4-x}(OH)_x^-$ (x=1,2,3) can generate H^- and is transiently stable in three-coordinate planar structure $BH_{3-y}(OH)_y$ (y=1,2,3). Furthermore, intramolecular reconstruction of BH_3-OH_2 and BH_2OH-OH_2 to generate H_2 were proposed. The reactions between two hydroxyborates are possible but not favorable in terms of high energy barrier. Proton shuttling and solution rearrangement are essentially involved in the overall $NaBH_4$ hydrolysis reaction. A better understanding of the elementary reaction steps of the hydrolysis reaction may open the pathway for rational catalyst design, reaction optimization, and finally a systematic development of $NaBH_4$ hydrolysis in large-scale H_2 storage.

Raman spectra and mode assignment for hydrolysis reaction byproducts $NaBO_2 \cdot 2H_2O$ and $NaBO_2 \cdot 1/3H_2O$ have been calculated from DFT and are in good agreement with

experimental spectra. The symmetry of the modes identified from simulations for $NaBO_2 \cdot 2H_2O$ is in agreement with previous experiments for $NaBO_2 \cdot 4H_2O$ except for the modes at 1072 and 952 cm^{-1}. We predict that these modes are H-O-B and H-B-O bending, respectively, rather than B-O stretching.

In future work, to quantitatively understand the deliquescence process and predict experiment deliquescence condition, Gibbs free energy change of Na^+/BH_4^- moving from crystal lattice to bulk liquid water will be computed with our developed MSXX FF by using molecular dynamics simulation. Potential mean force calculations for Na^+ and BH_4^- moving along surface normal direction will be performed using the umbrella sampling method[154]. A harmonic biasing potential along the surface normal direction will be applied to Na^+ and BH_4^-. Testing works for the FF (including $NaBH_4$ lattice constant, density and compressibility, $NaBH_4 \cdot 2H_2O$ density) have shown good agreement with experiments and our *ab initio* calculation results. Additional testing calculations will ensure the FF is reliable for our system.

BIBLIOGRAPHY

(1) Dillon, A. C.; Jones, K. M.; Bekkedahl, T. A.; Kiang, C. H.; Bethune, D. S.; Heben, M. J. *Nature* **1997**, *386*, 377.

(2) Rosi, N. L.; Eckert, J.; Eddaoudi, M.; Vodak, D. T.; Kim, J.; O'Keeffe, M.; Yaghi, O. M. *Science* **2003**, *300*, 1127.

(3) Nijkamp, M. G.; Raaymakers, J. E. M. J.; Van Dillen, A. J.; De Jong, K. P. *Appl. Phys. A* **2001**, *72*, 619.

(4) Morris, R. E.; Wheatley, P. S. *Angew. Chem. Int. Ed.* **2008**, *47*, 4966.

(5) Jena, P. *J. Phys. Chem. Lett.* **2011**, *2*, 206.

(6) Schlapbach, L.; Züttel, A. *Nature* **2001**, *414*, 353.

(7) Züttel, A. *Naturwiss.* **2004**, *91*, 157.

(8) Chen, P.; Xiong, Z.; Luo, J.; Lin, J.; Lee Tan, K. *Nature* **2002**, *420*, 302.

(9) Gutowska, A.; Li, L.; Shin, Y.; Wang, C. M.; Li, X. S.; Linehan, J. C.; Smith, R. S.; Kay, B. D.; Schmid, B.; Shaw, W.; Gutowski, M.; Autrey, T. *Angew. Chem. Int. Ed.* **2005**, *44*, 3578.

(10) Schlesinger, H. I.; Brown, H. C.; Finholt, A. E.; Gilbreath, J. R.; Hoekstra, H. R.; Hyde, E. K. *J. Am. Chem. Soc.* **1953**, *75*, 215.

(11) Sun, D.; Kiyobayashi, T.; Takeshita, H. T.; Kuriyama, N.; Jensen, C. M. *J. Alloys Compd.* **2002**, *337*, L8.

(12) Orimo, S.; Nakamori, Y.; Züttel, A. *Mater. Sci. Eng., B* **2004**, *108*, 51.

(13) Renaudin, G.; Gomes, S.; Hagemann, H.; Keller, L.; Yvon, K. *J. Alloys Compd.* **2004**, *375*, 98.

(14) Varin, R. A.; Chiu, C. *J. Alloys Compd.* **2005**, *397*, 276.

(15) Kumar, R. S.; Cornelius, A. L. *Appl. Phys. Lett.* **2005**, *87*, 1.

(16) Sundqvist, B.; Andersson, O. *Phys. Rev. B: Condens. Matter* **2006**, *73*, 092102.

(17) Blomqvist, H.; Rönnebro, E.; Kyoi, D.; Sakai, T.; Noréus, D. *J. Alloys Compd.* **2003**, *358*, 82.

(18) Lodziana, Z.; Vegge, T. *Phys. Rev. Lett.* **2004**, *93*, 145501.

(19) Ravindran, P.; Vajeeston, P.; Fjellvåg, H.; Kjekshus, A. *Comput. Mater. Sci.* **2004**, *30*, 349.

(20) Vajeeston, P.; Ravindran, P.; Kjekshus, A.; Fjellvåg, H. *J. Alloys Compd.* **2005**, *387*, 97.

(21) Vajeeston, P.; Ravindran, P.; Vidya, R.; Fjellvåg, H.; Kjekshus, A. *Appl. Phys. Lett.* **2003**, *82*, 2257.

(22) Kim, K. C.; Sholl, D. S. *J. Phys. Chem. C* **2010**, *114*, 678.

(23) Lee, G.; Lee, J. Y.; Kim, J. S. *Solid State Commun.* **2006**, *139*, 516.

(24) Araújo, C. M.; Ahuja, R.; Talyzin, A. V.; Sundqvist, B. *Phys. Rev. B: Condens. Matter* **2005**, *72*, 054125.

(25) Babanova, O. A.; Soloninin, A. V.; Stepanov, A. P.; Skripov, A. V.; Filinchuk, Y. *J. Phys. Chem. C* **2010**, *114*, 3712.

(26) Filinchuk, Y.; Talyzin, A. V.; Chernyshov, D.; Dmitriev, V. *Phys. Rev. B: Condens. Matter* **2007**, *76*, 092104.

(27) Stockmayer, W. H.; Rice, D. W.; Stephenson, C. C. *J. Am. Chem. Soc.* **1955**, *77*, 1980.

(28) Custelcean, R.; Jackson, J. E. *Chem. Rev.* **2001**, *101*, 1963.

(29) Filinchuk, Y.; Hagemann, H. *Eur. J. Inorg. Chem.* **2008**, 3127.

(30) Murtomaa, M.; Laine, E.; Salonen, J.; Kuusinen, O. *Powder Handling and Processing* **1999**, *11*, 87.

(31) Beaird, A. M.; Davis, T. A.; Matthews, M. A. *Ind. Eng. Chem. Res.* **2010**, *49*, 9596.

(32) Aiello, R.; Sharp, J. H.; Matthews, M. A. *Int. J. Hydrogen Energy* **1999**, *24*, 1123.

(33) Marrero-Alfonso, E. Y.; Gray, J. R.; Davis, T. A.; Matthews, M. A. *Int. J. Hydrogen Energy* **2007**, *32*, 4717.

(34) Marrero-Alfonso, E. Y.; Gray, J. R.; Davis, T. A.; Matthews, M. A. *Int. J. Hydrogen Energy* **2007**, *32*, 4723.

(35) Fakioğlu, E.; Yürüm, Y.; Veziroğlu, T. N. *Int. J. Hydrogen Energy* **2004**, *29*, 1371.

(36) Diakov, V.; Diwan, M.; Shafirovich, E.; Varma, A. *Chem. Eng. Sci.* **2007**, *62*, 5586.

(37) Shafirovich, E.; Diakov, V.; Varma, A. *Int. J. Hydrogen Energy* **2007**, *32*, 207.

(38) Marrero-Alfonso, E. Y.; Beaird, A. M.; Davis, T. A.; Matthews, M. A. *Ind. Eng. Chem. Res.* **2009**, *48*, 3703.

(39) James, B. D.; Wallbridge, M. G. H. *Prog. Inorg. Chem.* **1970**, *11*, 99.

(40) Kojima, Y.; Suzuki, K. I.; Fukumoto, K.; Sasaki, M.; Yamamoto, T.; Kawai, Y.; Hayashi, H. *Int. J. Hydrogen Energy* **2002**, *27*, 1029.

(41) Damjanović, L.; Bennici, S.; Auroux, A. *J. Power Sources* **2010**, *195*, 3284.

(42) Zhang, J.; Fisher, T. S.; Gore, J. P.; Hazra, D.; Ramachandran, P. V. *Int. J. Hydrogen Energy* **2006**, *31*, 2292.

(43) Demirci, U. B.; Garin, F. *Catal. Commun.* **2008**, *9*, 1167.

(44) Kojima, Y.; Kawai, Y.; Nakanishi, H.; Matsumoto, S. *J. Power Sources* **2004**, *135*, 36.

(45) Zhang, Q.; Wu, Y.; Sun, X.; Ortega, J. *Ind. Eng. Chem. Res.* **2007**, *46*, 1120.

(46) Patel, N.; Fernandes, R.; Miotello, A. *J. Power Sources* **2009**, *188*, 411.

(47) Chamoun, R.; Demirci, U. B.; Zaatar, Y.; Khoury, A.; Miele, P. *Int. J. Hydrogen Energy* **2010**, *35*, 6583.

(48) Andrieux, J.; Demirci, U. B.; Hannauer, J.; Gervais, C.; Goutaudier, C.; Miele, P. *Int. J. Hydrogen Energy* **2011**, *36*, 224.

(49) Li, F.; Li, Q.; Kim, H. *Chemical Engineering Journal* **2012**, *210*, 316.

(50) Oh, T. H.; Kwon, S. *Int. J. Hydrogen Energy* **2012**, *37*, 15925.

(51) Peng, S. G.; Liu, C. Y.; Liu, X. F.; Zhang, J.; Zhang, Y. Q. *Integr. Ferroelectr.* **2012**, *135*, 47.

(52) Demirci, U. B.; Garin, F. *J. Mol. Catal. A-Chem.* **2008**, *279*, 57.

(53) Liang, Y.; Wang, P.; Dai, H. B. *J. Alloys Compd.* **2010**, *491*, 359.

(54) Goubeau, J.; Kallfass, H. *Z. Anorg. Allg. Chem.* **1959**, *299*, 160.

(55) Mikheeva, V. I.; Fedneva, E. M. *Dokl. Akad. Nauk. SSSR* **1955**, *101*, 99.

(56) Mikheeva, V. I.; Surs, V. Y. *Dokl. Akad. Nauk. SSSR* **1953**, *93*, 67.

(57) Mikheeva, V. I.; Surs, V. Y. *Dokl. Akad. Nauk. SSSR* **1953**, *91*, 1133.

(58) Mochalov, K. N.; Khain, V. S.; Gilmansh.Gg *Dokl. Akad. Nauk. SSSR* **1965**, *162*, 613.

(59) Mochalov, K. N.; Khain, V. S.; Gil'manshin, G. G. *Kinet. Katal.* **1965**, *6*, 541.

(60) Mesmer, R. E.; Jolly, W. L. *Inorg. Chem.* **1962**, *1*, 608.

(61) Davis, R. E.; Bromels, E.; Kibby, C. L. *J. Am. Chem. Soc.* **1962**, *84*, 885.

(62) Kilpatrick, M.; McKinney, C. D. *J. Am. Chem. Soc.* **1950**, *72*, 5474.

(63) Stockmayer, W.; Zeto, R. J.; Miller, R. R. *J. Phys. Chem.* **1961**, *65*, 1076.

(64) Hohenberg, P.; Kohn, W. *Phys. Rev.* **1964**, *136*.

(65) Kohn, W.; Sham, L. J. *Phys. Rev.* **1965**, *140*.

(66) Levy, M. *Proc. Natl. Acad. Sci. U.S.A.* **1979**, *76*, 6062.

(67) Perdew, J. P.; Zunger, A. *Phys. Rev. B: Condens. Matter* **1981**, *23*, 5048.

(68) Tschinke, V.; Ziegler, T. *Can. J. Chem.-Rev. Can. Chim.* **1989**, *67*, 460.

(69) Neumann, R.; Handy, N. C. *Chem. Phys. Lett.* **1997**, *266*, 16.

(70) Perdew, J. P.; Kurth, S.; Zupan, A.; Blaha, P. *Phys. Rev. Lett.* **1999**, *82*, 2544.

(71) Becke, A. D. *J. Chem. Phys.* **1993**, *98*, 1372.

(72) Kresse, G.; Furthmüller, J. *Comput. Mater. Sci.* **1996**, *6*, 15.

(73) Kresse, G.; Hafner, J. *Phys. Rev. B: Condens. Matter* **1993**, *47*, 558.

(74) Kresse, G.; Hafner, J. *Phys. Rev. B: Condens. Matter* **1994**, *49*, 14251.

(75) Blöchl, P. E. *Phys. Rev. B: Condens. Matter* **1994**, *50*, 17953.

(76) Kresse, G.; Joubert, D. *Phys. Rev. B: Condens. Matter* **1999**, *59*, 1758.

(77) Giannozzi, P.; Baroni, S.; Bonini, N.; Calandra, M.; Car, R.; Cavazzoni, C.; Ceresoli, D.; Chiarotti, G. L.; Cococcioni, M.; Dabo, I.; Dal Corso, A.; De Gironcoli, S.; Fabris, S.; Fratesi, G.; Gebauer, R.; Gerstmann, U.; Gougoussis, C.; Kokalj, A.; Lazzeri, M.; Martin-Samos, L.; Marzari, N.; Mauri, F.; Mazzarello, R.; Paolini, S.; Pasquarello, A.; Paulatto, L.; Sbraccia, C.; Scandolo, S.; Sclauzero, G.; Seitsonen, A. P.; Smogunov, A.; Umari, P.; Wentzcovitch, R. M. *J. Phys.: Condens. Matter.* **2009**, *21*, 395502.

(78) Plimpton, S. *J. Comput. Phys.* **1995**, *117*, 1.

(79) Mayo, S. L.; Olafson, B. D.; Goddard Iii, W. A. *J. Phys. Chem.* **1990**, *94*, 8897.

(80) Perdew, J. P.; Chevary, J. A.; Vosko, S. H.; Jackson, K. A.; Pederson, M. R.; Singh, D. J.; Fiolhais, C. *Phys. Rev. B: Condens. Matter* **1992**, *46*, 6671.

(81) Perdew, J. P.; Chevary, J. A.; Vosko, S. H.; Jackson, K. A.; Pederson, M. R.; Singh, D. J.; Fiolhais, C. *Phys. Rev. B: Condens. Matter* **1993**, *48*, 4978.

(82) Kim, E.; Kumar, R.; Weck, P. F.; Cornelius, A. L.; Nicol, M.; Vogel, S. C.; Zhang, J.; Hartl, M.; Stowe, A. C.; Daemen, L.; Zhao, Y. *J. Phys. Chem. B* **2007**, *111*, 13873.

(83) Chernyshov, D.; Bosak, A.; Dmitriev, V.; Filinchuk, Y.; Hagemann, H. *Phys. Rev. B: Condens. Matter* **2008**, *78*, 172104.

(84) Tang, W.; Sanville, E.; Henkelman, G. *J. Phys.: Condens. Matter*. **2009**, *21*.

(85) Sanville, E.; Kenny, S. D.; Smith, R.; Henkelman, G. *J. Comput. Chem.* **2007**, *28*, 899.

(86) Henkelman, G.; Arnaldsson, A.; Jónsson, H. *Comput. Mater. Sci.* **2006**, *36*, 354.

(87) Dai, B.; Rankin, R. B.; Johnson, J. K.; Allendorf, M. D.; Sholl, D. S.; Zarkevich, N. A.; Johnson, D. D. *J. Phys. Chem. C* **2008**, *112*, 18270.

(88) Kim, K. C.; Sholl, D. S. *J. Phys. Chem. C* **2010**, *114*, 678.

(89) Grimme, S. *J. Comput. Chem.* **2006**, *27*, 1787.

(90) Tkatchenko, A.; Scheffler, M. *Phys. Rev. Lett.* **2009**, *102*, 073005.

(91) Dion, M.; Rydberg, H.; Schröder, E.; Langreth, D. C.; Lundqvist, B. I. *Phys. Rev. Lett.* **2004**, *92*, 246401.

(92) Klimeš, J.; Bowler, D. R.; Michaelides, A. *J. Phys.: Condens. Matter*. **2010**, *22*, 022201.

(93) Lee, K.; Murray, É. D.; Kong, L.; Lundqvist, B. I.; Langreth, D. C. *Phys. Rev. B: Condens. Matter* **2010**, *82*, 081101.

(94) Al-Saidi, W. A.; Voora, V. K.; Jordan, K. D. *J. Chem. Theory Comput.* **2012**, *8*, 1503.

(95) Voora, V. K.; Al-Saidi, W. A.; Jordan, K. D. *J. Phys. Chem. A* **2011**, *115*, 9695.

(96) Hamada, I.; Yamauchi, K.; Oguchi, T. *Phys. Rev. B: Condens. Matter* **2012**, *85*, 214119.

(97) Frayret, C.; Izgorodina, E. I.; MacFarlane, D. R.; Villesuzanne, A.; Barrès, A. L.; Politano, O.; Rebeix, D.; Poizot, P. *Phys. Chem. Chem. Phys.* **2012**, *14*, 11398.

(98) Hasegawa, M.; Nishidate, K.; Iyetomi, H. *Phys. Rev. B: Condens. Matter* **2007**, *76*, 115424.

(99) Jahn, S.; Madden, P. A.; Wilson, M. *Phys. Rev. B: Condens. Matter* **2006**, *74*, 024112.

(100) Wales, D. J.; Doye, J. P. K. *J. Phys. Chem. A* **1997**, *101*, 5111.

(101) Yang, Y.; Meng, S.; Wang, E. G. *Phys. Rev. B: Condens. Matter* **2006**, *74*, 245409.

(102) Allouche, A. *Surf. Sci.* **1998**, *406*, 279.

(103) Jones, R. O.; Gunnarsson, O. *Rev. Mod. Phys.* **1989**, *61*, 689.

(104) Duffin, A. M.; England, A. H.; Schwartz, C. P.; Uejio, J. S.; Dallinger, G. C.; Shih, O.; Prendergast, D.; Saykally, R. J. *Phys. Chem. Chem. Phys.* **2011**, *13*, 17077.

(105) Maheshwary, S.; Patel, N.; Sathyamurthy, N.; Kulkarni, A. D.; Gadre, S. R. *J. Phys. Chem. A* **2001**, *105*, 10525.

(106) Pedulla, J. M.; Jordan, K. D. *Chem. Phys.* **1998**, *239*, 593.

(107) Tsai, C. J.; Jordan, K. D. *J. Phys. Chem.* **1993**, *97*, 5208.

(108) Diri, K.; Myshakin, E. M.; Jordan, K. D. *J. Phys. Chem. A* **2005**, *109*, 4005.

(109) Wang, F. F.; Jenness, G.; Al-Saidi, W. A.; Jordan, K. D. *J. Chem. Phys.* **2010**, *132*, 134303.

(110) *NIST Chemistry WebBook, NIST Standard Reference Database Number 69*; Linstrom, P. J.; Mallard, W. G., Eds.; National Institute of Standards and Technology: Gaithersburg MD, 20899, 2013.

(111) Gatica, S. M.; Cole, M. W. *J. Low Temp. Phys.* **2009**, *157*, 111.

(112) Dasgupta, S.; Hammond, W. B.; Goddard Iii, W. A. *J. Am. Chem. Soc.* **1996**, *118*, 12291.

(113) Dasgupta, S.; Smith, K. A.; Goddard Iii, W. A. *J. Phys. Chem.* **1993**, *97*, 10891.

(114) Karasawa, N.; Dasgupta, S.; Goddard Iii, W. A. *J. Phys. Chem.* **1991**, *95*, 2260.

(115) Karawasa, N.; Goddard Iii, W. A. *Macromolecules* **1992**, *25*, 7268.

(116) Frisch, M. J. e. a.; Gaussian, Inc.: Wallingford CT, 2009.

(117) Breneman, C. M.; Wiberg, K. B. *J. Comput. Chem.* **1990**, *11*, 361.

(118) Adams, A. H.; National Research Council and McGraw-Hill Book Comany, Inc.: New York, 1928; Vol. 3.

(119) Mott, N. F.; Jones, H. *The Theory of the Properties of Metals and Alloys*; Dover Publication: New York, 1975.

(120) Henkelman, G.; Uberuaga, B. P.; Jonsson, H. *J. Chem. Phys.* **2000**, *113*, 9901.

(121) Sheppard, D.; Terrell, R.; Henkelman, G. *J. Chem. Phys.* **2008**, *128*, 134106.

(122) Sheppard, D.; Xiao, P. H.; Chemelewski, W.; Johnson, D. D.; Henkelman, G. *J. Chem. Phys.* **2012**, *136*, 074103.

(123) Jónsson, H.; Mills, G.; Jacobsen, K. W. *Classical and Quantum Dynamics in Condensed Phase Simulations*; World Scientific: Singapore, 1998.

(124) Cárdenas, R.; Lagúnez-Otero, J.; Flores-Rivero, A. *Int. J. Quantum Chem.* **1998**, *68*, 253.

(125) Keith, J. A.; Carter, E. A. *Chem. Sci.* **2013**, *4*, 1490.

(126) Kreevoy, M. M.; Hutchins, J. E. *J. Am. Chem. Soc.* **1972**, *94*, 6371.

(127) Pepperberg, I. M.; Halgren, T. A.; Lipscomb, W. N. *J. Am. Chem. Soc.* **1976**, *98*, 3442.

(128) Willem, R. *J. Chem. Soc., Dalton Trans.* **1979**, 33.

(129) Tuckerman, M. E.; Marx, D.; Parrinello, M. *Nature* **2002**, *417*, 925.

(130) Tuckerman, M.; Laasonen, K.; Sprik, M.; Parrinello, M. *J. Chem. Phys.* **1995**, *103*, 150.

(131) Hoheisel, C.; Kutzelnigg, W. *J. Am. Chem. Soc.* **1975**, *97*, 6970.

(132) Stanton, J. F.; Lipscomb, W. N.; Bartlett, R. J. *J. Am. Chem. Soc.* **1989**, *111*, 5173.

(133) Davis, R. E.; Swain, C. G. *J. Am. Chem. Soc.* **1960**, *82*, 5949.

(134) Gardiner, J. A.; Collat, J. W. *Inorg. Chem.* **1965**, *4*, 1208.

(135) Gardiner, J. A.; Collat, J. W. *J. Am. Chem. Soc.* **1965**, *87*, 1692.

(136) Davis, R. E.; Bromels, E.; Kibby, C. L. *J. Am. Chem. Soc.* **1962**, *84*, 885.

(137) Wang, F. T.; Jolly, W. L. *Inorg. Chem.* **1972**, *11*, 1933.

(138) Gardiner, J. A.; Collat, J. W. *J. Am. Chem. Soc.* **1964**, *86*, 3165.

(139) Garrett, B. C.; Dixon, D. A.; Camaioni, D. M.; Chipman, D. M.; Johnson, M. A.; Jonah, C. D.; Kimmel, G. A.; Miller, J. H.; Rescigno, T. N.; Rossky, P. J.; Xantheas, S. S.; Colson, S. D.; Laufer, A. H.; Ray, D.; Barbara, P. F.; Bartels, D. M.; Becker, K. H.; Bowen Jr, K. H.; Bradforth, S. E.; Carmichael, I.; Coe, J. V.; Corrales, L. R.; Cowin, J. P.; Dupuis, M.; Eisenthal, K. B.; Franz, J. A.; Gutowski, M. S.; Jordan, K. D.; Kay, B. D.; LaVerne, J. A.; Lymar, S. V.; Madey, T. E.; McCurdy, C. W.; Meisel, D.; Mukamel, S.; Nilsson, A. R.; Orlando, T. M.; Petrik, N. G.; Pimblott, S. M.; Rustad, J. R.; Schenter, G. K.; Singer, S. J.; Tokmakoff, A.; Wang, L. S.; Wittig, C.; Zwier, T. S. *Chem. Rev.* **2005**, *105*, 355.

(140) Burns, W. G.; Moore, P. B. *Radiat. Eff.* **1976**, *30*, 233.

(141) Chatterjee, A.; Magee, J. L.; Dey, S. K. *Radiat. Res.* **1983**, *96*, 1.

(142) Bakker, H. J.; Nienhuys, H. K. *Science* **2002**, *297*, 587.

(143) Kawashima, Y.; Takeo, H.; Matsumura, C. *Chem. Phys. Lett.* **1978**, *57*, 145.

(144) Kawashima, Y.; Takeo, H.; Matsumura, C. *J. Chem. Phys.* **1981**, *74*, 5430.

(145) Beaird, A. M.; Li, P.; Marsh, H. S.; Al-Saidi, W. A.; Johnson, J. K.; Matthews, M. A.; Williams, C. T. *Ind. Eng. Chem. Res.* **2011**, *50*, 7746.

(146) Brüesch, P. *Phonons: Theory and Experiments II*; Springer: Berlin, 1986.

(147) ICSD, http://www.fiz-karlsruhe.de/icsd.html

(148) OPIUM - Pseudopotential Generation Project, http://opium.sourceforge.net/

(149) Nakamoto, K. *Infrared and Raman Spectra of Inorganic and Coordination Compounds*; 4th ed.; Wiley, 1986.

(150) Jun, L.; Shuping, X.; Shiyang, G. *Spectrochim. Acta, Part A* **1995**, *51*, 519.

(151) Chryssikos, G. D.; Kapoutsis, J. A.; Patsis, A. P.; Kamitsos, E. I. *Spectrochim. Acta, Part A* **1991**, *47*, 1117.

(152) Pinchas, S.; Shamir, J. *J. Chem. Phys.* **1972**, *56*, 2017.

(153) Corazza, E.; Menchetti, S.; Sabelli, C. *Acta Crystallogr., Sect. B: Struct. Sci* **1975**, *31*, 1993.

(154) Torrie, G. M.; Valleau, J. P. *Chem. Phys. Lett.* **1974**, *28*, 578.